The Physicochemical Impact of Tocopherols on Lipid Membranes

Panagiota Taktikakis

A Thesis
in
The Department
of
Chemistry and Biochemistry

Presented in Partial Fulfillment of the
Requirements for the Degree of Master of Science (Chemistry and Biochemistry)
At Concordia University
Montreal, Quebec, Canada

August 2024

CONCORDIA UNIVERSITY

School of Graduate Studies

This is to certify that the thesis prepared

By: Panagiota Taktikakis

Entitled: The Physicochemical Impact of Tocopherols on Lipid Membranes

and submitted in partial fulfillment of the requirements for the degree of

Master of Science (Chemistry and Biochemistry)

complies with the regulations of the University and meets the accepted standards with respect to originality and quality.

Signed by the final Examining Committee:

Dr. Peter Pawelek Chair

Dr. Louis Cuccia Examiner

Dr. Peter Pawelek Examiner

Dr. Christine DeWolf Supervisor

Approved by Dr. Louis Cuccia (Graduate Program Director)

September 5th 2024 Pascale Sicotte Dean, Faculty of Arts and Science

ABSTRACT

The Physicochemical Impact of Tocopherols on Lipid Membranes

Panagiota Taktikakis

Lung surfactant is the lipid-protein monolayer at the interface between the air and the liquid lining the alveoli. It serves to ensure the lungs stay inflated during inhalation and to reduce the surface tension to prevent its collapse at the end of expiration. Exposure to e-cigarette additives vitamin E (α–tocopherol) and its acetate derivative vitamin E acetate (α–tocopherol acetate) through vaping has been linked to e-cigarette or vaping product use-associated lung injury (EVALI). This condition disrupts normal lung function, leading to severe respiratory distress that can cause hospitalization for difficulty in breathing, and, in some cases, lung collapse or death. Using a Langmuir balance, excess area calculations, Brewster angle microscopy (BAM), atomic force microscopy (AFM) and molecular studies such as grazing incidence X–ray diffraction (GIXD) and X–ray reflectivity (XR), the effects of these additives on the lung surfactant monolayer film have been examined and changes in surface activity, morphology, and molecular organization of the film assessed. The introduction of α–tocopherol and α–tocopherol acetate alters the fluidity, phase balance and modifies the composition of the different phases present. These changes could potentially impair normal lung surfactant function. This research also addresses potential short-term impacts on lung surfactant function due to vaping. In addition to its effects on lung surfactant, we studied α–tocopherol, the most bioavailable form of vitamin E, for its interaction with common membrane lipids. Known as a potent membrane-soluble antioxidant, α–tocopherol plays an irreplicable role in preventing lipid peroxidation, which can otherwise lead to the degradation of cellular membranes, or even cell death. We used the same techniques to explore the mixing behaviour of α–tocopherol with both saturated and unsaturated membrane lipids. This revealed how α–tocopherol's interactions vary based on the degree of lipid unsaturation, independent of the lipids headgroup.

ACKNOWLEDGMENTS

I would like to express my deepest gratitude to my supervisor, Dr. Christine DeWolf, whose unwavering support, and guidance have been invaluable throughout this journey. Her presence and encouragement have been a solid foundation for my work, and her efforts in facilitating collaborations between institutions have been crucial to the success of this project. I am especially grateful for her advice on taking breaks when needed and her balanced approach in pushing me to reach my full potential. Her willingness to spend countless hours with me on manuscript writing, offering creative ideas, and suggesting solutions to the challenges I faced has been instrumental. Her promotion of good laboratory practices and professionalism, both in the lab and in real life, has profoundly impacted my development. I am also deeply appreciative of the opportunity to run experiments at the synchrotron in Chicago, which she generously funded.

I would also like to thank the former lab members, Dr. Hala Youssef, Kailen Kroeger, Mathieu Côté, and Nivetha Subramanian whose ideas, experimental contributions laid the groundwork for this project. Your input was a valuable steppingstone in completing this work. To the current lab members, Maryam Lormahdiabadi, Anthony Koukoulomatis, Dalia Ali, Dr. Nicolas Bondon, and Zahra Alinia for a memorable experience and teaching me many things.

I sincerely thank my committee members, Dr. Cuccia, Dr. Passarelli, and replacement member Dr. Pawelek, for their guidance, great questions, contribution to this project and support. I would also like to thank professors throughout my masters Dr. Mejewski, Dr. Pawelek, and Dr. Oh, whose courses were interesting and challenged me to step out of my comfort zone.

My thanks to our collaborator and talented researcher, Dr. Antonella Badia from the department of chemistry at Université de Montréal, who contributed to the ideation, writing, and processing of the manuscripts in my thesis. Your involvement has been a crucial part of this research.

To my family, mother Vicky Valkanas, father Aristotelis Taktikakis, stepfather George Stavrakakis, and siblings Elizabeth, Anastasia, Konstantinos and George, and friends, Pooja, Kimberly, and Erin, your unconditional emotional support during this master's program has been

a source of strength. Your presence and understanding during the tough and good times have meant the world to me.

I want to also give a special thanks to my two Yorkie puppies, Queenie (4 years) and Chanel (1 year), whose companionship has been a constant source of joy and comfort. Their presence always managed to bring a smile to my face, no matter how challenging the day.

Finally, I am so grateful for the time I've had the past two years, which allowed me to focus on my well-being and sparked my passion for running that's been beneficial for my mental health.

Contribution of Authors

For Manuscript 1, Panagiota Taktikakis drafted the manuscript, collected, and analyzed the majority of the data. Nivetha Subramanian and Mathieu Côté, who were undergraduate students, both carried out preliminary experimental studies such as isotherms and BAM imaging prior to this master's thesis project. Kailen Kroeger was an undergraduate student at the time when he undertook a preliminary literature search for project formulation, conducted preliminary isotherms and contributed to X–ray diffraction data and collection. Dr. Hala Youssef was a research assistant who contributed to X–ray diffraction data collection and some analysis. Dr. Antonella Badia is a professor at Université de Montréal and research collaborator who contributed to project conception. The writing of the manuscript was carried out by Panagiota Taktikakis under the supervision of Dr. Christine DeWolf, and reviewed by collaborator Dr. Antonella Badia.

For Manuscript 2, the experiments were carried out by Panagiota Taktikakis. The writing of the manuscript was carried out by Panagiota Taktikakis under the supervision of Dr. Christine DeWolf, and reviewed by collaborator Antonella Badia.

For both manuscripts Dr. Chrstine DeWolf contributed to project conceptualization, funding acquisition, supervision and was involved in data analysis/interpretation and manuscript writing.

Table of contents

List of Abbreviations

ATII:	Alveolar type II cells
DPPC:	Dipalmitoyphosphotidylcholine
LC:	Liquid-condensed
RDS:	Respiratory distress syndrome
COPD:	Chronic obstructive pulmonary disease
EVALI:	Electronic-cigarette or vaping product use-associated lung injury
CDC:	Centers for Disease Control and Prevention
THC:	Tetrahydrocannabinol
BAL:	Bronchoalveolar
FDA:	Food and Drug Administration
–OH:	Hydroxyl group
Vitamin C:	Ascorbic acid
TPGS:	D–α–tocopherol polyethylene glycol 1000 succinate
DOPC:	Dioleoylphosphatidylcholine
POPC:	Palmitoyl oleoyl phosphatidyl choline
DOPE:	Dioleoylphosphatidylethanolamine
POPG:	1-palmitoyl-2-oleoyl-sn-glycero-3-phosphoglycerol
Vitamin E:	α–Tocopherol
Vitamin E acetate:	α–Tocopherol acetate
BAM:	Brewster angle microscopy
AFM:	Atomic force microscopy
GIXD:	Grazing incidence X–ray diffraction
XR:	X–ray reflectivity
LE:	Liquid-expanded
LB:	Langmuir-Blodgett
APS:	Advanced Photon Source
α_i:	Incident angle

2D:	Two-dimensional
3D:	Three-dimensional
ρ:	Electron density
DUPC:	Diundecanoylphosphatidylcholine
Tris:	Tris(hydroxymethyl)aminomethane
C_s^{-1}:	Compressibility modulus
DMPC:	1,2-Dimyristoyl-sn-glycero-3-phosphocholine

List of Figures

List of Tables

List of Equations

Chapter 1. Introduction & Literature Review

1.1. Langmuir Monolayers as Model Membranes

The structure and properties of biological membranes have been studied and understood through the development of simple to complex model membranes. Model membranes are categorized into three main systems including monolayers, liposomes, and planar bilayers.[1] This review centers on Langmuir monolayer systems as model membranes. These systems offer an advantage over other model systems due to their simplicity in controlling the composition and density of the lipid monolayer. Additionally, multi-component mixtures are attainable with relative ease.

Langmuir monolayers were first developed over a century ago by Irving Langmuir and are widely recognized for studying chemical interfaces through his works on adsorption theory.[2] The monolayers are created by spreading a surface-active molecule (amphiphilic molecule) onto a liquid subphase of choice, where it forms a self-assembling one-molecule thick layer. In the case of a monolayer composed of exclusively phospholipids, the hydrophilic headgroup region is facing or embedded into the liquid phase and hydrophobic tail region is facing the atmospheric phase (air, vapors, etc). This system allows for the precise control over and manipulation of the i) packing of the spread molecules, and ii) environmental conditions such as atmosphere, temperature, pH, and ionic strength.[3] It's simplicity and all these features make Langmuir monolayers an enticing choice for studying the physicochemical properties of monolayers, and how these properties change under different conditions. Langmuir monolayers are often used to mimic the behavior of biological membranes such as bilayers (as half of the bilayer of biological membranes) and/or biological monolayers such as the tear film, lung surfactant, and bile salts that also play critical roles in ensuring the proper function of the eyelids, alveoli, and digestive system, respectively. Additionally, Langmuir monolayers have been used to investigate various lipid compositions and other components, aiming to identify the optimal simplified model biomembrane for the different membrane types such as human plasma membrane, different types of organelle membranes, and bacterial membranes.[4,5] By mimicking these common membranes in the human body, the literature has studied the behavior between its components and antimicrobial molecules[3], proteins[6,7], nanoparticles[8–10], ions[11], environmental pollutants[12,13], among other interacting compounds.

1.2. Lung Surfactant

This review details the mammalians lung surfactant composition, structure and function as well as various natural and synthetic model lung membranes commonly used and accepted in the literature to study its film activity, film morphology and film structure.

1.2.1. Lung Surfactant Composition, Structure, Dynamics & Function

The lung surfactant is a monolayer composed of a mixture of lipids and proteins that is formed at the interface between the air and liquid lining the alveoli in the lungs. It was discovered in 1929 by Von Neergaard[14] who studied its function in porcine lungs and demonstrated that a lower surface tension plays a critical role in the respiratory mechanism and function.[15] The lower surface tension attained by the lung surfactant prevents alveolar collapse at the end of exhalation (atelectasis) and facilitates the work of breathing. Although this surfactant system is mostly known for its role in alveolar surface tension lowering it is also vital for efficient gas exchange and overall respiratory function.

The primary components of the lung surfactant are phospholipids and surfactant proteins synthesized by alveolar type II cells (ATII) depicted in Figure 1.1.[16] Phospholipids make up approximately 80% to 90% of the molecular weight of the mammalian lung surfactant which include a large amount of phosphocholines, phosphoglycerols, and a lower amount of phosphoinositols, phosphoethanolamine and phosphoserine.[17] In this lipid mixture, phosphocholine is the most abundant, accounting for approximately 65%, and next is monounsaturated phosphotidylglycerol, accounting for 7-15% of the total lipids.[16] Saturated dipalmitoyphosphotidylcholine (DPPC), makes up almost half of the phosphocholine lipids, making it the most abundant phospholipid in the lung surfactant.[16,17] The remaining 10% to 20% of its molecular weight provides room for the surfactant proteins (mainly SP-A, SP-B and SP-C) and some carbohydrates.[17] SP-A is a hydrophilic surfactant protein and SP-B along with SP-C are both hydrophobic.[17]

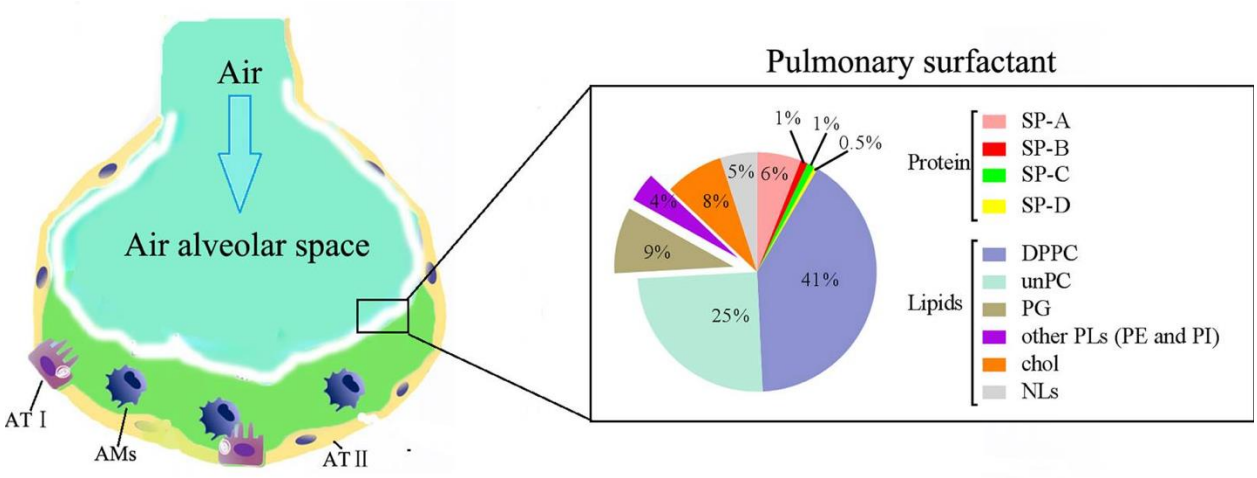

Figure 1.1. Alveolar sac with ATII (left) as well as lung surfactant components including phospholipids and surfactant proteins shown with approximate percentage of relative to the total lung surfactant molecular weight (right).[16]

The lungs of adult humans can reach up to 500 million alveoli[18] with an average alveoli diameter of 200 mm[19], which means the lung surfactant covers a very large area. The large area covered by the lung surfactant makes it an ideal model for studies using Langmuir monolayer techniques. This approach is advantageous as it does not require consideration of membrane curvature. Given the relatively planar nature of the lung surfactant due to its large size, it remains unaffected by curvature effects. The lungs are a highly dynamic organ that work non-stop for us to breathe. During a normal breathing cycle the surface area of the alveoli changes by about 30%[20,21] between the end of inhalation (when the lungs are filled with air) and the end of exhalation (when the lungs are emptied of air). This dynamic variation requires the lung surfactant to adapt continuously to maintain its function of reducing surface tension and preventing alveolar collapse, which is at most risk for collapse at the end of each breath (expiration). Fortunately, the lipids and surfactant proteins of the lung surfactant and its structural arrangement which will be discussed in the next paragraph, work synergistically to ensure the stability and proper function of the lung surfactant during each breathing cycle. The biophysical properties of this monolayer, such as its ability to undergo rapid adsorption and re-spreading, are essential for its function and depicted in Figure 1.2.[22]

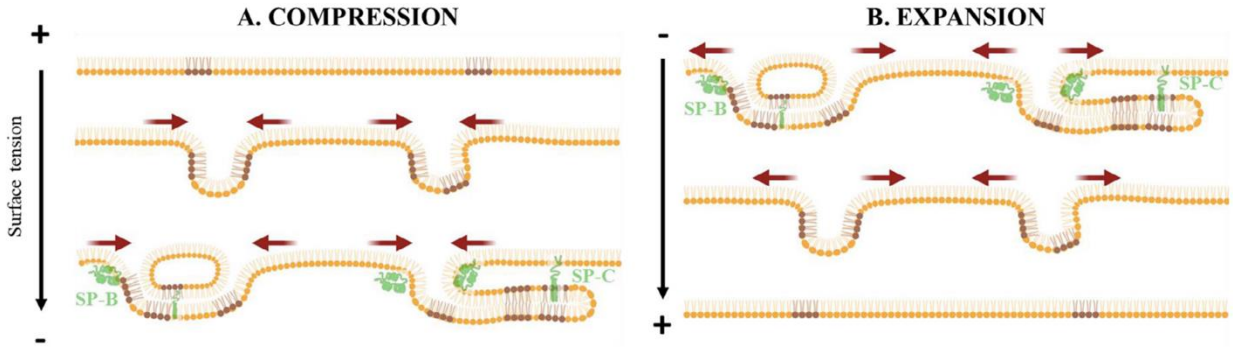

Figure 1.2. The lung surfactant film at the air-liquid interface during a breathing cycle for (a) compression and (b) expansion with corresponding surface tension changes upon compression and expansion. Molecules with surface activity depicted in brown and orange colors and surfactant proteins SP-B and SP-C depicted as a green color. The surface tension is the lowest at the end of compression and beginning of expansion of the lung surfactant.[22]

The next few sentences will discuss the molecular dynamics that occur during the compression and expansion period of a breathing cycle. The mixture of lipids and surfactant proteins in lung surfactant is critical for creating a surfactant that significantly lowers the surface tension within the alveoli. The compression of the breathing cycle during exhalation (Figure 1.2a) requires the reorganization of surfactant molecules to reduce surface tension to near-zero values[23] and prevent the collapse of the lungs. The proper mechanical function of the breathing cycle is helped by certain lipid-protein interactions between SP-B and SP-C with unsaturated lipids and DPPC. Here, SP-B and SP-C have specific roles, one of which is helping in the rapid lipid adsorption (primarily unsaturated lipids) to the interface, by rapidly adhering onto the proteins, in a process termed the "squeeze-out" theory.[24–26] At this point, after the unsaturated lipids have been squeezed out (while remaining adhered to surfactant proteins), the monolayer is enriched in saturated DPPC molecules that form a tight packing into a liquid-condensed (LC) phase, creating a continuous and stable monolayer, thereby promoting low surface tension to the near-zero value. On the other hand, the expansion of the breathing cycle during inhalation (Figure 1.2b) requires that the surfactant molecules re-adjust quickly to accommodate the increased surface area.[27] The process is also helped by surfactant proteins SP-B and SP-C which facilitate the re-spreading or unpacking of the lipid molecules to accommodate for the larger surface area while the alveoli sacs are filling with air.[27] Liekkinen *et al*. showed the preferential interaction between monounsaturated POPG and SP-B/C, correlating well to the concept that mainly unsaturated lipids are "squeezed-out" of the film.[28]

It has also been shown through isotherm work that SP-B/C increase the surface pressures[28–31], thus increasing the stability of the lung surfactant in the presence of surfactant proteins. Ultimately, all the components of the lung surfactant work together to make it easier for them to expand and contract during breathing, thereby facilitating the mechanics of respiration.

Now although this surfactant system is mostly known for its role in alveolar surface tension, it also plays a crucial role in gas exchange when you breathe. The lungs facilitate gas exchange between oxygen uptake and release of carbon dioxide, and to do so these gases must first pass through the lung surfactant. The large area available is also required for proper gas exchange between oxygen and carbon dioxide.[19] Studies have shown that effective gas exchange is greatly affected by changes in amount, composition, and structure in the lung surfactant.[32–34] Additionally, the lung surfactant plays a role in host defense mechanisms[17] to protect the lungs from pathogens.

1.2.2. Lung Surfactant Model Membrane Studies

Surfactant model membranes mimic biological membranes to help in understanding lung diseases such as respiratory distress syndrome (RDS), chronic obstructive pulmonary disease (COPD), lung cancer, cystic fibrosis, and impact on the lungs in terms of structure, function and interaction by airborne pollutants, electronic-cigarette (e-cigarettes) liquids and vapors, novel inhalation therapies for lung diseases, amongst other things.

Lung surfactant model membrane studies encompass a diverse array of naturally occurring surfactants (animal-derived) and synthetic surfactants (first- and second-generation) aimed at replicating the complex behavior of the human lung surfactant.[35] For example, the first-generation synthetic lung surfactants were protein-free and include Exosurf, ALEC, Turfsurf, as well as used combinations of surface active molecules such as DPPC, hexadecanol, and tyloxapol, amongst other compounds.[35,36] These were originally administered exogenously to treat infants having RDS, or premature infants whose lungs were not fully developed and lack adequate surfactant production.[35,36] This exogenous lung surfactant therapy helps reduce surface tension in the alveoli, preventing collapse and improving gas exchange, thereby supporting respiratory function until the infant's lungs mature sufficiently to produce surfactant naturally. This led to the first successful exogenous surfactant replacement therapy and reported by Fujiwara *et al.* using an animal-derived surfactant called Surfacten that originates from bovine lung surfactant extract and contains phospholipids and surfactant proteins.[35,37] Other examples of natural surfactants that are FDA

approved are Survanta, Curosurf, bLES, Infasurf, Alveofact and Human surfactant.[35] Studies comparing protein-free and protein-containing surfactants deemed protein-free surfactants to not lower surface tension as well, which may be attributed to the absence of surfactant proteins SP-B and SP-C.[38] To mimic natural surfactant, protein-containing second-generation synthetic surfactants were created including Lucinactant and CHF5633.[36] Nowadays, first-generation synthetic surfactants are no longer used in-clinic to treat RDS-related diseases instead natural surfactants and second-generation synthetic surfactants are used.[35] However, for models that serve as effective analogs for studying interactions and behaviors of the lung surfactant under different conditions range from highly sophisticated natural animal-based membranes to simpler synthetic membranes (protein-free and/or protein-containing).

1.3. Electronic-cigarette or Vaping Product Use-Associated Lung Injury (EVALI)

This review will discuss why the use of vitamin E acetate is a subject of concern for the public health, particularly in the context of electronic-cigarette or vaping product use-associated lung injury (EVALI) and why it is significant to study its impact on the lung surfactant.

1.3.1. Outbreak, Cause and Physiological Consequences of EVALI

EVALI is a medical condition where a person's lungs are damaged from substances found in e-cigarettes and vaping products. As of 2020, a total of 2558 hospitalized patients with nonfatal cases and 60 patients with fatal cases of EVALI had been reported to the Centers for Disease Control and Prevention (CDC).[39] EVALI symptoms include shortness of breath, cough, fever, gastrointestinal symptoms (nausea, vomiting, abdominal pain, etc), chest pain and dizziness.[40] Because these symptoms closely resemble those of COVID-19, and because many EVALI cases occurred during the peak of the pandemic, patients were suspected to have COVID-19, but all tests were negative.[40] Upon further investigation, which included a detailed review of the patients' vaping history, it was concluded these cases were related to vaping.[40] A study published in the New England Journal of Medicine established a connection between vitamin E acetate and EVALI, specifically in individuals using tetrahydrocannabinol (THC)-containing e-cigarettes.[41] Analyzing bronchoalveolar lavage (BAL) fluid samples from 51 EVALI patients, the study identified vitamin E acetate in 94% of the BAL samples.[41] This additive was since considered a potential cause of

EVALI. Following the discovery of vitamin E acetate in vaping products in September 2019, it was prohibited from the vaping supply chain, resulting in a decline in EVALI cases, as shown in Figure 1.3.

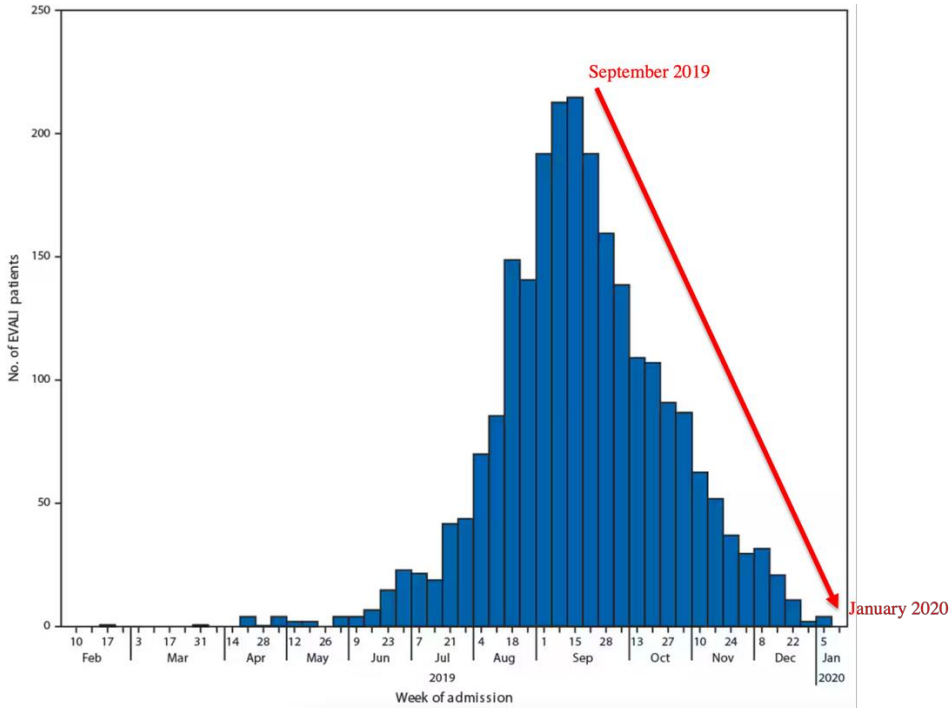

Figure 1.3. Weekly hospitalizations from EVALI as well as decline in cases from September 2019 to January 2020. Figure adapted from[42].

Although vitamin E acetate is FDA approved for ingestion and has many nutritional and health benefits (to be discussed in Section 1.4), it's inhalation may be harmful since its chemical structure is comparable to surface active phospholipids such as those found in the lung surfactant. It was added to e-cigarette liquids as an illegal cutting agent to dilute the illicit THC and lower their cost. Duffy *et al.* in 2019 recovered 38 samples from the first 10 New York cases of EVALI for which they obtained cartridges and found a low percentage of cannabinoid content and a large content of vitamin E acetate of approximately 64% of the e-cigarette fluids.[43] From this they tested six commercial brands of cannabinoid oil cartridges where in three of six vitamin E acetate was found to be >95% of the cartridges content, two were found to be primarily squalene, and one primarily a-bisabol.[43] Another recent study tested common e-cigarette liquid cutting agents (coconut oil and vitamin E acetate, etc) which lead to the formation of vaping emission condensations having toxic byproducts, including quinones, carbonyls, esters, and alkyl alcohols.[44] The condensates enhanced

the cytotoxicity of human airway epithelial cells, which may be linked to EVALI, amongst other health effects.[44]

EVALI manifests as an acute or subacute respiratory illness that can mimic various pulmonary diseases. Acute lung injury was observed including cough, shortness of breath and chest pain which can progress into severe respiratory distress and in some cases result in the need for mechanical respiration.[43] Another physiological impact is the trigger of an inflammatory response in the lungs upon repeated inhalation of vitamin E acetate which can compromise the lungs and contribute to the development of lung injury.[45] Along with inflammation of the lungs, a study found that EVALI represents a form of chemical pneumonitis from one or more inhaled toxic substances found in e-cigarette solutions.[46] A study exposed mice to inhalation of vitamin E acetate and they estimated the mouse would have inhaled 0.08 mg to 0.17 mg of vitamin E acetate per gram of body weight per day, a dose equivalent to the amount that an adult cannabinoid e-cigarette user would inhale daily.[47] The BAL in the mice after a two week exposure revealed that vitamin E acetate was effectively delivered to the lungs and match the findings of vitamin E acetate in BAL fluid from patients with EVALI.[47]Additionally, mice exposed to vitamin E acetate revealed alveolar macrophages containing an abundance of oily red O-stained residue, often in oil clusters, presumed to be vitamin E acetate, residing with pneumocytes lining the alveoli.[47] In addition to respiratory effects, some EVALI cases associated with vitamin E acetate reported gastrointestinal symptoms such as nausea, vomiting, and abdominal pain as well as cardiac health implications, however, the exact mechanism behind these symptoms and their connection to vitamin E acetate is not fully yet understood.[48] Therefore, our current understanding of the physiological impacts of vitamin E acetate in association with EVALI encompass acute lung injury, inflammation, pneumonitis, gastrointestinal symptoms, and cardiac health implications.[43,46–48]

1.3.2. Effects of Vitamin E Acetate on the Lung Surfactant

Recent studies have highlighted the adverse effects of vitamin E acetate on lung surfactant function. The presence of vitamin E acetate in the BAL of most EVALI patients indicated its retention in the alveoli of the lungs. Maintaining lung surfactant homeostasis is crucial for ensuring a functional film at the respiratory interface.[49] The composition, synthesis, secretion, reuptake, and degradation of surfactant components must be tightly regulated and balanced.[49] Any changes in the lung surfactant composition disrupts the balance, in this case through the deposition of vitamin

E acetate, which would then potentially impair its function and contribute to the reported symptoms of EVALI.

In a preliminary laboratory analysis conducted by the FDA, 1,090 vaping solutions associated with EVALI patients were examined. The analysis proved that approximately 50% of these samples contained the illicit diluent vitamin E acetate, with concentrations ranging from 23% to 88% in the affected samples.[41] The delivery of vitamin E acetate was found to be highly effective, with an exposure comparable to an e-cigarette user inhaling 0.5 mL to 1.1 mL of a vaping liquid containing high amount of vitamin E acetate.[47] Understanding the mechanisms by which vitamin E acetate affects the lung surfactant is crucial for developing strategies to mitigate its harmful effects. DiPasquale *et al.* first looked into the viscoelastic properties of a model lung membrane composed of DPPC:POPC:POPG:Chol (0.48:0.32:0.10:0.10) in the presence of up to 10 mol % vitamin E acetate.[50] They showed that vitamin E acetate inhibits the surfactant's ability to achieve the low surface tensions necessary for effective respiration.[50] Van Bavel *et al*. looked at a model lung surfactant membrane composed of an 8-lipid system with surfactant protein SP-B as well as natural surfactant bLES in the presence of vitamin E acetate. In the 8-lipid model, interactions with SP-B and vitamin E acetate were observed, suggesting changes to surfactant protein function.[51] These interactions may disrupt one of the main functions of SP-B assisting in the "squeeze out" of unsaturated lipids to reduce surface tension at the end of expiration which can lead to a dysfunctional lung surfactant membrane.[51] Later they investigated the stability and film organization of a simpler lung surfactant model made of DPPC:POPG in the presence of vitamin E, vitamin E acetate, THC and cannabidiol.[52] Results indicate that these additives destabilize surfactant films by affecting lipid chain packing and film compressibility. Furthermore, imaging methods showed smaller domains within the surfactant monolayer in the presence of both vitamin E and vitamin E acetate, suggesting changes to lipid organization.[52]

1.4. Biological Relevance of α–Tocopherol

This section will cover α–tocopherol, examining its molecular composition, structural features, and reactivity. It will also discuss its natural abundance, role in membranes, and various exogenous occurrences and uses.

1.4.1. Molecular Composition, Structural Features & Reactivity

α–Tocopherol, a form of vitamin E, has the molecular formula of $C_{29}H_{50}O_2$ and a molecular weight of 430.71 g/mol. The structure of α–tocopherol is characterized by a chromanol ring with a hydroxyl group (–OH) flanked at the 6th position in its phenolic moiety (Figure 1.4).

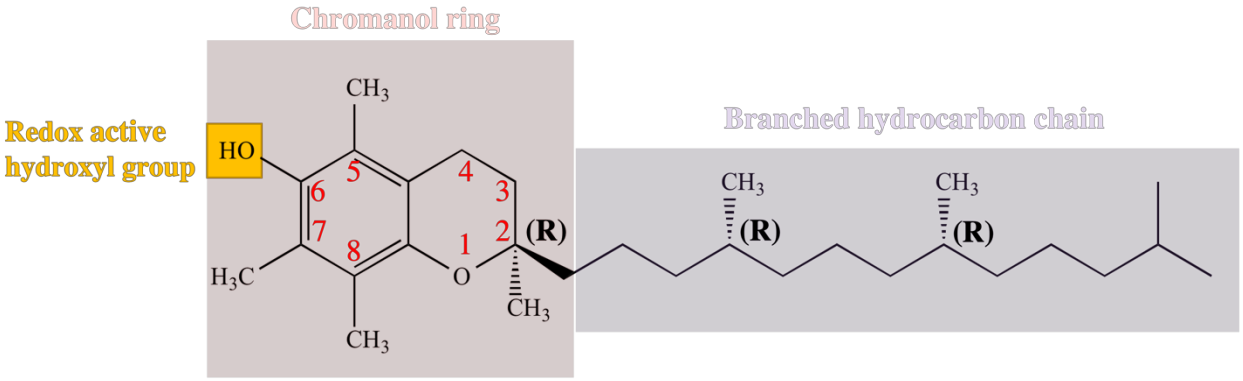

Figure 1.4. Molecular structure of naturally occurring RRR–α–tocopherol.

The chromanol ring is attached to a 13-carbon long branched hydrocarbon chain. α–Tocopherol has three chiral centers: one on the chromanol ring and two on the branched hydrocarbon chain. There are two forms of α–tocopherol: the naturally occurring stereoisomer, RRR–α–tocopherol, and the synthetic form, which is a racemic mixture.[53]

α–Tocopherol is known but not limited to its antioxidant abilities in the body. The chemical reactivity of α–tocopherol is primarily due to the –OH group. The way in which this group exerts is function is by donating a hydrogen to radicals which then forms itself a more stable and less reactive resonance-stabilized α–tocopheroxyl radical shown in Figure 1.5.[54] The resulting α–tocopheroxyl radical can be converted back to α–tocopherol by another α–tocopherol or other antioxidant molecules such as ascorbic acid (vitamin C) and/or glutathione, allowing the α–tocopherol to participate in many more oxidation-reduction reactions before being degraded.[54,55] This process is shown in Figure 1.5.

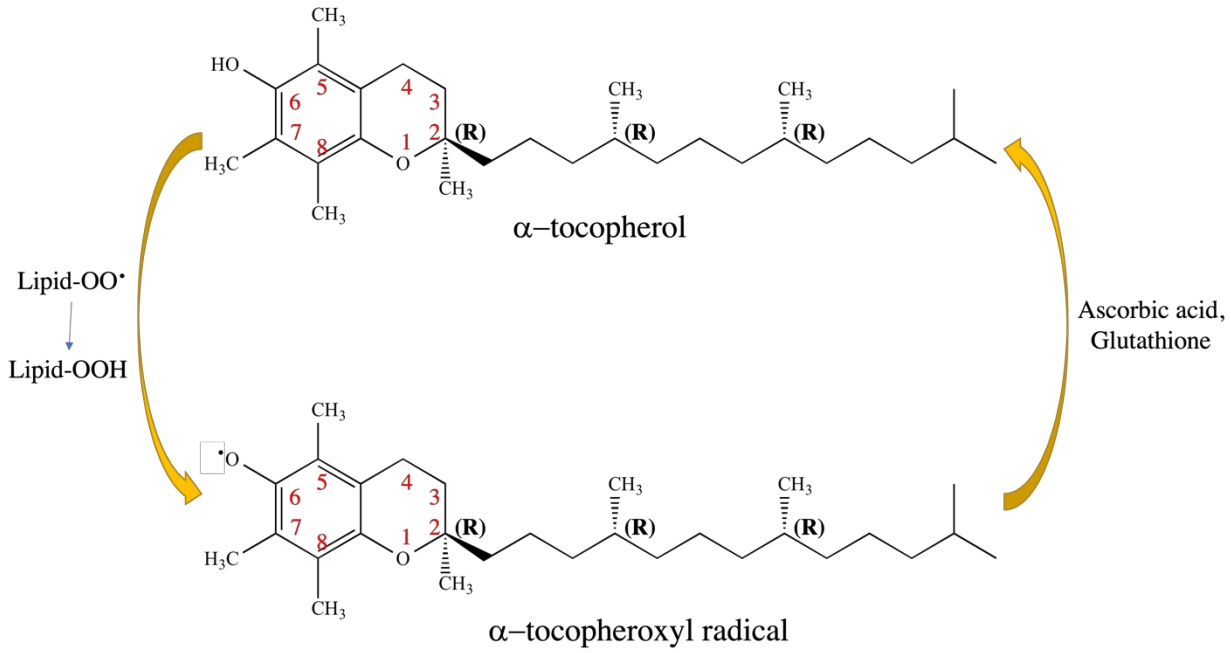

Figure 1.5. Oxidation-reduction reaction process with α–tocopherol, lipids, ascorbic acid, and glutathione.

1.4.2. Natural Abundance

Rich sources of α–tocopherol is most commonly found in plant seeds including peanuts, almonds and sunflower, and as a result in many plant oils including canola, olive and peanut oil.[56] Tocopherols are exclusively synthesized by photosynthetic organisms and are distributed widely across various plants tissues including seeds, fruits, roots and usually leafy greens.[55] They are found in the green moiety of plants and primarily located in chloroplast and thylakoid membranes, near the photosynthetic machinery, in order to reduce oxidative damage in the plant during processes such as photosynthesis and respiration.[55] α–Tocopherol is one of eight isomers of vitamin E, which include two groups of four tocopherols (a, b, g, d) and four tocotrienols (a, b, g, d). These groups differ on side chain level of unsaturation with tocopherols being fully saturated and tocotrienols being triunsaturated as depicted in Figure 1.6.

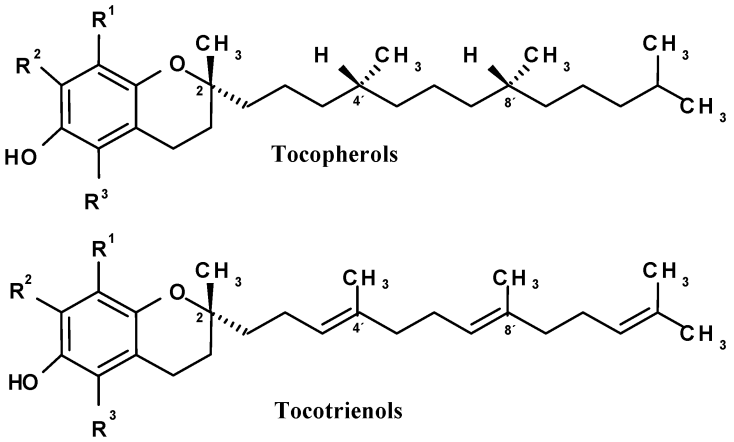

	R^1	R^2	R^3
α-	CH_3	CH_3	CH_3
β-	CH_3	H	CH_3
γ-	CH_3	CH_3	H
δ-	CH_3	H	H

Figure 1.6. Molecular structures of vitamin E stereoisomers.[57]

Among the two groups, α–tocopherol, specifically the RRR–α–tocopherol stereoisomer, is the most biologically relevant and most bioavailable form of vitamin E in the body. Synthetic α–tocopherol is less bioavailable i.e. usable in the body but much less potent as natural RRR–α–tocopherol. Animal and human bioavailability studies found natural:synthetic α–tocopherol of 2:1 (synthetic having half the bioavailability of natural).[58–60] Additionally, according to literature, natural antioxidants are more effective in preventing chronic diseases, while synthetic antioxidants are preferred in the preservation of lipid food products.[61] The extent of its bioavailability has also shown to vary from person to person, for example, individuals with chronic liver disease and cystic fibrosis have reduced intestinal absorption of lipid-soluble nutrients resulting in a biochemical deficiency of vitamin E.[62] In general, its higher bioavailability and reduced metabolism compared to other forms is largely due to the presence of the hepatic α–tocopherol transfer protein.[63] This protein selectively binds to α–tocopherol, storing and transporting it in the plasma and most tissues, where it is approximately 50 times more concentrated than the other stereoisomers of vitamin E.[63]

1.4.3. Role in Membranes

α–Tocopherol is a crucial component of biological membranes due to its lipid-soluble nature. One of the primary roles of α–tocopherol in membranes is protecting cells from oxidative damage. Oxidative damage can occur when the body is under oxidative stress, in other words there are more free radicals (up to an unhealthy level) than antioxidants present. This alters the composition of cell membranes and can induce several human diseases.[64] The body can enter a state of oxidative

stress for a number of reasons including, environmental pollution, smoking, sun exposure, alcohol consumption, and stress, amongst other triggers. As an antioxidant, α–tocopherol was initially demonstrated to protect fats and oils[65] from oxidation and later shown to protect polyunsaturated fatty acids and esters by scavenging free radicals to prevent lipid peroxidation.[66,67] Lipid oxidation was initially studied in relation to food deterioration, as oxidative changes can alter nutritional value and produce toxic compounds.[68] Subsequently, lipid peroxidation and its byproducts in the body were linked to numerous diseases, including cancer, diabetes, cardiovascular, neurological, and various inflammatory diseases.[69] α–Tocopherol can play a regulatory role in some signal transduction enzymes such as those involved in proliferation, apoptosis, survival, inflammation, secretion, adhesion, autophagocytosis, gene expression, etc. A deficiency in vitamin E may contribute to the development of some human diseases.[70] It has shown to modulate signal transduction by modulating enzyme-membrane interactions which overall affects signal transduction pathways on a molecular level.[70]

1.4.4. Exogenous Occurrence (or uses)

α–Tocopherol is used in diet, supplements, pharmaceutical applications, cosmetics, food preservation, and industrially. The recommended daily value intake for vitamin E depends on sex and age, however the average intake is 15 mg for adults.[71]

The most common foods enriched in α–tocopherol provide between 0.6 mg to 7.4 mg per serving, making it challenging to meet daily requirements through diet alone (for some individuals), therefore, α–tocopherol dietary supplements are available.[72] Dietary supplements, which provide nutrients that are not consumed in sufficient quantities, are available in both naturally occurring RRR–α–tocopherol and synthetic forms. These supplements are offered as capsules, tablets, liquids, and/or gummies. D–α–tocopherol polyethylene glycol 1000 succinate (TPGS) is a water-soluble natural vitamin E derivative.[73] TPGS is used in pharmaceutical applications for improving the targetability and bioavailability of many drugs[74], combatting cardiovascular and metabolic disorders[74], beneficial anti-cancerous properties (preventing cancer cell proliferation, altering growth factors, etc)[75] , among others. Besides its pharmaceutical applications, vitamin E is commonly incorporated into skincare products for its photoprotective effect against ultraviolet-induced free radical damage to skin[76,77] and anti-aging benefits, which include enhancing collagen synthesis and preventing collagen degradation[78,79]. α–Tocopherol also plays a role in food quality

and is added to some foods to ensure their safety. It is used in oils to stop the oxidation of fatty acids, extending the shelf life and increase stability of foods subjected to increased temperatures.[80] Building on this, α–tocopherol is also employed industrially in the production of polyethylene[81], the most widely used plastic in food packaging[82]. It performs two actions, stabilizes the polymer during processing and extends the food's shelf life by migrating from the packaging into the food itself and works as an antioxidant.[81,83]

1.5. Model Membranes Using α–Tocopherol

Studies on model membranes reveal significant insights into the interactions and behavior of α–tocopherol and phospholipids. One study shows the mixed system of DPPC and α–tocopherol, where the α–tocopherol adopts a conformation state resembling collapse but retains a distinct phase within the membrane.[84] This formation is supported by the high hydrophobicity of the of α–tocopherol molecule, preventing it from dissolving in water. Compression isotherms of mixed monolayers of saturated lipid, dipalmitoylphosphatidylcholine (DPPC), diunsaturated lipid, dioleoylphosphatidylcholine (DOPC), and monounsaturated lipid, palmitoyl oleoyl phosphatidyl choline (POPC) with α–tocopherol, showed the strength of attractive interactions between phospholipids and α–tocopherol increased with higher chain unsaturation in the order: DOPC > POPC > DPPC.[84] Next, densitometry measurements and small-angle X–ray scattering showed favorable interactions between α–tocopherol and unsaturated phospholipids, with these interactions also correlating to increased lipid chain unsaturation. The addition of α–tocopherol caused minor changes in unsaturated lipid samples, with no significant structural perturbation. This aligned with observations that α–tocopherol sits deeper in DOPC membranes.[85]

The antioxidant activity of α–tocopherol has shown to be strongly correlated with its physical location in a lipid bilayer.[86,87] It was demonstrated that the reduction of reactive oxygen species and lipid radicals by α–tocopherol occurs specifically at the membrane's hydrophobic/hydrophilic interface.[87] The physiological amount of vitamin E in membranes ranges from 0.1 mol % to 1 mol % of phospholipids.[88] Despite its low in vivo concentrations, α–tocopherol intercepts free radicals near the hydrophobic/hydrophilic interface and effectively terminates lipid peroxyl radical oxidation chain reactions deeper within the membrane. Further investigations using deuterium-labeled α–tocopherol reveal that it remains upright in the phosphocholine bilayers but has a

different positioning in bilayers depending on lipid chain unsaturation. The reactive –OH group is positioned near the hydrophobic/hydrophilic interface. In monounsaturated POPC membranes, the –OH of α–tocopherol submerges less than in diunsaturated DOPC membranes, indicating a preference for localization near oxidizable bonds, enhancing its antioxidant activity.[86] Building on this, α–tocopherol was shown to penetrate more readily into mixed monolayers of phospholipids as unsaturation increases.[89]

Interestingly, α–tocopherol plays a role in membrane stability during freezing conditions of plants, particularly the chloroplast thylakoid lipids.[90] α–Tocopherol significantly influences membrane dynamics and stability by interacting with the cryoprotectant sucrose.[90] The study reveals that α–tocopherol concentration in the thylakoid adapts to environmental conditions, preventing membrane destabilization under stress conditions like low temperature and drought.[90] On a different note the effects of α–tocopherol on phospholipid monolayer curvature was studied by X–ray diffraction.[91] Monolayers of 50 mol % α–tocopherol added in dioleoylphosphatidylethanolamine (DOPE) showed one of the highest negative curvatures with a curvature radius of −13.7 Å.[91] The study found the addition of α–tocopherol increases the inward curvature, which produces stress in bilayer membranes, thus affecting membrane interactions. This curvature stress results from the addition of relatively more mass to the hydrocarbon portion of the membrane monolayers than to the polar portion.[91]

1.6. Research Objectives

The first part of this work focuses on the impacts of vaping additives α–tocopherol (vitamin E) and α–tocopherol acetate (vitamin E acetate) on a synthetic lipid-based model lung surfactant membrane composed of zwitterionic DPPC and anionic POPG across additive concentrations ranging from 1 mol % to 20 mol %. The model lung surfactant used in this study offers the optimal balance of saturated, unsaturated lipids, as well as charge found in the innate lung surfactant. This study aims to understand how the lung surfactants surface activity, film morphology and film structure is affected in the presence of these additives and how they may lead to lung injury.

The next part of this work explores the interactions between α–tocopherol and the individual components of the model lung surfactant membrane, DPPC and POPG, that are also common membrane lipids. This study aims to characterize the mixing behavior of α–tocopherol with these

lipids and add to the conversation of our understanding of its antioxidant role in membranes and synergy with different lipids.

For all systems, the techniques to study the surface activity, and morphology of the model membranes, include the Langmuir balance, Brewster angle microscopy (BAM), and atomic force microscopy (AFM). Additionally, the sensitive synchrotron-based X–ray surface characterization techniques are used to study the liquid crystalline structure of the mixed monolayers, specifically grazing incidence X–ray diffraction (GIXD) and X–ray reflectivity (XR). All techniques are summarized in section 1.7.

1.7. Experimental Techniques for Studying Model Membranes

This review will introduce and discuss some key biophysical techniques for studying monolayer films surface activity, film morphology, and film structure.

1.7.1. Langmuir Film Balance

Figure 1.7. depicts a generic representation of a surface pressure-area compression isotherm which is obtained with a Langmuir trough that consists of a shallow rectangular trough filled with a liquid of choice and two movable barriers that compresses or expands the surface area of the liquid.

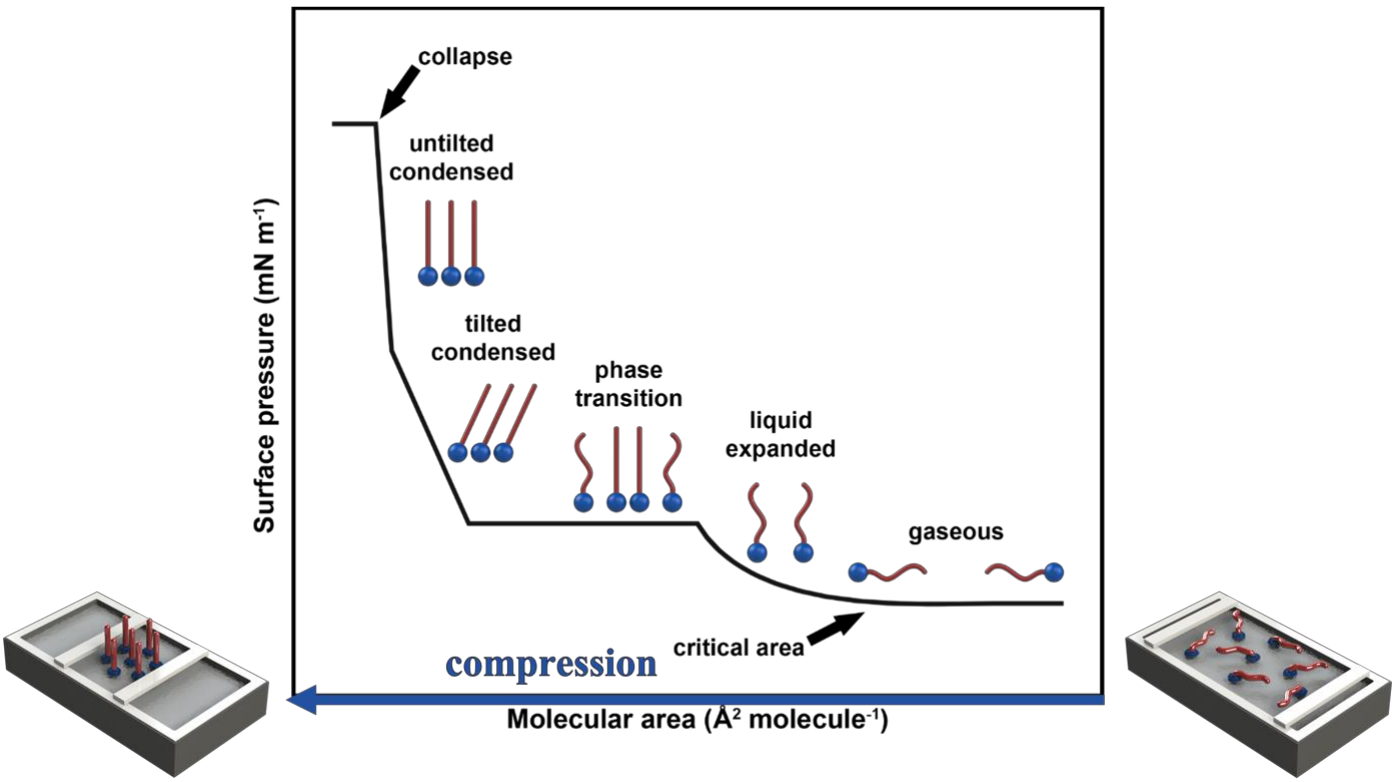

Figure 1.7. Generic representation of a Langmuir surface pressure-area compression isotherm depicting various phases in the isotherm with corresponding Langmuir rectangular trough in a compressed form (left) and expanded form (right).

The isotherm shows the relationship between surface pressure and the molecular area per molecule for a monolayer of lipids. As compression increases, the surface pressure also increases because the lipids are being forced closer together causing interactions among them. The transitions through the standard phases in a lipid monolayer are analogous to the three-dimensional (3D) phases. The first phase is the gaseous phase where the lipid molecules are far enough apart with minimal to no interaction. Then is a liquid expanded (LE) phase where the lipid molecules are closer together, interacting more but still have significant freedom of movement such that the lipid chains behave like liquid alkanes. Next is a two-phase co-existence (phase transition) of the LE and the condensed phase. At the point of phase co-existence, the surface pressure remains constant with further compression of the monolayer because there is a redistribution of the molecules between the two phases. After this phase transition there is the tilted and/or untilted condensed phase, where lipid molecules pack closely together, and the lipid chains exhibit liquid crystalline ordering. The condensed phase is analogous to a 3D solid, where molecules are in fixed positions

in a crystal lattice and in an ordered structure. Lastly is the collapse of the monolayer that occurs when the molecular area becomes too small to accommodate all the lipids in the monolayer. This prompts the formation of 3D aggregates or submersion of lipids and/or other molecules into the subphase.

1.7.2. Brewster Angle Microscopy (BAM), Microscopic View

The real-time visualization of monolayers at the air-liquid interface with BAM was first introduced and observed in 1991[92,93] and since then has become a standard technique for the imaging of films. This method is coupled with a Langmuir trough, where a thin film is spread onto a liquid surface and imaged *in situ* by BAM during the film's compression. This technique is performed for the visualization of thin films and particularly useful for studying Langmuir monolayer film morphologies like lung surfactants at the microscopic level. Information such as the lateral organization can be obtained, including phase separation and domain formation.[94] It employs a laser beam set at Brewster's angle of 53°, defined by the refractive index of the two phases being air and water (substrate or subphase) present at the interface shown in Figure 1.8a.

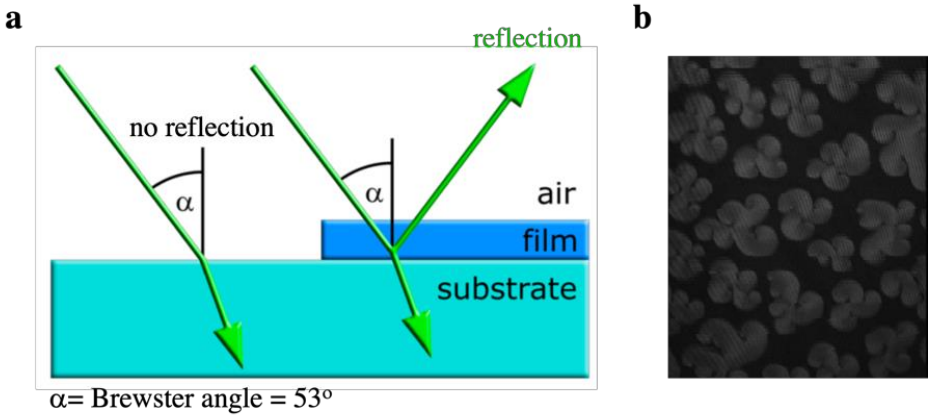

Figure 1.8. (a) Schematic representation of the interaction of polarized light perfectly reflected through the subphase at Brewster's angle of 53° (left) and when the Brewster angle is deviated in the presence of a thicker film morphology (right). (b) Example of a BAM image showing the thick light regions and less thick dark regions.

At this angle the polarized light is perfectly transmitted through the subphase without reflection (Figure 1.8a). Variations in the Brewster angle across the sample create light and dark phases, reflecting thickness differences in the film as depicted in Figure 1.8b. The BAM image shows light regions attributed to the thicker condensed phase lipid molecules and dark regions attributed to

less thick LE phase lipid molecules. A limitation of BAM is that film morphologies must be beyond its lateral resolution of 1 μm to be visible.

1.7.3. Atomic Force Microscopy (AFM), Nanoscopic View

In 1986, Gerd Binning, Calvin Quate and Christopher Gerber invented the atomic force microscope (AFM)[95] to investigate the morphology of films using the Langmuir-Blodgett (LB) method. The LB method was developed by Irving Langmuir and Katharine Blurr Blodgett and allows for the controlled transfer of a monolayer at the air-liquid interface onto a solid substrate, as illustrated in Figure 1.9. During the LB transfer process, the surface pressure is kept constant by adjusting the barriers to compensate for the loss of molecules being transferred to the solid substrate, thus preserving the target pressure.

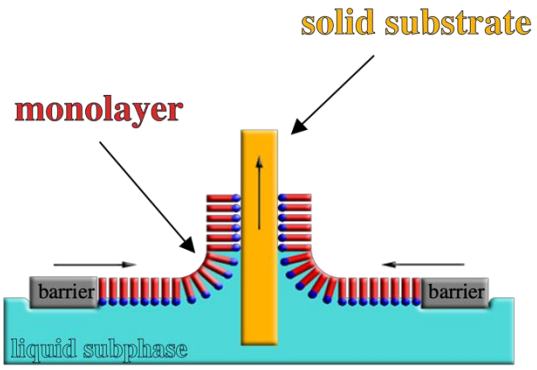

Figure 1.9. Schematic of Langmuir-Blodgett (LB) method deposition.

After sample acquisition and once the film has dried, AFM in the peak force tapping variant called ScanAsyst imaging mode is used. This mode automatically optimizes all scan parameters, such as setpoint and feedback response, without user intervention, to characterize the surface morphology at the nanoscale level. This technique generates high-resolution images that provide spectroscopic information at each pixel; the more the pixels scanned, the higher the image resolution. It also allows direct control of the tip-sample interaction force, protecting the sample and preserving the tip's sharpness for longer. A sharpened intact tip is critical for AFM sample analysis for several reasons including: more precise measurements, accurate topographical data, and reduces tip artifacts. AFM complements BAM, which offers a non-destructive analysis, lateral resolution below 1 μm, and quantitative measurements, such as the ability to accurately measure the thickness

of different parts of the film. The pairing of the LB method and AFM enables detailed characterization of monolayer films at the nanoscale level.

1.7.4. X–Ray Techniques

This review will focus on X–ray techniques, namely, GIXD and XR, for studying monolayers in real-time (Figure 1.10). These techniques provide detailed structural information and insights into molecular organization at the air-water interface.

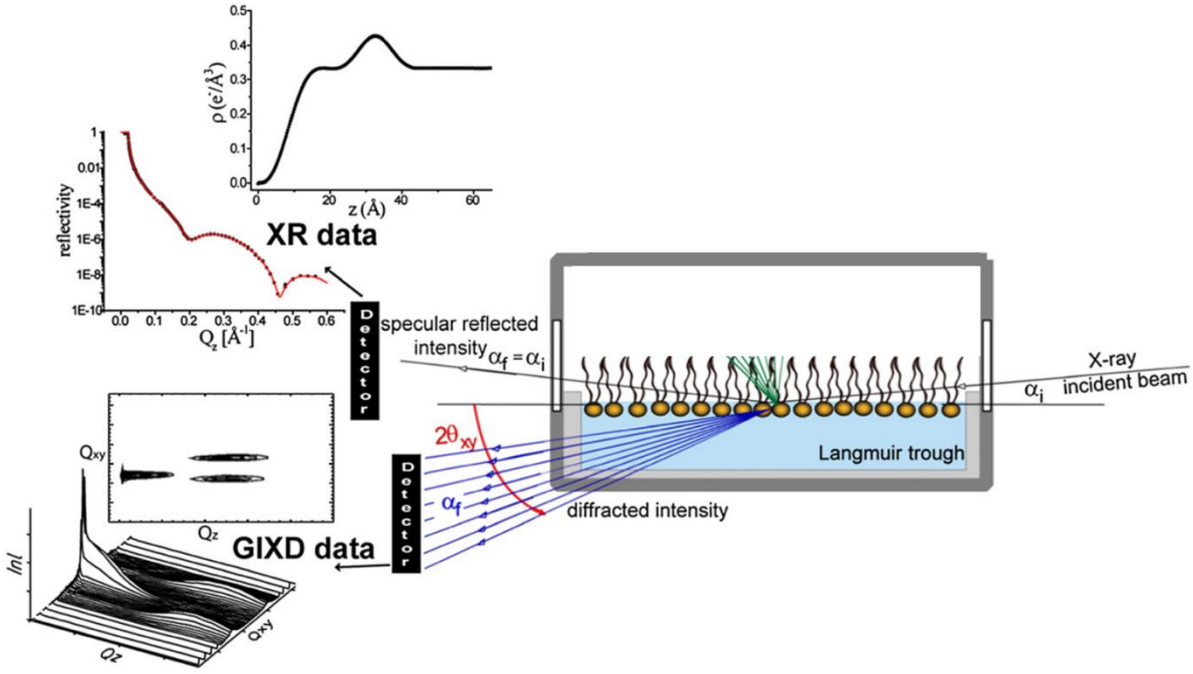

Figure 1.10. Working principles of two X–ray methods, including GIXD and XR, used for monolayers at the air-liquid interface. Figure adapted from[96].

1.7.4.1. Grazing Incidence X–Ray Diffraction (GIXD)

GIXD focuses on the condensed phase molecules where structural changes can be observed *in situ*.[97,98] This technique examines the molecular ordering within the plane of the interface, providing insights into the surface crystallization of monolayers and revealing the influence of certain ordered chain structures and in some cases headgroups. The experimental setup involves a complex X–ray diffraction apparatus coupled with a large Langmuir trough placed in a Helium-flushed container (to remove oxygen and reduce background scattering) with kapton windows transparent for X–rays.[99] The GIXD experimental setup used in this work is shown in Figure 1.11.

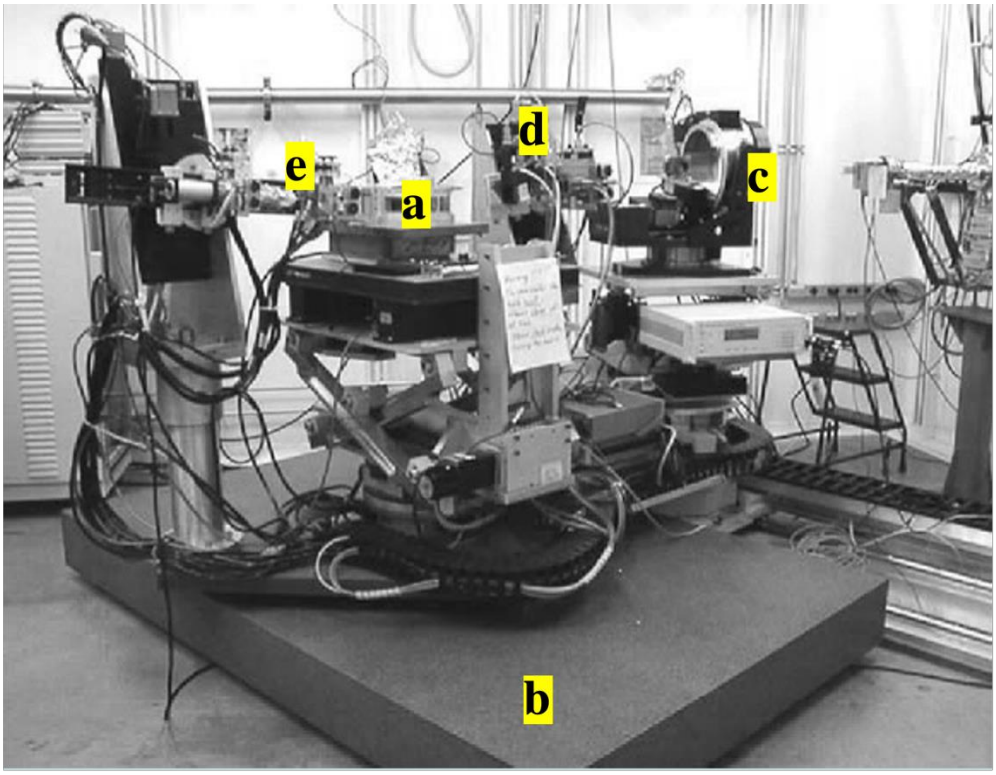

Figure 1.11. GIXD experimental setup at the beamline 15-ID-C ChemMatCARS of the Advanced Photon Source (APS) at Argonne National Laboratory involving (a) enclosed Langmuir trough, (b) antivibration platform, (c) germanium crystal for beam redirection, (d) incident X–ray beam slits, (e) position sensitive Pilatus detector.

In this method, an X–ray beam with a defined wavelength is directed at the subphase at a specific incident angle (α_i), where it is reflected at an angle (α_f) off the surface of the subphase, in other words total reflection. This total reflection allows for the measurement of both the scattering vectors Q_{xy} (lateral) and Q_z (vertical). The X–rays penetrate up to 8 nm of depth into the monolayer material[97], making this method highly surface sensitive. GIXD provides information about the two-dimensional (2D) crystallites oriented on the subphase, attributed to the condensed phase of monolayers. This method gives quantitative molecular-level details on the condensed phase such as lattice spacing (crystallographic orientation), phospholipid chain tilt angle, and thicknesses. It is important to note that disordered or unstructured lipids in a LE phase do not contribute to the GIXD signal but can be studied using other X–ray methods such as X–ray reflectivity which is not limited to phase state and will be discussed in more detail in section 1.7.4.2.

The diffraction signal or pattern observed for a given condensed phase is resolved as a contour plot with both scattering vectors, Q_{xy} and Q_z, for all monolayers (Figure 1.10). The positions in Q_{xy}

give information about the lattice while positions in Q_z give information about the chain-tilt of condensed phase lipid molecules. The positioning and intensities of the diffraction signals at defined directions are influenced and characterized by the ordering of various components such as, alkyl chains or, less often, the headgroup packing.

1.7.4.2. X–Ray Reflectivity (XR)

XR at the air-liquid interface offers the vertical information using vertical scattering vector Q_z for monolayers in both the structured condensed and unstructured liquid-expanded phases. For this technique an X–ray beam strikes the surface at an incident angle α_i then after interaction is reflected at an angle α_f, where $\alpha_i=\alpha_f$ due to the law of reflection (Figure 1.10).[96] Varying the α_i probes different depths of the monolayer sample and simultaneously collects the intensity of the reflected X–rays at α_f over a range of α_i, thereby obtaining the reflectivity (R) across this range. The vertical scattering vector Q_z parameter is given by the formula:

$Q_z = \frac{4\pi}{\lambda}\sin(\alpha_f)$, where l is the wavelength of the X–rays

Equation 1.1. Formula for scattering vector component (Q_z).[100]

To obtain a reflectivity curve as seen in Figure 1.10, R and Q_z are plotted against each other. This curve is then fitted using a slab model[96] to obtain vertical information on the monolayer such as the film thickness in Angstroms, electron density (r), and surface roughness at distinct layers (slabs) within the film or at interfaces, where the refractive index and X–ray wavelength vary depending on the slab. The monolayers studied in this work are primarily composed of phospholipids. Figure 1.12 shows the four slabs typically analyzed in terms of thickness and electron density in XR for a phospholipid monolayer at the air-liquid interface.

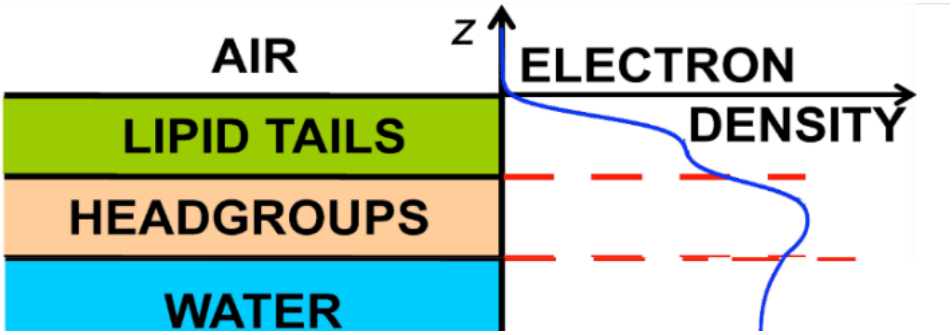

Figure 1.12. Cartoon for four-slab XR fiiting model (air, lipid tail, headgroups, water) of typical phospholipid monolayer. Figure adapted from[100].

1.8. Outline of Manuscripts

Two manuscripts are included in this research (Chapters 2, & 3):

The first manuscript (Chapter 2) focuses on the physicochemical impacts of increasing amounts of vaping additives associated with EVALI, vitamin E and vitamin E acetate, on a lipid-only model lung surfactant. This manuscript was published in the journal Langmuir. Full citation found below:

Understanding the Retention of Vaping Additives in the Lungs: Model Lung Surfactant Membrane Perturbation by Vitamin E and Vitamin E Acetate. Panagiota Taktikakis, Mathieu Côté, Nivetha Subramaniam, Kailen Kroeger, Hala Youssef, Antonella Badia, and Christine DeWolf. Langmuir 2024 40 (11), 5651-5662. DOI: 10.1021/acs.langmuir.3c02952

The second manuscript (Chapter 3) provides a more detailed study on the interaction of membrane-soluble vitamin E with the individual components of the lipid-only model lung surfactant studied in Chapter 2. These lipids are also common membrane lipids. This manuscript has been prepared for submission to the journal BBA Biomembranes.

Chapter 2. Understanding the Retention of Vaping Additives in the Lungs: Model Lung Surfactant Membrane Perturbation by Vitamin E and Vitamin E Acetate

2.1. Abstract

Deviations from the normal physicochemical and functional properties of pulmonary surfactant are associated with the incidence of lung injury and other respiratory disorders. This study aims to evaluate the alteration of the 2D molecular organization and morphology of pulmonary surfactant model membranes by the electronic cigarette additives α–tocopherol (vitamin E) and α–tocopherol acetate (vitamin E acetate), which have been associated with lung injury referred to as e-cigarette or vaping use-associated lung injury (EVALI). The model membranes used contained a 7:3 molar ratio of DPPC (1,2-dipalmitoyl-sn-glycero-3-phosphocholine) and POPG (1-palmitoyl-2-oleoyl-sn-glycero-3-phosphoglycerol) to which α–tocopherol and α–tocopherol acetate were added to form mixtures of up to 20 mol % additive. The properties of the neat tocopherol additives and DPPC/POPG (7:3) mixtures with increasing molar proportions of additive were evaluated by surface pressure–area isotherms, excess area calculations, Brewster angle microscopy, grazing incidence X–ray diffraction, X–ray reflectivity, and atomic force microscopy. The addition of either additive induces a fluidization of the model lung surfactant membrane, generating a greater proportion of fluid phase and thus altering the essential phase balance of the model pulmonary surfactant membrane. Despite this net fluidization, both tocopherol additives have space-filling effects on the liquid-expanded and condensed phases, yielding negative excess areas in the liquid-expanded phase and reduced tilt angles in the condensed phase. Both tocopherol additives alter the stability of the fluid phase, pushing the eventual collapse of this phase to higher surface pressures than the model membrane in the absence of an additive.

2.2. Introduction

The use of electronic cigarettes or ‘vaping’ has grown significantly in popularity in recent years. At the start of 2019, a marked increase in the incidence of serious lung injuries associated with vaping in young adults, with no pre-existing respiratory diseases challenged the common

perception that vaping is a healthier alternative to smoking.[43] The medical condition of these young adults with lung injuries was labeled by the Centers for Disease Control and Prevention (CDC) as electronic cigarette or vaping product use-associated lung injury (EVALI). The CDC announced that this outbreak was strongly linked to the presence of α–tocopherol acetate (vitamin E acetate), a diluent in vaping solutions containing tetrahydrocannabinol. α–Tocopherol acetate was detected in bronchoalveolar lung lavage specimens from 94% of patients presenting with EVALI.[41,43] Current evidence is insufficient to rule out other contributing factors, but the molecular mechanism of lung injury from α–tocopherol (vitamin E) and its acetate form on the lungs requires further understanding.

Most of the literature on α–tocopherol–lipid interactions focus on the miscibility of α–tocopherol in membrane bilayers to determine its preferential association with either saturated or unsaturated lipids in order to understand its biological importance as an antioxidant. DiPasquale *et al.* proposed that α–tocopherol more readily associates with disordered phospholipid environments, exhibiting a reduced partial molar volume in bilayers and favorable intermolecular interactions that correlate with the degree of chain unsaturation.[101] Jurak *et al.* studied monolayer models consisting of binary mixtures of α–tocopherol (20 to 75 mol %) and different phosphocholines, namely dipalmitoylphosphatidylcholine (DPPC), palmitoyloleoylphosphatidylcholine (POPC), and dioleoylphosphatidylcholine (DOPC).[84] They also concluded that there is a correlation between the degree of unsaturation and the strength of the attractive interactions, with the diunsaturated DOPC exhibiting the strongest interactions, followed by the monounsaturated POPC, and then the saturated DPPC. However, despite these different interaction strengths, α–tocopherol showed a tendency to partially mix with all phosphocholines, regardless of their unsaturation level.

In contrast to the experimental findings, molecular dynamics simulations by Leng *et al.* suggest that α–tocopherol preferentially associates with monounsaturated over polyunsaturated phospoholipids.[102] This preferential association with monounsaturated compared to polyunsaturated phospholipids is similar to the behaviour of cholesterol, except that cholesterol shows an even greater affinity for saturated over monounsaturated phospholipids. Muddana *et al.* showed by computing the radial pair density of α–tocopherol in 1:1 mixtures of DPPC and diundecanoylphosphatidylcholine (DUPC) that α–tocopherol preferentially partitions to the phase boundary between the gel and fluid phases (under conditions of phase separation), thus acting as a lineactant.[103] They also noted that the previously reported preferential association of tocopherol

with polyunsaturated fatty acid chains may not be generalizable and is also influenced by the positions of the units of unsaturation. Lineactants lead to the reduction of the line tension, favoring the formation of smaller domains. Experimental studies also suggest that α–tocopherol exhibits lineactant properties at added concentrations above 10 mol %.[101]

Pulmonary surfactant consists of approximately 90% by weight of lipids, of which 70-80 mol % are saturated (with zwitterionic DPPC as the major component) and 30% are unsaturated with a high proportion of anionic phosphoglycerols such as palmitoyloleoylphosphatidylglycerol (POPG).[104] Binary mixtures of DPPC and POPG are commonly used as model membranes[26,105–107] because they mimic the saturated–unsaturated balance, the charged nature, the phase separation and many of the functional properties of natural pulmonary surfactant extracts. Such simplified lipid-only models allow us to probe the interaction of α–tocopherol, a lipid analogue, with the various phospholipid phases formed in monolayer films. In this work we have studied the impact of both α–tocopherol and its acetate form on the surface activity, morphology, compressibility and structure of a model pulmonary surfactant membrane.

2.3. Experimental (Materials & Methods)

Materials. 1,2-dipalmitoyl-*sn*-glycero-3-phosphatidylcholine (DPPC, 99%) and 1-palmitoyl-2-oleoyl-phosphatidylglycerol (POPG, 99%) were purchased from Avanti Polar Lipids in powder form. α–Tocopherol, α–tocopherol acetate (both 96%), tris(hydroxymethyl)aminomethane (Tris, 99.8%) and NaCl (99%) were purchased from Sigma-Aldrich. ACS grade chloroform (Fischer Scientific) was used to prepare the phospholipid and additive stock spreading solutions. All reagents were used without further purification. The molecular structures of the phospholipids and additives are shown in Figure 2.1.

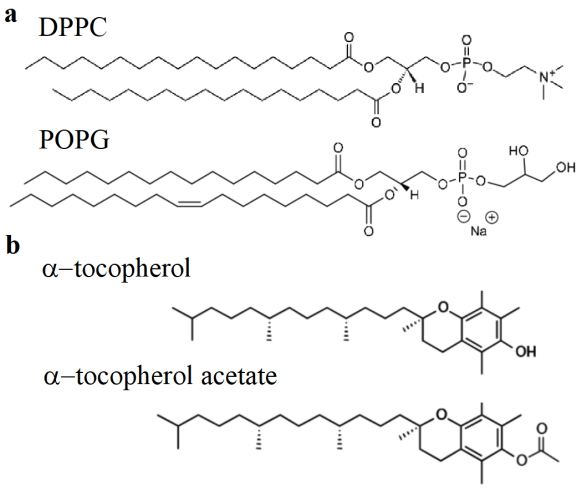

Figure 2.1. Molecular structures of the (a) phospholipids (DPPC and POPG) and (b) additives α–tocopherol/α–tocopherol acetate, also known as vitamin E/vitamin E acetate) used in this work.

Lipid Mixtures and Aqueous Subphases. Stock solutions of 1.0 mM DPPC and 1.0 mM POPG in chloroform were combined to prepare a solution containing a 7:3 molar ratio of DPPC and POPG. Stock solutions of α–tocopherol (1.0 mM) and α–tocopherol acetate (1.0 mM) in chloroform were combined with the DPPC:POPG (7:3) solution to prepare solutions containing 1 mol %, 5 mol %, 10 mol %, 15 mol %, and 20 mol % of α–tocopherol or α–tocopherol acetate and 99 mol %, 95 mol %, 90 mol %, 85 mol %, and 80 mol % DPPC:POPG (7:3), respectively. Tris-buffered saline (TBS) comprising 50 mM Tris and 150 mM NaCl served as the aqueous subphase for all Langmuir monolayer experiments and was prepared with ultrapure water (resistivity of 18.2 MW cm), and pH adjusted to 7.4 using hydrochloric acid.

Surface Pressure–Molecular Area Isotherms. Surface pressure–molecular area isotherms were obtained using a Langmuir film balance (Model 516, Nima Technology) with maximum trough surface area of 80 cm^2 and a filter paper Wilhelmy plate (Whatman No. 3001-604). Neat α–tocopherol, neat α–tocopherol acetate, DPPC:POPG (7:3), and their mixtures were spread on the TBS subphase and the solvent was allowed to evaporate (10 min) prior to lateral symmetric compression of the film at the air-aqueous interface at a rate of 5 cm^2/min (equivalent to 6 to 7.5 $Å^2$/molecule/min, depending on the film). All experiments were conducted at room temperature (22.5 ± 0.5 °C) and at least three separate isotherms were obtained for each lipid composition to

ensure reproducibility. Previous reports[108] have shown that the phase behaviour of the model membranes at room temperature to be qualitatively similar to those at physiological temperatures, albeit with the phase transitions shifted to lower surface pressures.

The impact of lipid composition on molecular mixing was assessed from changes to the average molecular area. The ideal mixing molecular area at a given pressure is calculated from the weighted average of the measured molecular areas of the DPPC:POPG (7:3) mixture and either neat α–tocopherol or α–tocopherol acetate. The excess molecular area (deviation from the ideal molecular area) can be calculated as follows:

$$A_{ideal} = (1 - x_{additive}) \times A_{DPPC:POPG\ (7:3)} + x_{additive} A_{additive}$$

Equation 2.1. Ideal molecular area of mixed monolayer system.

$$A_{excess} = A_{measured} - A_{ideal}$$

Equation 2.2. Excess molecular area.

where, $x_{additive}$ is the mole fraction of additive in the mixture, $A_{DPPC:POPG\ (7:3)}$ is the molecular area of DPPC:POPG (7:3) at a given pressure, $A_{additive}$ is the molecular area of the neat additive monolayer at a given pressure, $A_{measured}$ is the experimental molecular area of DPPC:POPG (7:3) with additive, and A_{ideal} is the ideal mixing molecular area.

Brewster Angle Microscopy (BAM) Imaging. BAM imaging of monolayers at the air-aqueous interface during barrier compression was performed using an I-Elli2000 imaging ellipsometer (Nanofilm Technologies) coupled to a Langmuir film balance (Model 601BAM, Nima Technology) with a maximum trough area of 146 cm^2. The instrument is equipped with a 50 mW Nd:YAG laser (λ=532 nm), and the images were captured using a 20× objective (with a field of view of 220 μm × 275 μm and lateral resolution of approximately 1 μm) at the Brewster incident angle of 53.15°. Following a wait time of 10 min for solvent evaporation after spreading of the lipid solution, the monolayer was symmetrically compressed at a rate of 5 cm^2/min. All BAM images were obtained at 50% laser brightness intensity, except for the images of the neat α–tocopherol and α–tocopherol acetate monolayers that were obtained at 70% intensity.

Langmuir monolayer transfer onto mica substrate. Monolayer films were vertically transferred on the upstroke from the air–aqueous interface onto freshly-cleaved mica using the Langmuir–Blodgett technique. The monolayer was compressed and held for five minutes at the target pressure prior to transfer at a rate of 5 mm/min. The solid-supported films were allowed to dry under ambient conditions for 30 min and imaged by AFM within 24 h of their preparation.

Atomic force microscopy (AFM). A MultiMode 8HR scanning probe microscope (Bruker Nano, Santa Barbara, CA) was used to capture AFM images in Peak Force Tapping Mode in air with silicon tips mounted on nitride levers of nominal spring constant of 0.4 N/m and resonance frequency of 70 kHz (Model Scanasyst-Air, Bruker AFM Probes). Images were recorded at a scan rate of 0.759 Hz and 512 × 512-pixel resolution and processed with Nanoscope software version 2.0. The condensed phase domains were identified by applying a height threshold and bearing analysis used to determine the percent area coverage of condensed phase. Analyses were performed on at least three images randomly selected across multiple samples.

Grazing incidence X–ray diffraction (GIXD). The GIXD experiments were performed at the beamline 15-ID-C ChemMatCARS of the Advanced Photon Source (APS) at Argonne National Laboratory with the following parameters: X–ray beam wavelength of 1.239 Å, incidence angle of 0.0906°, horizontal size of 20 μm, and vertical size of 120 μm, leading to a beam footprint of 2 × 10^{-3} cm by 7.6 cm. The detector used was the 2D Swiss Light source PILATUS 100 K set to single-photon counting mode. Two sets of slits, one placed in front of the detector to control the beam footprint and the other placed 280 μm from the sample, were used to minimize intense low-angle scattering. Experiments were performed at the air–aqueous interface of a 340 cm^2 Langmuir trough with a compression rate of 5 cm^2/min. The measured GIXD data is plotted as contour plots of the intensity as a function of both the horizontal (Q_{xy}) and the vertical (Q_z) scattering vector components. The lattice spacing d_{hk} was obtained from the in-plane diffraction data as $d_{hk}= 2p/Q^{hk}_{xy}$, where the Miller indices h, k were used to index the Bragg peaks needed to calculate the unit cell parameters for the in-plane lattice. The full width at half maximum (fwhm) of the Bragg peaks after correction for the instrumental resolution (0.0084 $Å^{-1}$) was used to calculate the in-plane correlation length using the Scherrer formula as follows:

$$\xi_{xy} = 0.9 \times {}^{2\pi}/_{fwhm_{intrinsic}(Q_{xy})}$$

Equation 2.3. Scherrer formula.

GIXD experiments were performed at lateral surface pressures of 10 mN/m, 18 mN/m, 35 mN/m, and 45 mN/m, and at a temperature of 22.0 ± 0.5 °C.

X–ray reflectivity (XR). XR is measured as a function of the vertical scattering vector component (Q_z). XR probes the electron density variation ρ(z) of the vertical structure of the layers at the air-aqueous interface. The monolayer was modeled as a stack of slabs, with each slab having a constant thickness and electron density. The electron density profile ρ(z) was laterally averaged over both the ordered and disordered parts of the monolayer under the footprint of the X–ray beam.

The X–ray reflectivity data was analyzed using an open-source (Python) software developed and provided by Wei Bu, beamline scientist at ChemMatCARS. The measured X–ray reflectivity $R(Q_z)$ is normalized by the Fresnel reflectivity $R_F(Q_z)$, which is calculated for a sharp air-aqueous interface. The X–ray reflectivity was calculated using the Parratt method. Nonlinear least-squares fitting was used to determine the minimum number (N^{-1}) of internal slabs to best fit the X–ray reflectivity data. In our XR data analysis, all systems were treated as a homogeneous monolayer film although lateral phase separation occurs under the experimental conditions. This assumption was made based on the sizes of the condensed and liquid-expanded phases, which are less than the footprint of the X–ray beam in all our systems. This assumption has been previously used in the literature, where the domain sizes of the phase-separated patches are smaller than the X–ray beam footprint.[109] All XR experiments were performed at a lateral surface pressure of 35 mN/m and at a temperature of 22.0 ± 0.5 °C.

2.4. Results & Discussion

2.4.1. Surface Pressure–Molecular Area Isotherms

The compression isotherms of the model lung surfactant mixture DPPC:POPG (7:3), α–tocopherol, α–tocopherol acetate, and mixtures of DPPC:POPG (7:3) and either α–tocopherol or α–tocopherol acetate are shown in Figure 2.2a,b. For DPPC:POPG (7:3) the onset area is 108 $Å^2$/molecule, while those of α–tocopherol and α–tocopherol acetate are much smaller, 74 and 80 $Å^2$/molecule, respectively. The onset areas of DPPC:POPG (7:3) mixtures containing varying molar concentrations of α–tocopherol or α–tocopherol acetate decreased with increasing concentration of additive, with a more pronounced effect observed with α–tocopherol acetate (Figure 2.2a,b insets). In particular, a shift of the DPPC:POPG isotherm to lower molecular areas is observed in the presence of both additives at concentrations ≥ 10 mol %.

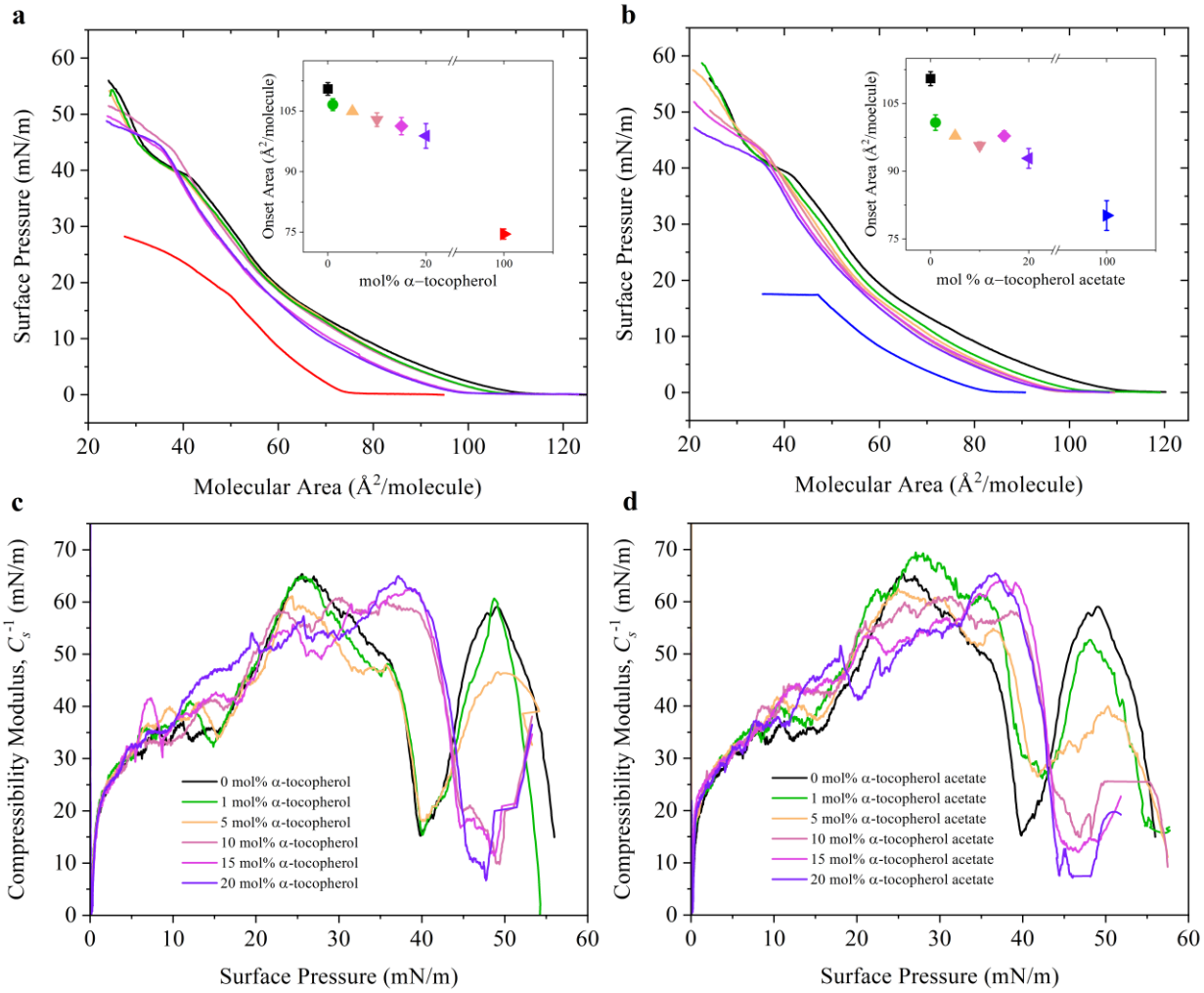

Figure 2.2. UPPER PANELS: Surface pressure–area isotherms for (a) neat α–tocopherol (red) and DPPC:POPG (7:3) mixtures with increasing molar concentrations of α–tocopherol (0 mol %, 1 mol %, 5 mol %, 10 mol %, 15 mol %, and 20 mol %, colours indicated in legend), and (b) neat α–tocopherol acetate (blue) and DPPC:POPG (7:3) mixtures with increasing molar concentrations of α–tocopherol acetate (0 mol %, 1 mol %, 5 mol %, 10 mol %, 15 mol %, and 20 mol %, colours indicated in legend). The insets show the variation in onset area as a function of the mole fraction of additive. LOWER PANELS: The compressibility moduli as a function of the surface pressure for DPPC:POPG (7:3) mixtures with (c) α–tocopherol and (d) α–tocopherol acetate.

DPPC:POPG mixtures are known to phase separate into a DPPC-rich condensed phase and a POPG-rich liquid-expanded phase.[9,30] This phase transition can be difficult to discern from the isotherm but its onset is associated with a minimum in the compressibility modulus versus surface pressure plots (Figure 2.2c,d) observed at around 13 mN/m. Beyond this pressure, the film remains

phase separated until the collapse of the POPG-rich fluid phase, evident as a plateau in the isotherm at 42–45 mN/m, after which the surface pressure increases more steeply until the eventual film collapse at 55–60 mN/m (Figure 2a,b). By contrast, both α–tocopherol and α–tocopherol acetate films collapse at lower pressures, namely below 20 mN/m. An elevated collapse pressure for mixtures of phospholipids and additives compared to the pure additives suggests an interaction between components.[101] The pressure for the collapse of the POPG-rich fluid phase is shifted to higher values in the presence of 10 mol % or more of the additive, indicative of stabilizing interactions between the tocopherol and POPG. α–Tocopherol was shown to have a stabilizing effect on disordered bilayers wherein it suppressed the bilayer thermal expansivity.[85]

A direct comparison of the isotherms for a given concentration of additive is provided in Figure A1. The isotherms of monolayers containing 0 mol %, 1 mol % and 5 mol % of additive are qualitatively similar in shape. At or above 10 mol % of additive, there is a distinct change in the plateau pressure, which is shifted to higher values. As the proportion of additive increases, the slope change associated with the formation of a DPPC-rich condensed phase, which typically occurs around 13 mN/m in DPPC:POPG (7:3), becomes less pronounced in both the isotherm and compressibility plots, suggesting that α–tocopherol and α–tocopherol acetate are fluidizing the condensed DPPC-rich phase, as was observed with monolayers of DPPC and α–tocopherol, wherein the addition of 25 mol % to 75 mol % α–tocopherol results in the disappearance of the liquid-expanded-to-condensed phase transition.[84]

Compressibility moduli (C_s^{-1}) for the neat α–tocopherol and α–tocopherol acetate films are presented in Figure A2 and the maximum C_s^{-1} are 55 mN/m and 47 mN/m, respectively. As a consequence of the methyl branching, the tocopherol phytyl side chains have an inherently larger cross-sectional area than an unbranched chain. Yasmann and Sukharev *et al.* demonstrated that branched alkyl chains, such as DPhPC (diphytanoylphosphatidylcholine) (the branched lipid equivalent of DPPC), exhibited a lower film compressibility modulus of 115 mN/m[110] than DPPC for which the film compressibility modulus can reach values of up to 250 mN/m.[111] Additionally, the shorter chain length of the tocopherols may also contribute to the low compressibility, for example, the 14-carbon saturated DMPC (1,2-dimyristoyl-sn-glycero-3-phosphocholine) exhibits a maximum film compressibility modulus value of 100 mN/m[112] which is lower than that of the 16-carbon DPPC film. At all surface pressures up to collapse, the α–tocopherol film

compressibility modulus is distinctly higher than that of the α–tocopherol acetate film, despite the similarity of the isotherm shapes. This is attributed to the acetate (as opposed to hydroxyl) in the headgroup altering the molecular orientation of the α–tocopherol acetate at the interface. The C=O portion of the ester functional groups present on the headgroups of surface-active molecules has been reported to be mainly oriented parallel to the aqueous surface or subphase.[113] An altered molecular orientation can not only affect the neat film compressibility but also its miscibility with different lipids and monolayer phases.

2.4.2. Deviations From Ideal Mixing

To assess the phospholipid-tocopherol additive interactions in the mixed monolayers, excess molecular areas were calculated for varying molar concentrations of α–tocopherol (Figure 2.3a) and α–tocopherol acetate (Figure 2.3b). Positive deviations suggest repulsive interactions and film expansion while negative deviations indicate attractive interactions and/or condensation.[114] Excess areas were calculated at surface pressures of 1 mN/m to 15 mN/m since monolayers of α–tocopherol and α–tocopherol acetate collapse by 18 mN/m. For the α–tocopherol mixtures, small negative deviations less than 5 $Å^2$/molecule are observed, which decrease as the film is compressed, indicating the presence of attractive interactions between the model membrane and α–tocopherol. In general, it appears that the deviations are more pronounced as the proportion of α–tocopherol increases, however, these increases may not be statistically significant, given the reported errors. We speculate that the additive has a greater space-filling impact on the chains when the molecular spacing is higher. As the film is compressed, the chains naturally extend more and there is less opportunity for the α–tocopherol to space-fill.

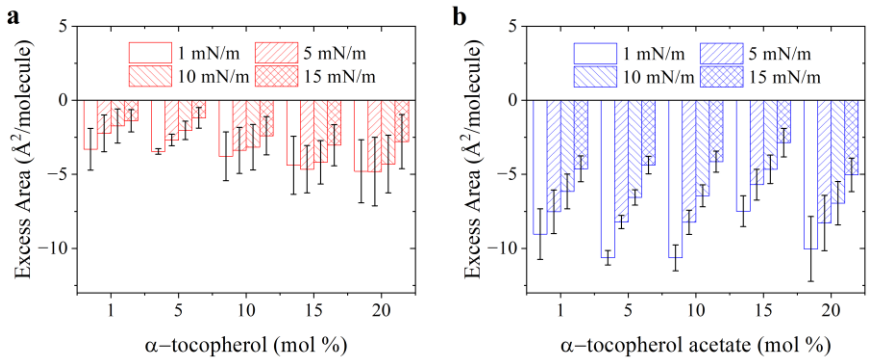

Figure 2.3. Molecular area deviations from the ideal mixing area (excess areas) for DPPC:POPG (7:3) mixtures containing (a) α–tocopherol and (b) α–tocopherol acetate at surface pressures of 1 mN/m, 5 mN/m, 10 mN/m and 15 mN/m. The standard deviations were calculated from triplicate measurements of the surface pressure–molecular area isotherms.

In contrast to α–tocopherol, the addition of just 1 mol % α–tocopherol acetate results in a significant condensing effect with negative excess areas of –9 ± 2 Å^2/molecule, for which the decrease in excess area as the film is compressed is also more pronounced. In summary, increasing the molar concentration of either additive leads to a negative deviation from the ideal mixing molecular areas, with the deviation being more pronounced at lower pressures, i.e., when all components are in the liquid-expanded phase and for mixtures containing α–tocopherol acetate. The substitution of the hydroxyl group with an acetate clearly has a significant impact.

A larger impact of α–tocopherol acetate on DPPC:POPG (4:1), compared to α–tocopherol, was also observed by van Bavel *et al*.[52] Their phospholipid-additive isotherms are however shifted to molecular areas greater than that of DPPC:POPG, despite smaller molecular areas for the single-chain α–tocopherol and α–tocopherol acetate. For comparison purposes, we estimate excess areas of +6 Å^2/molecule (5 mN/m), +9 Å^2/molecule (10 mN/m), and +10 Å^2/molecule (20 mN/m) with just 5 mol % additive using our tocopherol-additive isotherms (since neat α–tocopherol and α–tocopherol isotherms were not reported by the authors). The excess areas will be addressed further in the context of morphology in the next section.

2.4.3. Film Morphology

The morphologies of neat α–tocopherol and α–tocopherol acetate films imaged using BAM are illustrated in Figure 2.4. α–Tocopherol initially forms a homogeneous film at low pressure. At 14 mN/m, small, very low contrast domains begin to appear. As the film is further compressed, the α–tocopherol begins to collapse and 3D aggregates (protrusions) form, evident as bright spots in the BAM images, in agreement with previous studies.[52,84] These protrusions increase in diameter and brightness with compression, a growth pattern that likely leads to the broad collapse over a range of surface pressures observed in the isotherm. AFM images confirm a homogeneous phase below 15 mN/m (Figure 2.5a). The diameter of the protrusions observed at pressures ≥ 15 mN/m directly correlates with the height (Figure 2.5b).

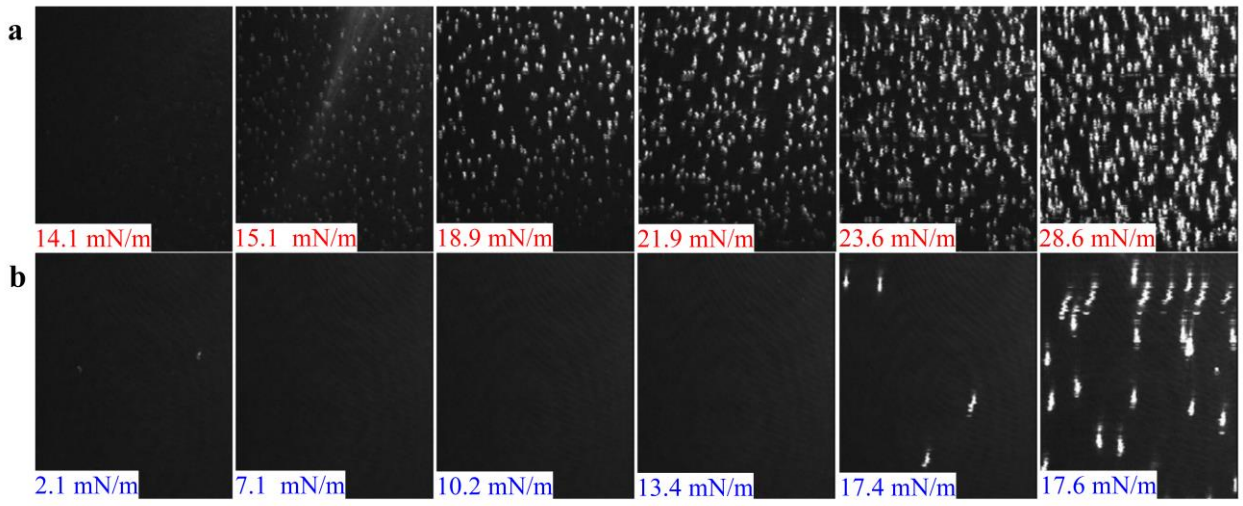

Figure 2.4. BAM images (220 μm × 275 μm) of monolayers at the air–aqueous interface of (a) α–tocopherol and (b) α–tocopherol acetate as a function of the surface pressure.

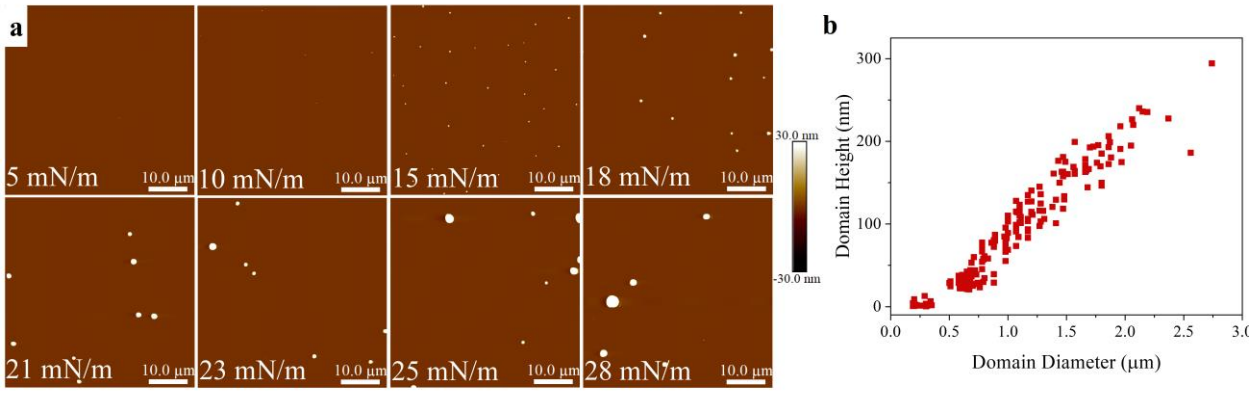

Figure 2.5. (a) AFM images of α–tocopherol at surface pressures of 5 mN/m, 10 mN/m, 15 mN/m, and 18 mN/m (top row) and 21 mN/m, 23 mN/m, 25 mN/m and 28 mN/m (bottom row). (b) Corresponding domain diameter and height showing the growth of the domains both in width and height as the surface pressure increases.

In contrast to α–tocopherol (Figure 2.2a), the isotherm α–tocopherol acetate shows a sharp collapse at 17.5 mN/m (Figure 2.2b) which correlates with the immediate formation of fewer, but larger, very bright protrusions from the monolayer film (Figure 2.4b). The sharp collapse makes Langmuir–Blodget transfer at constant pressure difficult and AFM images of such films transferred at both 10 mN/m and 17.5 mN/m exhibit a flat, uniform and featureless surface with no visible protrusions (data not shown). The difference in collapse is related to the kinetics of the growth of the protrusions, for which the altered molecular orientation (due to the replacement of a hydroxyl by an acetate) and consequent film compressibility modulus (as discussed earlier) play a determining role.

The BAM images of the DPPC:POPG (7:3) monolayer show the appearance of classical condensed phase domains at around 18 mN/m that persist to high pressures (Figures 2.6 and 2.7). These domains are attributed to a DPPC-rich condensed phase surrounded by a POPG-rich fluid phase. At higher pressures, there is a loss in optical contrast, which will be discussed later. Little change in the film morphology is observed with the addition of 1 mol % and 5 mol % of α–tocopherol or α–tocopherol acetate to the DPPC:POPG (7:3) mixture. At best, there is a minor variation in the domain sizes since some domains appear to be slightly larger at equivalent surface pressures. This may be explained by subtle changes in the line tension of the DPPC-rich condensed domains,

where higher line tensions drive the formation of larger domains, and lower line tensions drive the formation of smaller domains.[115] Both a loss in optical (phase) contrast and the reduction of the total condensed-phase areas occurs at lower surface pressures with greater concentrations of the additives, specifically above 10 mol % for α–tocopherol and 5% mol for α–tocopherol acetate, suggesting a fluidization of the monolayer film. Additionally, the bright protrusions formed by the tocopherols are eliminated in the mixed films, in agreement with the isotherm that shows no indication of an independent collapse of the tocopherol phase.

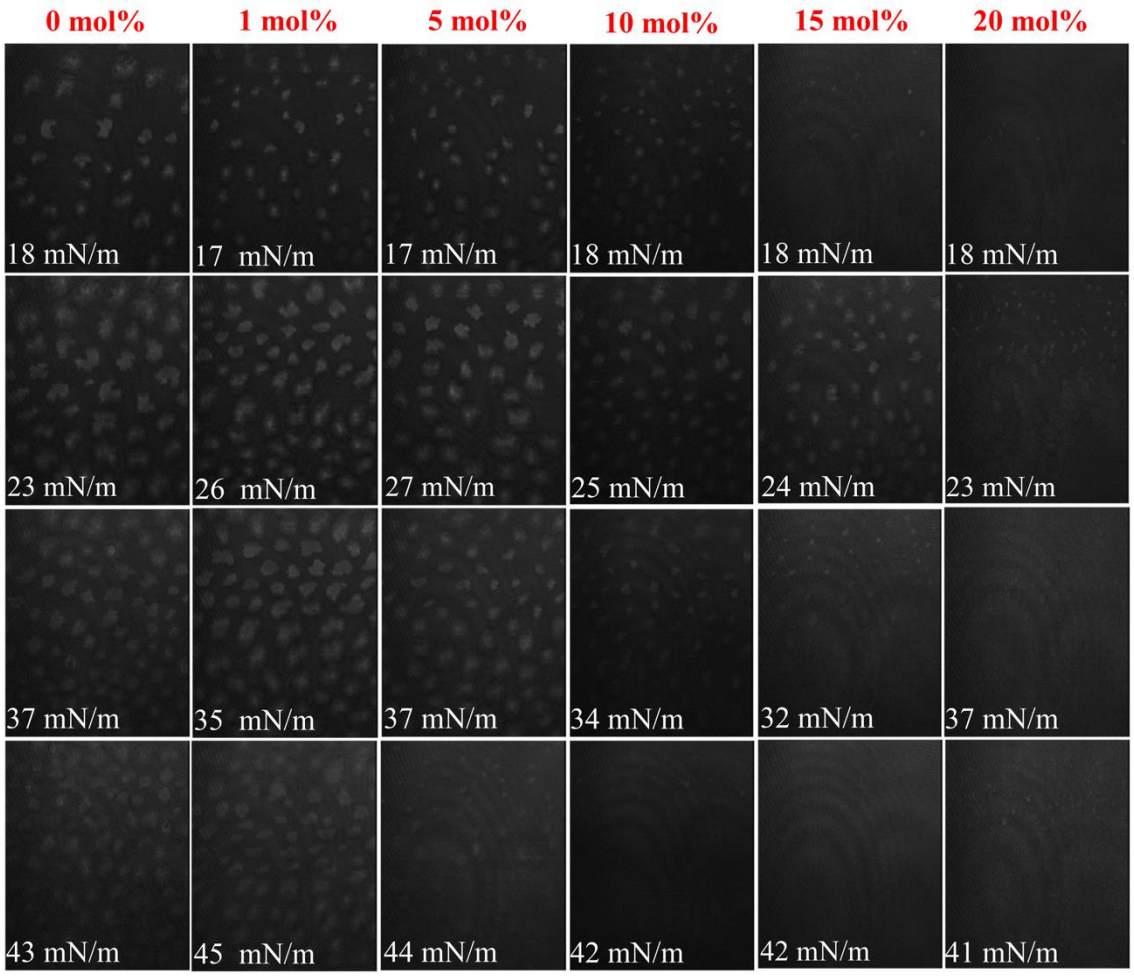

Figure 2.6. BAM images (220 μm × 275 μm) of DPPC:POPG (7:3) as a function of the surface pressure (from top to bottom): ~18 mN/m, ~25 mN/m, ~35 mN/m, and ~45 mN/m, and with varying molar concentrations of added α–tocopherol added (from left to right): 0 mol %, 1 mol %, 5 mol %, 10 mol %, 15 mol % and 20 mol %.

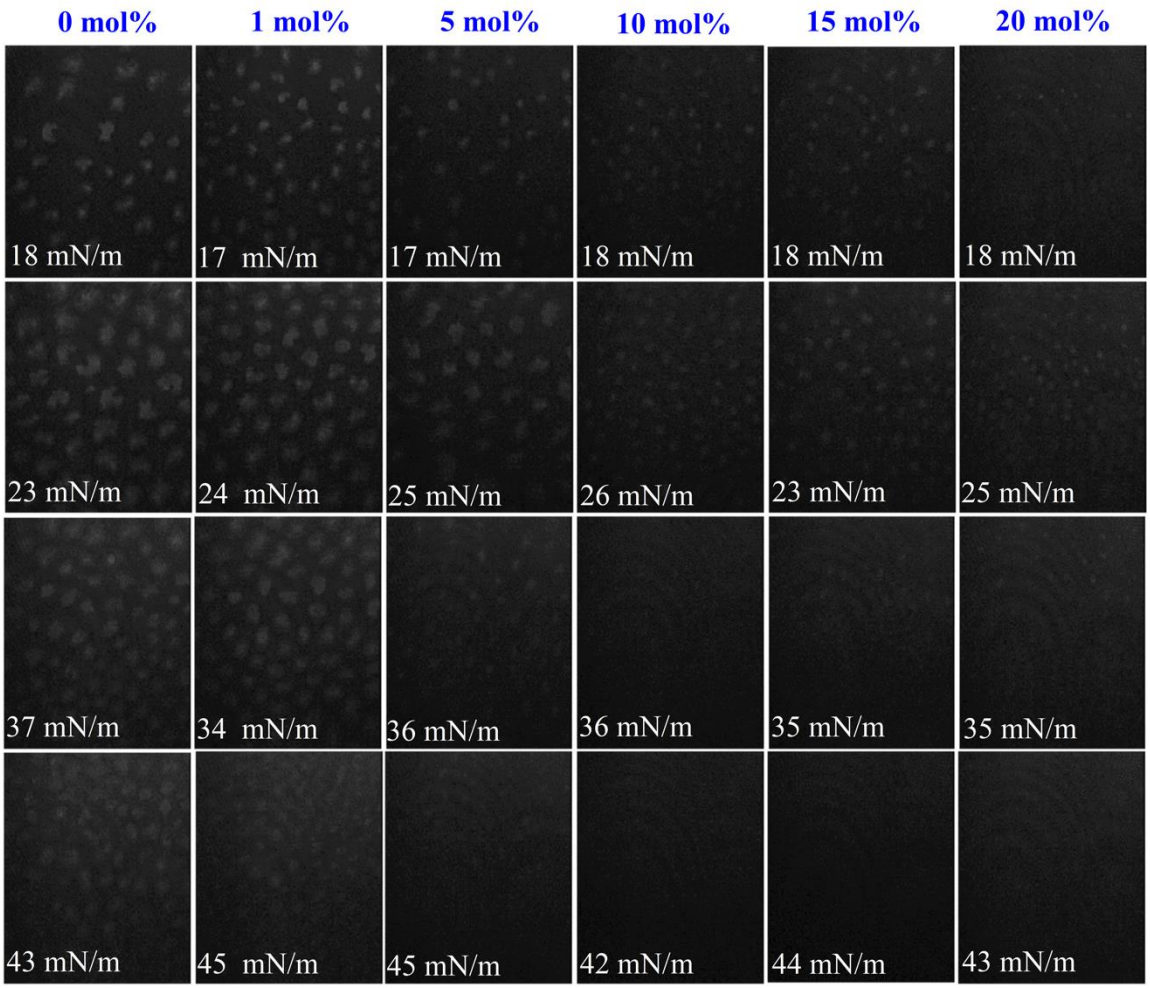

Figure 2.7. BAM images (220 μm × 275 μm) of DPPC:POPG (7:3) as a function of the surface pressure (from top to bottom): ~18 mN/m, ~25 mN/m, ~35 mN/m, and ~45 mN/m, and with varying molar concentrations of added α–tocopherol acetate added (from left to right): 0 mol %, 1 mol %, 5 mol %, 10 mol %, 15 mol % and 20 mol %.

The reduction in contrast observed at higher compression states has previously been attributed to either the collapse of the fluid phase[10] or to the formation of nanoscale domains below the optical resolution of BAM.[116] To determine if the loss of contrast is attributable to fluidization or one of the aforementioned factors, DPPC:POPG:α–tocopherol films were transferred onto mica for AFM analysis (Figure 2.8). An analysis of the surface area occupied by the condensed-phase domains reveals a 35% area coverage of the condensed phase in the absence of α–tocopherol that is reduced

to 4% with 20 mol % of α–tocopherol, indicative of fluidization. A distinct step change in the condensed phase coverage occurs for proportions of α–tocopherol greater than 10 mol %. Additionally, by 20 mol % α–tocopherol most of the domain diameters are between 0.5 μm to 1.5 μm, and thus below the lateral resolution of BAM, contributing to the loss of optical contrast. Muddana *et al.* showed that α–tocopherol exhibited lineactant properties such that it favored the phase boundaries in DPPC:DUPC (1:1) bilayers.[103] Lineactants reduce the line tension, lowering the energetic cost of forming phase boundaries and resulting in smaller domains.

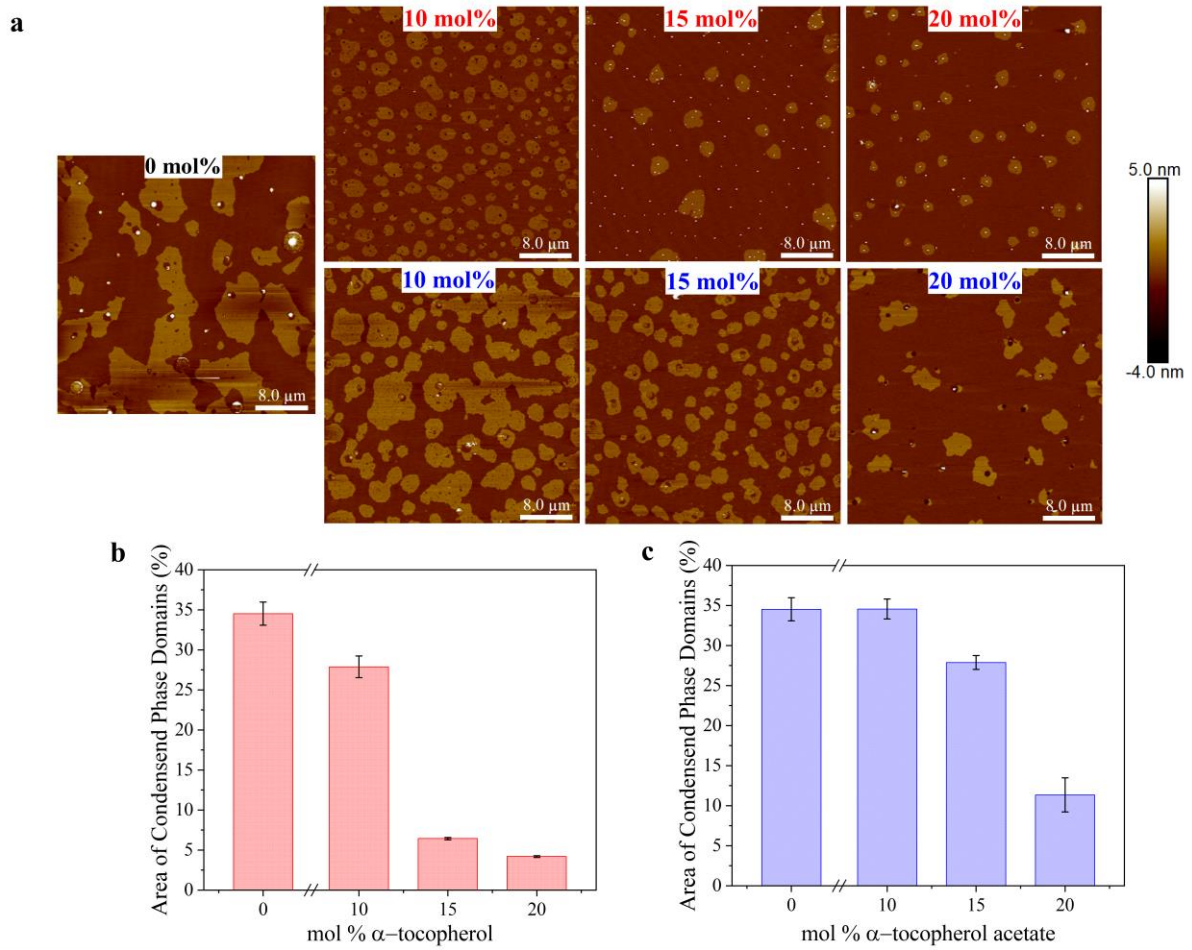

Figure 2.8. (a) AFM images of monolayer films transferred onto mica at 45 mN/m for DPPC:POPG (7:3) (black, 0 mol %) and varying molar concentrations (10 mol %, 15 mol % and 20 mol %) of added α–tocopherol (red, top) and α–tocopherol acetate (blue, bottom). Corresponding % area coverage of condensed phase domains for DPPC:POPG (7:3) monolayer films with different molar concentrations of added (b) α–tocopherol or (c) α–tocopherol acetate.

With both phases present, the tocopherols likely partition between the two phases and generate competing effects in terms of the mean molecular area. The expansion observed by Van Bavel *et al.* may be related to the higher proportion (80%) DPPC in their model membrane.[52] The previously reported preferential partitioning of the α–tocopherol's into the fluid phase may drive the apparent fluidization. To understand the mixing effects on each of the individual phases, isotherms for 1:1 POPG:α–tocopherol (representing if all the tocopherol partitions to the fluid phase) and 3:1 DPPC:α–tocopherol (representing if all the tocopherol partitions to the condensed phase) were investigated (Figure A3) and the excess areas tabulated in Table A1. POPG:α–tocopherol yields excess areas of –1 $Å^2$/molecule at 1 mN/m and –2 $Å^2$/molecule at 10 mN/m while DPPC:α–tocopherol exhibits excess areas of -7 $Å^2$/molecule at 1 mN/m and +8 $Å^2$/molecule at 10 mN/m, respectively. This is in agreement with partial molar volume measurements that show a larger tocopherol partial molar volume in a DPPC fluid phase (above its T_m) than in a POPC fluid phase at the same temperature.[85] Notably, where each lipid forms a liquid-expanded phase, we have contraction of the film (all pressures for POPG, low pressures for DPPC). This contraction is significantly greater for the saturated and zwitterionic DPPC lipids. Once the lipid film adopts a condensed phase (the plateau for DPPC is between 6 and 10 mN/m), there is a shift to a film expansion. This can either be due to an expansion of the condensed phase or the prevention of this condensed phase from forming, wherein the DPPC molecules remain in a liquid-expanded phase to higher surface pressures. Although the values obtained would suggest the tocopherols predominantly associate with the fluid phase, GIXD and XR were used to determine whether the tocopherols are miscible to any extent with the DPPC condensed phase (see below).

With increasing proportions of both additives, a fluidization of the condensed phase is observed at surface pressures above 18 mN/m. It is important to emphasize that the excess area calculations were restricted to surface pressures of up to 15 mN/m due to the low collapse pressures of α–tocopherol and α–tocopherol acetate. The BAM measurements were taken at surface pressures higher than 15 mN/m, rendering it impossible to accurately determine the precise impacts at these higher surface pressures. However, analogous to cholesterol, α–tocopherol contains major structural components such as a rigid ring structure with a polar hydroxyl group at one end and a hydrophobic chain at the other end. The difference is that the chromanol group on α–tocopherol is smaller than the steroid moiety on cholesterol, and the phytyl side chain (13 carbons) on

α–tocopherol is longer than the branched chain (5 carbons) on the sterol.[102] The addition of 1 mol % to 30 mol % cholesterol to model surfactant monolayers comprising 8:2 DPPC:DPPG (1,2-dipalmitoyl-sn-glycero-3-phosphoglycerol) leads to the formation of smaller circular domains and decreased condensed-phase area.[117] Cholesterol induces a contraction in molecular area when mixed with saturated lipids like DPPC and a slight expansion when mixed with more unsaturated lipids like DOPC and POPC.[101] By analogy, α–tocopherol, like cholesterol, may have a larger impact on the condensed phase than the fluid phase.

2.4.4. Film Structure

The GIXD contour plots obtained for DPPC:POPG (7:3) and their mixtures with α–tocopherol (molar concentrations of 10 mol %, 15 mol %, and 20 mol %) are shown in Figure 2.9. GIXD was performed at surface pressures of 10 mN/m (where DPPC:POPG (7:3) is in a liquid-expanded phase), 18 mN/m (where DPPC-rich condensed phase domains are first evident in BAM), 35 mN/m and 45 mN/m (just below and above, respectively, the collapse/expulsion of the POPG-rich phase). At all pressures between 18 mN/m and 45 mN/m, the diffraction patterns of DPPC:POPG (7:3) show three low-order reflections (10, 01, $1\bar{\bar{1}}$) with Bragg rod maxima above the horizon (Q_z) that correspond to an oblique lattice with tilted chains.[9] Note that GIXD peaks represent only the structure of the condensed phase domains since fluid or liquid-expanded phases yield no diffraction. The condensed phase is attributed to a DPPC-rich phase given its similarity to the diffraction pattern of DPPC itself[118] and the fact that POPG forms a liquid-expanded phase under these conditions. The peak positions and unit cell parameters calculated from fits of the three Bragg peaks and Bragg rods are provided in Tables A2 and A3. The DPPC-rich phase in the absence of α–tocopherol yields tilt angles of 31°, 28° and 20° for pressures of 18 mN/m, 35 mN/m and 45 mN/m, respectively. The large chain tilt angle of the DPPC-rich phase is comparable to the values reported in the literature[118] at similar surface pressures and is attributed to the area mismatch of the large DPPC headgroup and the two alkyl chains.[119] By tilting the chains, a balance between the projected area of the chains and that of the phosphatidylcholine head group is achieved.[119]

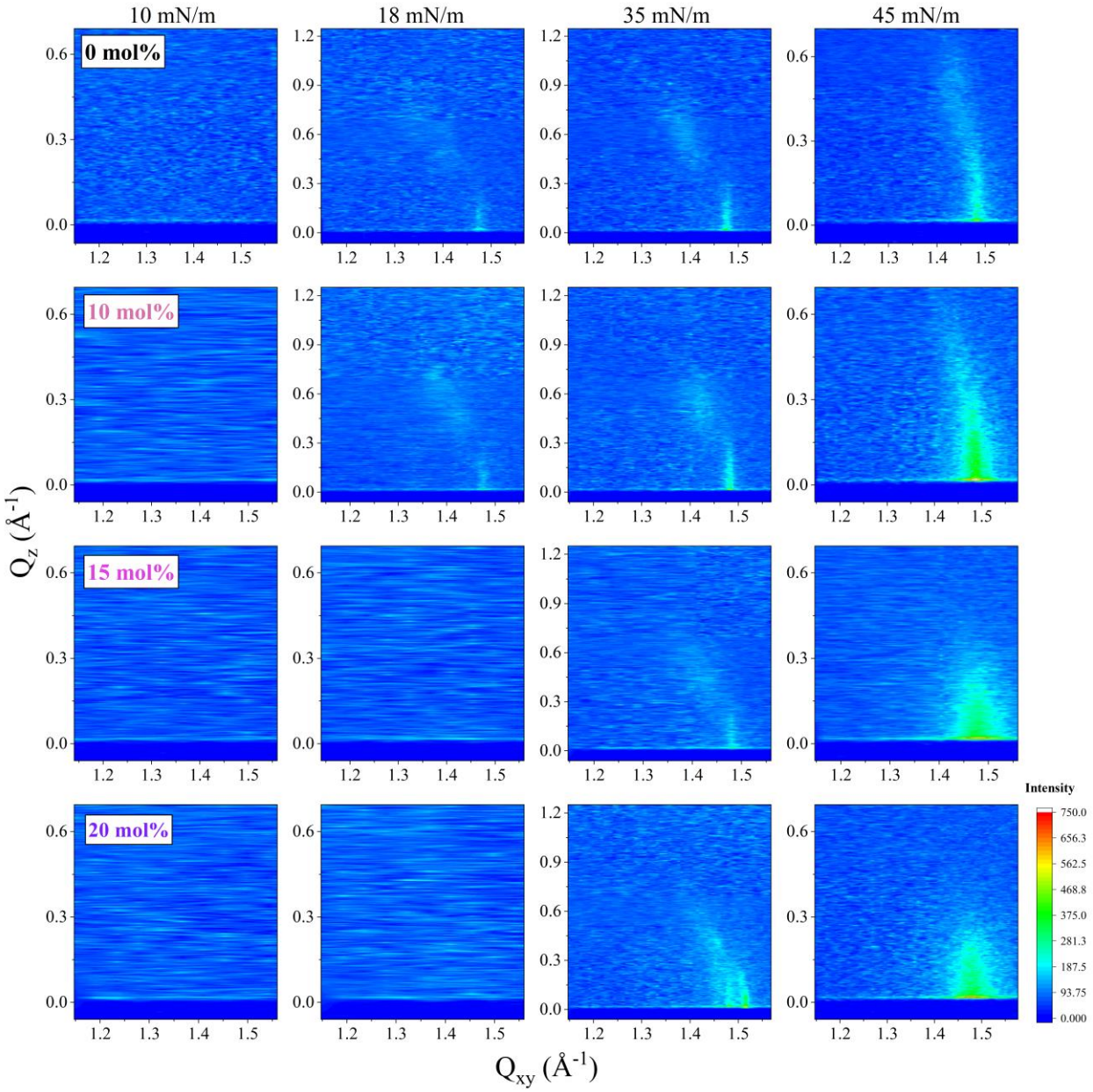

Figure 2.9. Contour plots of the X–ray intensities as a function of the in-plane (Q_{xy}) and out-of-plane (Q_z) scattering vector components for DPPC:POPG (7:3) with varying molar concentrations of α–tocopherol (top to bottom): 0 mol %, 10 mol %, 15 mol %, and 20 mol % at surface pressures (right to left) of 10 mN/m, 18 mN/m, 35 mN/m and 45 mN/m (note that not all Q_z scales are the same).

The diffraction peaks for the mixtures containing 10 mol %, 15 mol % and 20 mol % of α–tocopherol at 35 mN/m confirm the presence of DPPC-rich condensed phase domains within a fluid POPG phase. The lack of diffraction peaks at 18 mN/m for 15 mol % and 20 mol % indicate

the α–tocopherol hinders the formation of the condensed phase, pushing its formation to higher surface pressures. With increasing molar concentrations of α–tocopherol, the out-of-plane peaks move to lower Q_z and higher Q_{xy} values (Table A2), indicative of a tilt angle decrease from 28° (with no α–tocopherol) to 19° at 35 mN/m (with 20 mol % added α–tocopherol) (Table A3), evidence that α–tocopherol intercalates in the DPPC chain region and mimics the behavior of low amounts of cholesterol in PC membranes.[120] By 45 mN/m, the diffraction peaks for systems with α–tocopherol shift to much lower Q_z values, corresponding to very low tilt angles. Like cholesterol, we suggest α–tocopherol alleviates the area mismatch of the large DPPC headgroups by incorporating itself between the DPPC chains.[119,120] Thus, we propose that some of the α–tocopherol intercalates within the condensed DPPC phase, leading to a notable reduction in the tilt angle.

For DPPC:POPG (7:3) with 20 mol % α–tocopherol at 35 mN/m, additional peaks are observed at higher Q_z (Figure 2.9). Repetition of the measurement yielded diffraction peaks associated with the same DPPC-rich phase peaks but not the additional peaks at higher (>1.5 $Å^{-1}$) Q_{xy} (Figure A4). We attribute these high Q_{xy} peaks to a kinetic effect, wherein as the POPG begins to collapse, the α–tocopherol redistributes between the phases (the partitioning of α–tocopherol between the remaining LE and the condensed phase changes). Depending on the extent of loss of POPG and the kinetics of the molecular redistribution, an intermediate phase can form. By 45 mN/m the film has had more time to equilibrate, and these higher Q_{xy} peaks are less distinct. A future study will investigate the partitioning of the α–tocopherol between these phases in more depth.

GIXD measurements on the DPPC:POPG:α–tocopherol acetate mixture were performed for only 20 mol % additive at surface pressures of 20 mN/m, 35 mN/, and 45 mN/m and are shown in Figure A5. The fits and unit cell parameters are tabulated in Tables A2 and A3, respectively. Unlike the 20 mol % α–tocopherol system, by 20 mN/m, diffraction peaks from the emerging DPPC-rich condensed phase are observed. At 35 and 45 mN/m, the diffraction patterns from the DPPC-rich phase are weaker and with lower signal-to-noise, which may indicate that the acetate analogue of α–tocopherol induces a greater degree of fluidization (i.e., less condensed phase in the beam footprint). At 35 mN/m, the chain tilt angle for the 20 mol % α–tocopherol acetate mixture is approximately 12° (Table A3), considerably lower than DPPC:POPG (7:3) without any

additives (28°) and considerably lower than the film analogue with 20 mol % α–tocopherol (19°). The addition of a simple acetate group to the α–tocopherol headgroup does not hinder its incorporation into the DPPC lattice and yields a significantly reduced alkyl chain tilt angle.

X–ray reflectivity data was fit with the top slab representing the alkyl chains (tail) and a lower slab representing the headgroups to generate a vertical electron density profile (Figure 2.10). Fitting outputs are summarized in Table A4.

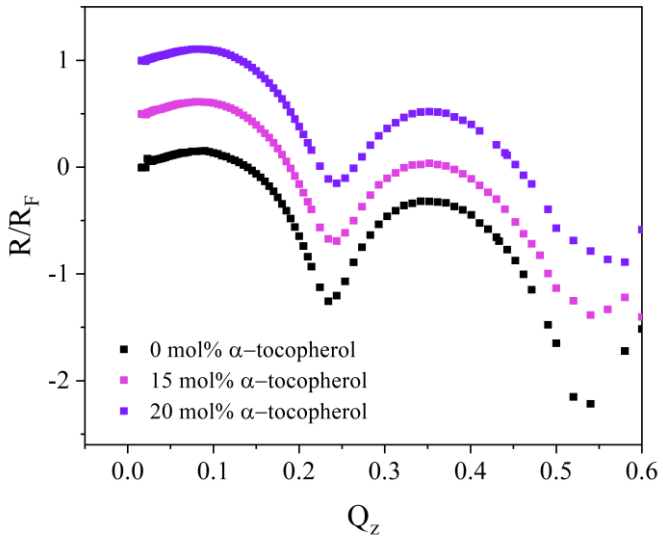

Figure 2.10. Normalized X–ray reflectivity versus the vertical scattering vector component Q_z of DPPC:POPG (7:3) in the absence and presence of 15 mol % α–tocopherol and 20 mol % α–tocopherol at a surface pressure of 35 mN/m.

The presence of 15 mol % or 20 mol % α–tocopherol in the DPPC:POPG (7:3) monolayer yields a smaller average alkyl chain thickness (15.1 Å) compared to that of DPPC:POPG (7:3) (17.6 Å). The film thickness represents the weighted average of both the liquid-expanded and condensed phases. The decrease in alkyl chain thickness is most likely due to the increased proportion of the thinner liquid-expanded phase. The XR fits also indicate a larger average headgroup thickness with added α–tocopherol (7.8 Å) compared to that of DPPC:POPG (7:3) with no α–tocopherol (6.9 Å). Figure 2.11 depicts the aromatic moiety of α–tocopherol anchored to the subphase. The remainder of the chromanol ring is positioned above the phosphocholine headgroup of DPPC which may

explain the increase in headgroup thickness. This arrangement was previously observed by resonance energy transfer studies, with bilayers composed of 20 mol % α–tocopherol and DPPC.[121] Furthermore, the addition of 20 mol % of α–tocopherol in DPPC:POPG (7:3) leads to an increase in electron density at the tail region while causing a reduction in electron density at the headgroup region. The α–tocopherol molecules within the DPPC-rich condensed phase contribute to an expansion of the intermolecular space between the DPPC headgroups, decreasing the overall headgroup electron density. The electron enrichment at the tail region can be the result of the incorporation of the branched phytyl chain of the α–tocopherol within the alkyl chain region.

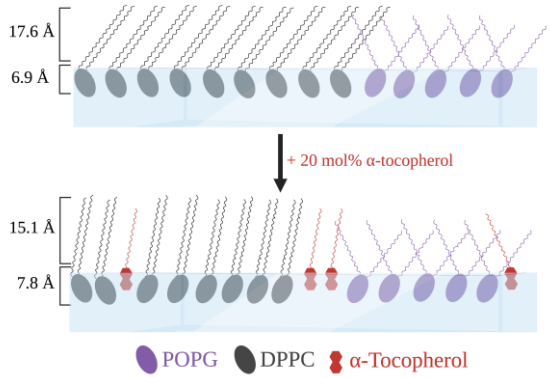

Figure 2.11. Schematic representation of α–tocopherol partitioning between the liquid-expanded and condensed phases.

2.4.5 Implication of the Findings for EVALI

α–Tocopherol acetate has been found in significant proportions in the bronchoalveolar lavage (BAL) samples from EVALI patients.[41] The persistence of α–tocopherol acetate in BAL fluids indicates its retention in the alveoli. Given the lipophilic structure of α–tocopherol acetate, as well as its physical and chemical similarity to phospholipids, it is highly likely to embed in the pulmonary surfactant coating the alveoli, the first line of defense to inhaled species. Our findings using model membranes, that show that α–tocopherol and α–tocopherol acetate are present in both the fluid and condensed phases of the pulmonary surfactant, are consistent with this retention in the alveoli and BAL fluids. EVALI patients presented clinical pathologies including ground-glass opacities[122,123] and foamy microphages[46], as observed with exogenous lipid pneumonia. Thus, it has been suggested that EVALI represents a form of airway-centered chemical pneumonitis.[43,46]

The increase in foamy macrophages is associated with impaired recycling of the pulmonary surfactant.[124] The pulmonary surfactant membrane composition is tightly regulated. Changes in its composition, in this case through the deposition of fatty materials (α–tocopherol and α–tocopherol acetate) and resulting impaired pulmonary surfactant recycling, are expected to cause difficulty in gas-exchange and breathing (due to changes in surface tension and the work of breathing).[125] The latter can contribute to a shortness of breath and the former to reduced oxygen levels, both commonly reported symptoms for EVALI.[122]

2.5. Conclusion

Herein we have compared the phase behavior and the interactions of α–tocopherol and α–tocopherol acetate with the different phases of lung surfactant model membranes. While qualitatively similar surface pressure–area isotherms and film morphologies are obtained, there are notable differences produced by replacing the hydroxyl in the headgroup with acetate. α–Tocopherol exhibits a higher compressibility than α–tocopherol acetate and an altered kinetics of the film collapse, with α–tocopherol exhibiting a broader collapse over a range of surface pressures that correlates with the slow growth (laterally and vertically) of protrusions comprising the expelled lipid material. By contrast, the collapse from the liquid-expanded phase of α–tocopherol acetate is very sharp and yields fewer, but larger, lipid protrusions.

The interaction of either α–tocopherol and α–tocopherol acetate with the model membrane lipids induces the tocopherols to stay in the plane of the membrane to much higher surface pressures, inhibiting the formation of the tocopherol-rich protrusions. Both tocopherols partition between the DPPC-rich condensed and POPG-rich LE phases. α–Tocopherol appears to take up some of the excess space within a liquid-expanded phase (negative excess areas for POPG at all pressures and DPPC at 1 mN/m and 5 mN/m) without inducing a condensed phase. The positive excess areas for DPPC:α–tocopherol mixtures at 10 mN/m and 15 mN/m combined with changes in the GIXD peak positions for the DPPC:POPG mixtures with either additive confirm that some α–tocopherol and α–tocopherol acetate clearly partitions to the DPPC-rich condensed phase. The reduction in the alkyl chain tilt angle of the condensed phase indicates that the film expansion is not due to an expansion of the condensed phase. Notably, higher concentrations of α–tocopherol acetate,

compared to α–tocopherol, are required to see extensive fluidization of the film. This may be because the altered molecular orientation of α–tocopherol acetate enables better incorporation into the DPPC-rich phase, evidenced by the reduced fluidization and significantly lowered tilt angles. The biophysical properties and functionality of the pulmonary surfactant membrane are finely tuned to its composition and phase structure.[108] Both α–tocopherol and α–tocopherol acetate lead to a net fluidization of the model membranes by inhibiting the formation of condensed phase, thus increasing the proportion of liquid-expanded phase, despite having a contracting effect on each individual phase. This fluidization greatly diminishes the proportion of condensed phase, whose role is to ensure the film stability at ultralow surface tension and high compression states (i.e., upon exhalation). This fluidization, along with the altered collapse pressure, becomes most evident at α–tocopherol proportions greater than 10 mol % and α–tocopherol acetate proportions greater than 15 mol %. Dosimetry analysis has predicted that 42% of α–tocopherol acetate inhaled from e-liquids can deposit in the pulmonary rather than tracheal region.[126] The residence time and accumulation of tocopherols as a function of vaping frequency in the pulmonary surfactant is not known, although tocopherol acetate was sufficiently present to be detectable in BAL fluids from patients with EVALI. Although studied herein in terms of their impact on model lung surfactant membranes, given α–tocopherol is a naturally occurring, membrane-soluble antioxidant, and α–tocopherol acetate is used not only as a vaping solution diluent but also as a pro-drug precursor, the fluidizing effects of these compounds have broader implications.

Chapter 3. Understanding the Mixing Behavior of α–Tocopherol with Common Membrane Lipids (Phosphotidylcholine & Phosphotidylglycerol)

3.1. Abstract

Vitamin E, particularly α–tocopherol, is a potent antioxidant important for cellular health. As the most bioavailable form of vitamin E, α–tocopherol integrates into many cellular membranes, preventing lipid peroxidation of unsaturated phospholipids by neutralizing free radicals. This antioxidant capacity plays a role in preventing mitochondrial diseases and immune system deterioration. This study focuses on the interactions of binary mixtures of α–tocopherol with DPPC (1,2-dipalmitoyl-sn-glycero-3-phosphocholine) and POPG (1-palmitoyl-2-oleoyl-sn-glycero-3-phosphoglycerol) for lipid:α–tocopherol ratios of 3:1, 1:1, and 1:3. The properties of surface activity, and morphology of the films were evaluated at a microscopic and nanoscopic level by surface pressure-area isotherms, excess area calculations, Brewster angle microscopy (BAM), and atomic force microscopy (AFM). To study the structural changes of the films at a molecular level, grazing incidence X–ray diffraction (GIXD), and X–ray reflectivity (XR) were employed. α–Tocopherol shows a high degree of miscibility with POPG even at the highest concentration studied of 75 mol %. We demonstrate that α–tocopherol does not completely fluidize DPPC at 25 mol % as was previously reported. Moreover, α–tocopherol exhibits some miscibility in the DPPC-rich condensed phase, altering alkyl chain packing. The linactant behaviour of α–tocopherol was visualized using AFM which shows clustering at the domain boundaries. These findings indicate that α–tocopherol specifically interacts with and modulates the properties of both saturated and unsaturated membranes differently, contributing to its diverse roles.

3.2. Introduction

Vitamin E is one of nature's most potent membrane-soluble antioxidant molecules that is primarily ingested through our diet. Among the eight forms of Vitamin E, α–tocopherol stands out as the least metabolized and most bioavailable.[127,128] A key reason for this is the presence of the hepatic α–tocopherol transfer protein in the liver which preferentially binds to α–tocopherol and secretes

it from our liver into the plasma. α–Tocopherol is distributed across various cellular components and abundant in phospholipid cell membranes including the plasma membrane[129,130], mitochondrial membrane[131–134], endoplasmic reticulum[135], and lysosomal membrane[136–138]. It has been greatly studied for its diverse role in cellular signaling[139–141], beneficial effect on female's fertility and reproductive health[142,143], immune system strengthening and regulation[144–149], anti-inflammatation[144,150–152] and protection against oxidative damage and lipid peroxidation of membrane lipids[132,153–155].

The major antioxidant ability of α–tocopherol stems from its capacity to limit active lipid peroxidation of membranes enriched in unsaturated phospholipids by neutralizing free radicals.[68,156] One significant mechanism is its reaction with radical species, either by, intercepting free radicals diffusing into the membrane and/or terminating lipid peroxyl radicals, which occurs almost 1,000 times faster with α–tocopherol compared to polyunsaturated lipids.[154] Deficiencies in vitamin E, specifically α–tocopherol, have shown to lead to mitochondrial diseases and weakening of the immune system, amongst other effects.

Membranes comprise of a complex mixture of lipids, both saturated and unsaturated, among other components. Given α–tocopherol's ability to prevent the unwanted oxidation of unsaturated lipids, numerous studies have investigated its mechanism of protection. A significant focus has been on determining the specific location of α–tocopherol within membranes. α–Tocopherol exhibits linactant properties, a concept first proposed by Muddana et al.[103] Their research on 1:1 DPPC:DUPC bilayers demonstrated that α–tocopherol predominantly resides at the phase boundaries between the two lipid phases.[103]

Recent studies have linked vaping lung injuries to additives such as vitamin E acetate (α–tocopherol acetate) and flavoring molecules.[51,157–161] For tocopherols this has been linked to its linactant behavior which modifies the line tension of the lung surfactant and compromises its proper function.[51,157,158] Additionally, α–tocopherol has been shown to protect cells against 7-ketocholesterol-induced apoptosis[162,163] and is the strongest vitamer for inhibiting phospholipase A_2[164], an enzyme involved in the inflammatory response. This inhibition was later partly attributed to α–tocopherol's linactant properties, which increase the miscibility of existing phases at the boundaries and promote the dissolution of 7-ketocholesterol-containing rafts[103], thereby inactivating their signaling pathways.[165] Furthermore the stabilization of membrane edges by α–tocopherol makes it more difficult for phospholipase A_2 to access the lipid membrane.[164,165]

Previous work has focused on the interaction of α–tocopherol with phosphocholines, with an emphasis on understanding how the degree of chain unsaturation affects its miscibility within the lipid membrane and its vertical placement of its reactive hydroxyl moiety, and how these translate to its role as a membrane-soluble antioxidant.[86,89] Phosphocholines are highly abundant in mammalian cell membranes, and for the lung surfactant membrane, dipalmitoylphosphatidylcholine (DPPC) is the primary phosphocholine. DPPC is a saturated zwitterionic lipid, and commonly used in model membranes for its role in membrane stability and fluidity. Phosphoglycerols, namely 1-palmitoyl-2-oleoyl-phosphatidylglycerol (POPG), is most abundant in human lung surfactant and bacterial membranes[166,167]. POPG is anionic and induces membrane curvature, typically displaying a positive curvature.[168] It enhances membrane dynamics by improving permeability due to its loose packing structure[168] and, influences the structure and conformation of membrane proteins[167,169], playing a role in various cellular processes. While most research has focused on α–tocopherol's role in protecting eukaryotic cells from oxidative damage, its role in protecting bacterial cell membranes, both commensal and pathogenic, is much less clear. However, recent research has explored α–tocopherol in conjunction with probiotics to enhance their survival and efficacy[170] and positive effect on the bacterial gut microbiome that may delay age-related diseases.[171]

We previously observed that α–tocopherol partitions to both the fluid and condensed phase of the model lung surfactant. This prompted us to conduct a more in-depth study of α–tocopherol's mixing behaviour with the individual components of the model lung surfactant, DPPC and POPG, that are also common membrane lipids. By understanding how α–tocopherol interacts with these lipids, we can deepen our knowledge of its antioxidant role, its contribution to membrane stabilization, its effects on the immune system and gut health as well as its linactant properties, which has recently been highlighted as a factor contributing to many of the beneficial actions of α–tocopherol.

3.3. Experimental (Materials & Methods)

Materials. 1,2-dipalmitoyl-sn-glycero-3-phosphatidylcholine (DPPC, 99%) and 1-palmitoyl-2-oleoyl-phosphatidylglycerol (POPG, 99%) were purchased from Avanti Polar Lipids in powder form. α–Tocopherol (96%), tris(hydroxymethyl)aminomethane (Tris, 99.8%) and NaCl (99%)

were purchased from Sigma-Aldrich. ACS grade chloroform (Fischer Scientific) was used to prepare the phospholipid and additive stock spreading solutions. All reagents were used without further purification. The molecular structures of the phospholipids and α–tocopherol are shown in Figure 3.1.

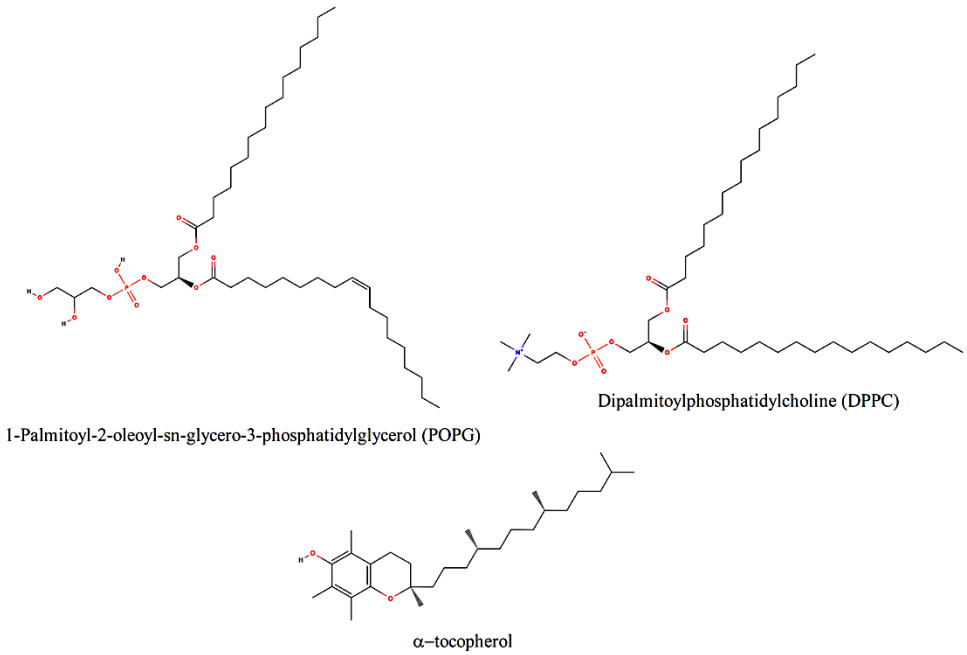

Figure 3.1. Molecular structures of DPPC, POPG and α–tocopherol.

Lipid Mixtures and Aqueous Subphases. Stock solutions of α–tocopherol (1.0 mM) in chloroform were combined with stock solutions of DPPC (1 mM) and POPG (1 mM) in chloroform to prepare binary solutions containing 25 mol %, 50 mol %, and 75 mol % of α–tocopherol and 75 mol %, 50 mol %, and 25 mol % DPPC or POPG, respectively. Tris-buffered saline (TBS) comprising 50 mM Tris and 150 mM NaCl served as the aqueous subphase for all Langmuir monolayer experiments and was prepared with ultrapure water (resistivity of 18.2 MΩ cm), and pH adjusted to 7.4 using hydrochloric acid.

Surface Pressure–Molecular Area Isotherms. Surface pressure–molecular area isotherms were obtained using a Langmuir film balance (Model 516, Nima Technology) with maximum trough

surface area of 80 cm^2 and a filter paper Wilhelmy plate (Whatman No. 3001-604). Neat α–tocopherol, DPPC, POPG, and their binary mixtures were spread on the TBS subphase and the solvent was allowed to evaporate (10 min) prior to lateral symmetric compression of the film at the air-aqueous interface at a rate of 5 cm^2/min. All experiments were conducted at room temperature (22.5 ± 0.5 °C) and at least three separate isotherms were obtained for each lipid composition to ensure reproducibility. Previous reports[108] have shown that the phase behavior of the model membranes at room temperature to be qualitatively similar to those at physiological temperatures, albeit with the phase transitions shifted to lower surface pressures.

The impact of lipid composition on molecular mixing was assessed from changes to the average molecular area. The ideal mixing molecular area at a given pressure is calculated from the weighted average of the measured molecular areas of the DPPC or POPG and neat α–tocopherol.

Brewster Angle Microscopy (BAM) Imaging. BAM imaging of monolayers at the air-aqueous interface during barrier compression was performed using an I-Elli2000 imaging ellipsometer (Nanofilm Technologies) coupled to a Langmuir film balance (Model 601BAM, Nima Technology) with a maximum trough area of 146 cm^2. The instrument is equipped with a 50 mW Nd:YAG laser (λ=532 nm), and the images were captured using a 20× objective (with a field of view of 220 μm × 275 μm and lateral resolution of approximately 1 μm) at the Brewster incident angle of 53.15°. Following a wait time of 10 min for solvent evaporation after spreading of the lipid solution, the monolayer was symmetrically compressed at a rate of 5 cm^2/min. All BAM images were obtained at 60% laser brightness intensity.

Langmuir monolayer transfer onto mica substrate. Monolayer films were vertically transferred on the upstroke from the air–aqueous interface onto freshly-cleaved mica using the Langmuir–Blodgett technique. The monolayer was compressed and held for five minutes at the target pressure prior to transfer at a rate of 5 mm/min. The solid-supported films were allowed to dry under ambient conditions for 30 min and imaged by AFM within 24 h of their preparation.

Atomic force microscopy (AFM). A MultiMode 8HR scanning probe microscope (Bruker Nano, Santa Barbara, CA) was used to capture AFM images in Peak Force Tapping Mode in air with silicon tips mounted on nitride levers of nominal spring constant of 0.4 N/m and resonance frequency of 70 kHz (Model Scanasyst-Air, Bruker AFM Probes). Images were recorded at a scan

rate of 0.759 Hz and 512 × 512-pixel resolution and processed with Nanoscope software version 2.0.

Grazing incidence X–ray diffraction (GIXD). The GIXD experiments were performed at the beamline 15-ID-C ChemMatCARS of the Advanced Photon Source (APS) at Argonne National Laboratory with the following parameters: X–ray beam wavelength of 1.239 Å, incidence angle of 0.0906°, horizontal size of 20 μm, and vertical size of 120 μm, leading to a beam footprint of 2 × 10^{-3} cm by 7.6 cm. The detector used was the 2D Swiss Light source PILATUS 100 K set to single-photon counting mode. Two sets of slits, one placed in front of the detector to control the beam footprint and the other placed 280 mm from the sample, were used to minimize intense low-angle scattering. Experiments were performed at the air–aqueous interface of a 340 cm^2 Langmuir trough with a compression rate of 5 cm^2/min. The measured GIXD data is plotted as contour plots of the intensity as a function of both the horizontal (Q_{xy}) and the vertical (Q_z) scattering vector components. The lattice spacing d_{hk} was obtained from the in-plane diffraction data as $d_{hk}= 2p/Q^{hk}_{xy}$, where the Miller indices h, k were used to index the Bragg peaks needed to calculate the unit cell parameters for the in-plane lattice. The full width at half maximum (fwhm) of the Bragg peaks after correction for the instrumental resolution (0.0084 $Å^{-1}$) was used to calculate the in-plane correlation length using the Scherrer formula. GIXD experiments were performed at lateral surface pressures of 18 mN/m, 35 mN/m and 45 mN/m at a temperature of 22.0 ± 0.5 °C.

X–ray reflectivity (XR). XR is measured as a function of the vertical scattering vector component (Q_z). XR probes the electron density variation ρ(z) of the vertical structure of the layers at the air-aqueous interface. The monolayer was modeled as a stack of slabs, with each slab having a constant thickness and electron density. The electron density profile ρ(z) was laterally averaged over both the ordered and disordered parts of the monolayer under the footprint of the X–ray beam.

The X–ray reflectivity data was analyzed using an open-source (Python) software developed and provided by Wei Bu, beamline scientist at ChemMatCARS. The measured X–ray reflectivity $R(Q_z)$ is normalized by the Fresnel reflectivity $R_F(Q_z)$, which is calculated for a sharp air-aqueous interface. The X–ray reflectivity was calculated using the Parratt method. Nonlinear least-squares fitting was used to determine the minimum number (N^{-1}) of internal slabs to best fit the X–ray reflectivity data. In our XR data analysis, all systems were treated as a homogeneous monolayer

film although lateral phase separation occurs under the experimental conditions. This assumption was made based on the sizes of the condensed and liquid-expanded phases, which are less than the footprint of the X–ray beam in all our systems. This assumption has been previously used in the literature, where the domain sizes of the phase-separated patches are smaller than the X–ray beam footprint.[109] All XR experiments were performed at a lateral surface pressure of 35 mN/m and at a temperature of 22.0 ± 0.5 °C.

3.4. Results & Discussion

3.4.1. Surface Pressure–Molecular Area Isotherms & Film Compressibility

The surface pressure–molecular area isotherms of DPPC, POPG, and binary mixtures of DPPC:α–tocopherol (3:1, 1:1, 1:3) and POPG:α–tocopherol (3:1, 1:1, 1:3) are shown in Figure 3.2a,b. The corresponding compressibility moduli for DPPC and POPG as well as binary mixtures with α–tocopherol are shown in Figure 3.2c,d.

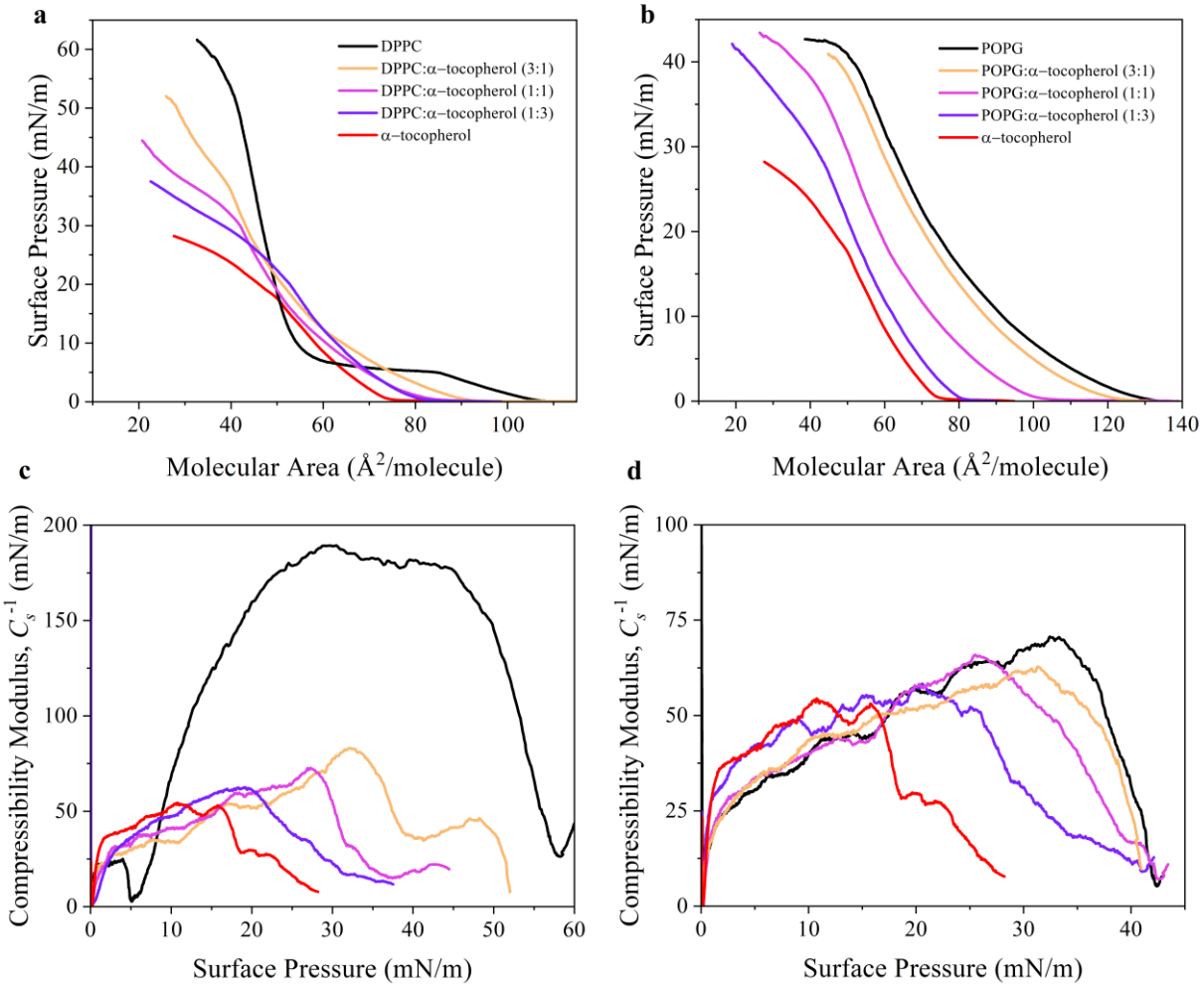

Figure 3.2. UPPER PANELS: Surface pressure–area isotherms for (a) neat α–tocopherol, DPPC and binary mixtures of DPPC:α–tocopherol (3:1, 1:1, 1:3), and (b) neat α–tocopherol, POPG and binary mixtures of POPG:α–tocopherol (3:1, 1:1, 1:3). LOWER PANELS: The compressibility moduli as a function of the surface pressure for (c) DPPC and binary mixtures of DPPC:α–tocopherol (3:1, 1:1, 1:3) and (d) POPG and binary mixtures of POPG:α–tocopherol (3:1, 1:1, 1:3). Color scheme indicated in legend.

With decreasing molecular area and increase in surface pressure DPPC exhibits the classical LE-LC phase transition at approximately 5-10 mN/m.[172] There is no obvious LE-LC phase transition in the isotherms of the binary mixtures of DPPC:α–tocopherol (3:1, 1:1, 1:3) (Figure 3.2a). The methyl-branched tail of α–tocopherol similarly disrupts the phosphocholine packing in dimyristoylphosphatidylcholine:α–tocopherol (3:1) bilayers, which showed the absence of the gel-to-LC phase transition.[173] The collapse pressure for α–tocopherol is ~ 17 mN/m, corresponding molecular area of ~ 50 Å^2/molecule while that of DPPC is at ~ 55 mN/m occurring at a molecular area of ~ 40 Å^2/molecule (Figure 3.2a and Table B1). For all proportions of α–tocopherol, a transition is observed at molecular areas in the range of ~ 42 to ~ 53 Å^2/molecule (Table B1). As the proportion of α–tocopherol increases, the initial area for the transition increases and the initial surface pressure of the transition decreases. Thus, as the proportion of α–tocopherol increases, the molecular area and pressure of this transition approach that of the collapse of α–tocopherol. If two components are fully miscible in a binary mixture only one phase transition or collapse must occur, and in contrast two independent collapses will occur if components of the monolayer are not fully miscible.[84] With lower proportions of α–tocopherol, there are clearly two distinct transitions in the isotherm. These two distinct phase transitions are more evident in the compressibility moduli shown in Figure 3.2c and the pressure at which both of these occur, varies with the proportion of α–tocopherol. Thus, we propose partial miscibility between DPPC and α–tocopherol at these proportions, wherein the lower pressure transition is associated with the collapse of an α–tocopherol-rich phase and the higher-pressure transition with the collapse of a DPPC-rich phase. The collapse of the DPPC-rich phase is lowered with the addition of 25 mol % α–tocopherol and while it is clear that a DPPC-rich phase is observed at higher proportions of α–tocopherol, we were unable to reach high enough surface pressures to attain collapse of this phase. By comparison, in our previous work that investigated the physicochemical impacts of vaping additives (α–tocopherol and α–tocopherol acetate) in model lung membranes, the tocopherols did not exhibit an independent collapse.[158]

The film compressibility modulus (C_s^{-1}) decreases from 200 mN/m (without α–tocopherol) to below 100 mN/m with all proportions of α–tocopherol added. An increase in monolayer film compressibility was also observed by Jurak *et al.*, attributed to a disruption of the DPPC packing by the tocopherol branched-chain.[84] The maximum C_s^{-1} remains low but shows a small decrease

from 80 mN/m to 63 mN/m as the proportion of α–tocopherol increases. Despite large decreases in compressibility moduli, a condensed phase persists at both low and high surface pressures for DPPC:α–tocopherol (3:1), and only at higher pressures for DPPC:α–tocopherol (1:1) (as will be shown with AFM imaging).

The collapse pressure of POPG is observed at ~ 42 mN/m, comparable to the literature[174,175], with a low compressibility modulus <75 C_s^{-1} (Table B1 and Figure 3.2b,d). All isotherms for POPG and α–tocopherol mixtures are shifted to lower molecular areas in comparison to POPG due to α–tocopherol occupying a much smaller molecular area than the double-chained POPG. Comparable shifts to lower molecular areas were observed by Jurak *et al.* for α–tocopherol in mixtures with phosphocholines with varying degrees of unsaturation.[84] POPG:α–tocopherol (3:1) has a similar collapse pressure ~ 42 mN/m as POPG (Table B1). A broad collapse that more closely resembles the shape of the α–tocopherol collapse is observed in POPG:α–tocopherol (1:1) and POPG:α–tocopherol (1:3) starting at ~38 mN/m, and ~28 mN/m, respectively, as also evidenced in the compressibility moduli (Figure 3.2d and Table B1). The broad collapse of POPG:α–tocopherol (1:1) reaches a slightly higher surface pressure than POPG. In our previous study using a 7:3 DPPC:POPG model lung surfactant membrane, the collapse of the POPG-rich liquid-expanded phase was shifted to higher surface pressures with the addition of 20 mol % α–tocopherol (note that the POPG and α–tocopherol were at a 1:1 molar ratio, if one were to assume that all of the α–tocopherol is in the POPG-rich phase).[158] The higher surface pressures attained suggests a synergistic effect between POPG and α–tocopherol on film stability. Other types of synergistic effects have been reported with α–tocopherol-lipid mixtures. For example, fatty fish species, such as freshwater sardines, have skin lipids comprising over 50% unsaturated lipids and approximately 13% polyunsaturated lipids, making them susceptible to oxidation.[176,177] Sardine skin lipid extracts were shown to exhibit the highest oxidative stability with α–tocopherol combined with other antioxidants.[177] Other examples of the synergy between tocopherols and unsaturated lipids was reported in food supplements given to fish, where polyunsaturated lipids and α–tocopherol given together exhibited a synergistic effect on the immune response and disease resistance.[178,179] POPG, a critical component of lung surfactant, plays an essential role in its proper functioning by being sectioned into lipid reservoirs at the end of expiration, facilitated by surfactant proteins that aid in its adsorption to the surface.[24–26] According to the FDA, vitamin E

acetate was found in concentrations up to 88% in THC-containing e-cigarettes[180], suggesting that the amount of vitamin E acetate reaching the lungs can be significantly higher than the physiological concentration of approximately 1%[88] in phospholipids. Our findings indicate that α–tocopherol does not significantly change the phase behaviour of the POPG up to 75 mol % α–tocopherol, with the exception of increased film stability (higher collapse pressure). This suggests that the damage to the lung surfactant may be more related to interactions with saturated lipids (such as DPPC) rather than unsaturated lipids and may not significantly alter the formation of lipid reservoirs. Nor does the addition of 25 mol % and 50 mol % α–tocopherol to POPG greatly affect the compressibility of the fluid-phase POPG monolayer (Figure 3.2d). However, with the addition of 75 mol % α–tocopherol, the monolayer is less compressible for surface pressures up to 20 mN/m which is attributed to the increase in the packing of monounsaturated lipids with α–tocopherol.

3.4.2. Deviations From Ideal Mixing

To assess the phospholipid-tocopherol interactions in the binary monolayer mixtures, molecular area deviations from the ideal mixing area (excess areas) were calculated for DPPC:α–tocopherol (Figure 3.3a) and POPG:α–tocopherol (Figure 3.3b). Numerical values for excess areas are presented in Table B2.

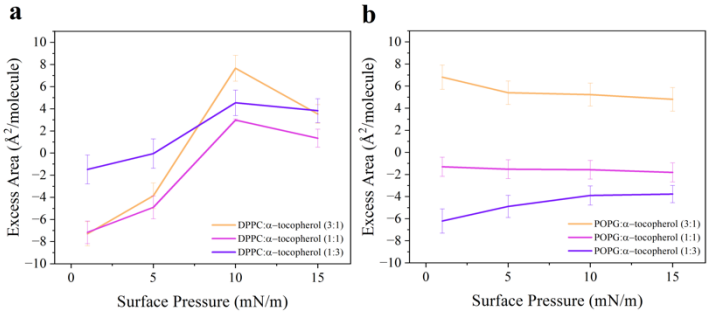

Figure 3.3. Molecular area deviations from the ideal mixing area (excess areas) for binary mixtures of (a) DPPC:α–tocopherol (3:1, 1:1, 1:3) and (b) POPG:α–tocopherol (3:1, 1:1, 1:3) at surface pressures of 1 mN/m, 5 mN/m, 10 mN/m and 15 mN/m. The standard deviations were calculated from triplicate measurements of the surface pressure–molecular area isotherms.

Positive deviations signify repulsive interactions leading to film expansion, whereas negative deviations signify attractive interactions and/or condensation.[114] Excess area calculations were

limited to a surface pressure of 15 mN/m due to the low collapse pressure of α–tocopherol. The addition of α–tocopherol to DPPC shifts the isotherms to lower molecular areas. A large shift of the pressure onset area to lower molecular areas is observed for low amounts added α–tocopherol (25 mol %). The isotherm shifts again with 50 mol % added α–tocopherol but there is very little difference in the pressure onset area between 50 and 75 mol %. At large molecular areas (low surface pressures, ≤5 mN/m) where DPPC exhibits a LE phase, all binary mixtures of DPPC:α–tocopherol show negative excess areas (Figure 3.3a and Table B2). In our previous work, α–tocopherol showed to have space-filling effect on the LE phase which led to negative excess areas for DPPC:α–tocopherol (3:1) at low surface pressures ≤5 mN/m.[158] These negative excess areas are similar in magnitude for 3:1 and 1:1 but the magnitude decreases significantly with high proportions of α–tocopherol. Thus, when DPPC is a major component and in a LE phase, α–tocopherol has a space filling effect. However, when α–tocopherol is the dominant component, there is little to no effect of mixing with a fluid phase DPPC and the system approaches ideality. By comparison the phosphocholine POPC, which forms a fluid phase at all surface pressures, exhibits negative excess areas with low proportions of tocopherol (25%) and positive excess areas with proportions of tocopherol > 50%.[84] However, it should be noted that for POPC, the calculation was based on the minimum molecular area before collapse, i.e. at high surface pressures, rather than the molecular areas for films at the same surface pressure.[84]

Upon compression to higher surface pressures (≥10 mN/m, where DPPC forms a condensed phase), positive excess areas are observed (Figure 3.3a). These positive deviations suggest repulsive interactions between DPPC and α–tocopherol resulting in a net expansion of the monolayer, an expansion that has previously been reported.[84] Moreover, in agreement with Neunert *et al.* the 1:1 mixture shows the smallest deviations from ideality at pressures that correspond to DPPC forming a condensed phase.[114] Thus, the deviations form ideality are both phase and surface pressure dependent.

By contrast, the mixing of POPG and α–tocopherol is independent of surface pressure (Figure 3.3b) for each POPG:α–tocopherol mixture, likely because POPG remains in a LE phase at all surface pressures up to collapse. The 3:1 mixture shows an expansion of the film with positive excess areas within + 5 to + 7 $Å^2$/molecule for all surface pressures (Table B2). Again, the 1:1 mixture is close to ideality with only a small contraction of the film and negative excess areas within – 1 to – 2 $Å^2$/molecule (Table B2). At higher proportions of tocopherol (the 1:3 mixture)

there is a more significant contraction of the film with negative excess areas within – 4 to – 6 $Å^2$/molecule (Table B2). If one calculates excess areas at 5 mN/m using the isotherms of Jurak *et al.* (Table B3) a similar trend is observed for binary mixtures of α–tocopherol with POPC (namely, positive excess areas for low proportions α–tocopherol, almost ideal at 1:1 ratios and negative excess areas at high proportions of α–tocopherol) .[84] Furthermore, this calculation reveals negative excess areas at all proportions for α–tocopherol mixed with DOPC, again with a minimum at the 1:1 ratio. Therefore, it appears degree of units of chain unsaturation, not headgroup interactions, governs the mixing properties of α–tocopherol as similar excess area trends are observed for both phospholipids POPG and POPC. Additionally, the 1:1 stoichiometry produces nearly ideal mixtures across multiple chain combinations and headgroups. These attractive interactions result in the formation of a more compact (less compressible) monolayer (Figure 3.2c).

3.4.3. Film Morphology (BAM)

The morphologies of DPPC, neat α–tocopherol and binary mixtures of DPPC:α–tocopherol (3:1, 1:1, 1:3) imaged with BAM are illustrated in Figure 3.4.

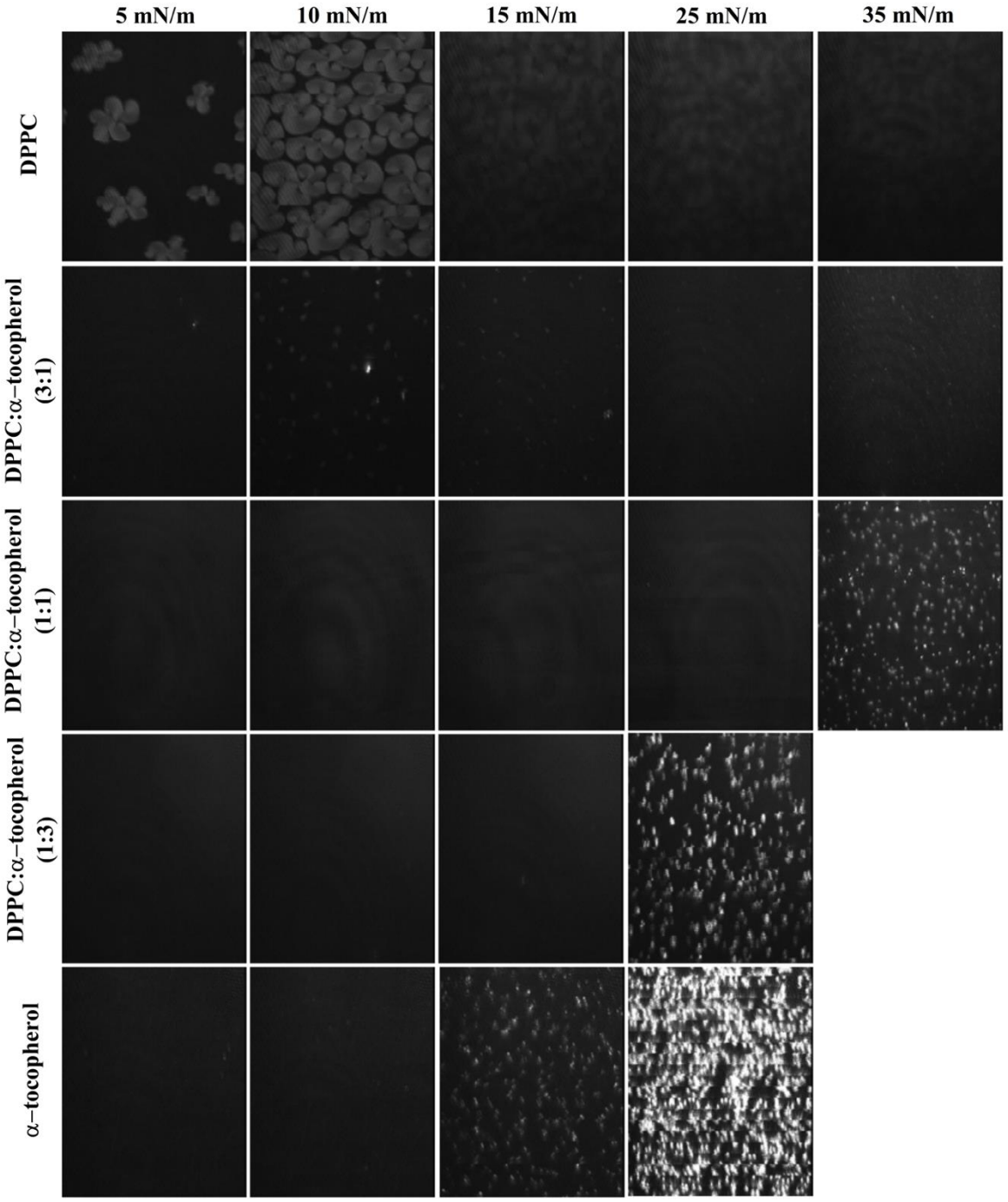

Figure 3.4. BAM images (220 μm × 275 μm) of DPPC, DPPC:α–tocopherol (3:1), DPPC:α–tocopherol (1:1), DPPC:α–tocopherol (1:3), and neat α–tocopherol (from top to bottom) as a function of the surface pressure (from left to right): 5 mN/m, 10 mN/m, 15 mN/m, 25 mN/m, and 35 mN/m. Note that only for DPPC:α–tocopherol (1:1) the furthest image to the right is taken after the first collapse at approximately 40 mN/m instead of 35 mN/m.

At 5 mN/m, DPPC shows the co-existence of a LE-LC phase where the LC phase is characterized by a well-established[181,182] triskelion shape in the presence of salt buffer subphase. Upon compression ≥ 15 mN/m the growth of the condensed phase leads to covering the whole monolayer in a homogeneous DPPC LC phase (Figure 3.4).[84,158]

With 25 mol % added α–tocopherol, there is a significant reduction in the LC phase across all surface pressures (higher proportion of LE phase), indicating a fluidization of the condensable DPPC-rich phase. This observation is consistent with the broadening of the LE-LC phase transition in surface pressure-area isotherms for DPPC:α–tocopherol (3:1) (Figure 3.2a). Additionally, the LC domains are much smaller and no longer triskelion in shape, instead having a more circular morphology that persists even at high pressures of 35 mN/m (see Figure B1 for an enhanced contrast image). For the same lipid system, Jurak *et al.* reported the absence of any condensed phase domains with added 25 mol % α–tocopherol[84], however this may be due to the lower resolution of the BAM used. With 50 mol % α–tocopherol, no discernable LC phase is observed up to 25 mN/m, however, by 35 mN/m, small circular domains with varying brightness levels appear while with 75 mol % α–tocopherol, these appear already at a surface pressure 25 mN/m (Figure 3.4). These bright domains correspond to the expulsion of α–tocopherol from the monolayer surface as the morphology corresponds to that of the collapse of α–tocopherol (Figure 3.4). Regardless of the proportion of α–tocopherol added, there is a consistent reduction in the LC phase and the emergence of bright 3D protrusions occurring at lower surface pressures in the following order of α–tocopherol added in DPPC: 25 mol %, 50 mol % and 75 mol %. The larger amount of the LE phase correlates well to the decrease in compressibility moduli observed for all the DPPC:α–tocopherol mixed monolayer films compared to DPPC alone (Figure 3.4 and Figure 3.2c) and the positive excess areas at high surface pressures (Figure 3.3a).

The morphologies of POPG, neat α–tocopherol and binary mixtures of POPG:α–tocopherol (3:1, 1:1, 1:3) imaged with BAM are illustrated in Figure 3.5. For POPG, a homogenous LE phase is observed in BAM measurements for all surface pressures. All mixtures of POPG with α–tocopherol also show a homogeneous film up to 15 mN/m. While POPG:α–tocopherol (3:1) remains homogeneous up to 35 mN/m, both POPG:α–tocopherol (1:1) and POPG:α–tocopherol (1:3) form small bright circular domains by 35 mN/m consistent with the expulsion of α–tocopherol.

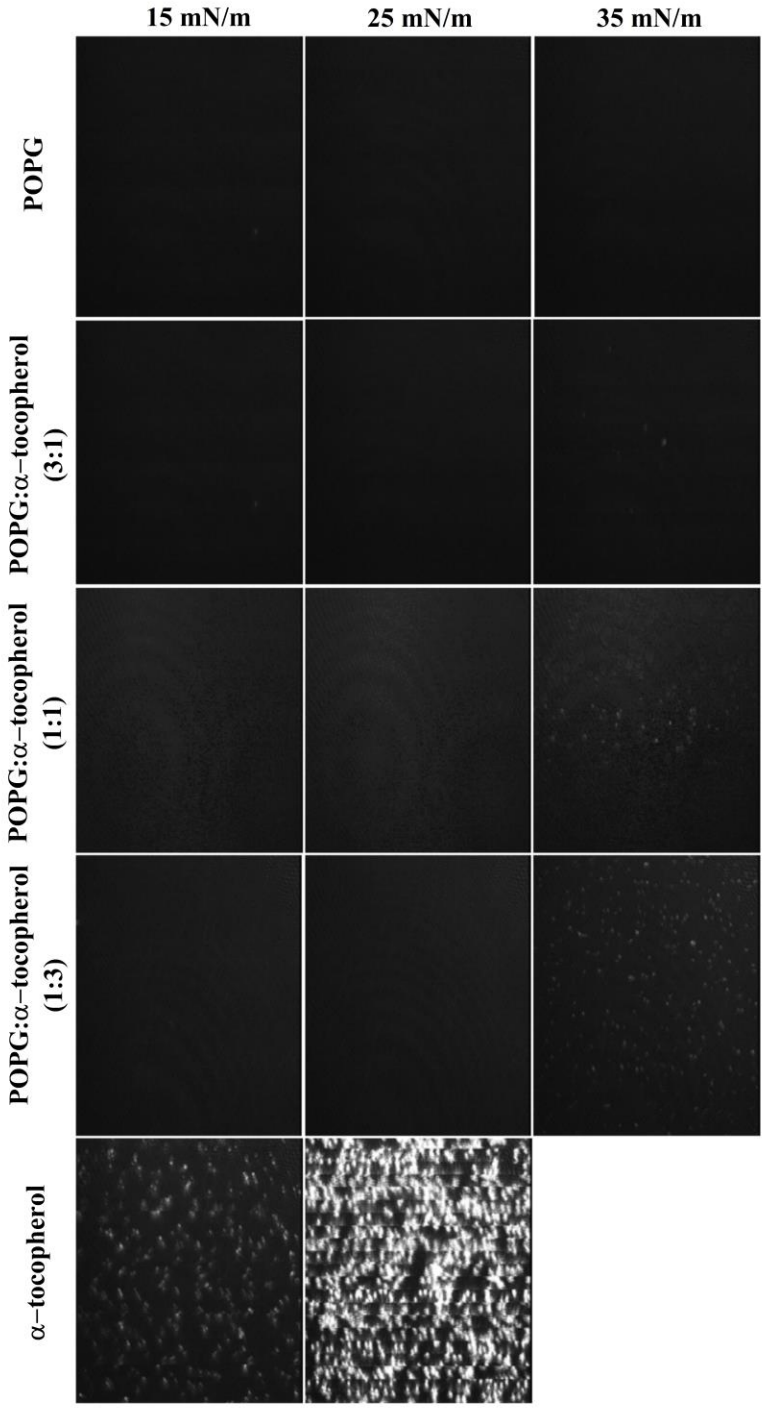

Figure 3.5. BAM images (220 μm × 275 μm) of POPG, POPG:α–tocopherol (3:1), POPG:α–tocopherol (1:1), POPG:α–tocopherol (1:3), and neat α–tocopherol (from top to bottom) as a function of the surface pressure (from left to right): ~15 mN/m, ~25 mN/m, and ~35 mN/m.

3.4.4. Film Morphology (AFM)

To probe the morphology of DPPC and mixtures of DPPC and α–tocopherol in more detail, AFM imaging was employed (Figures 3.6 and 3.7).

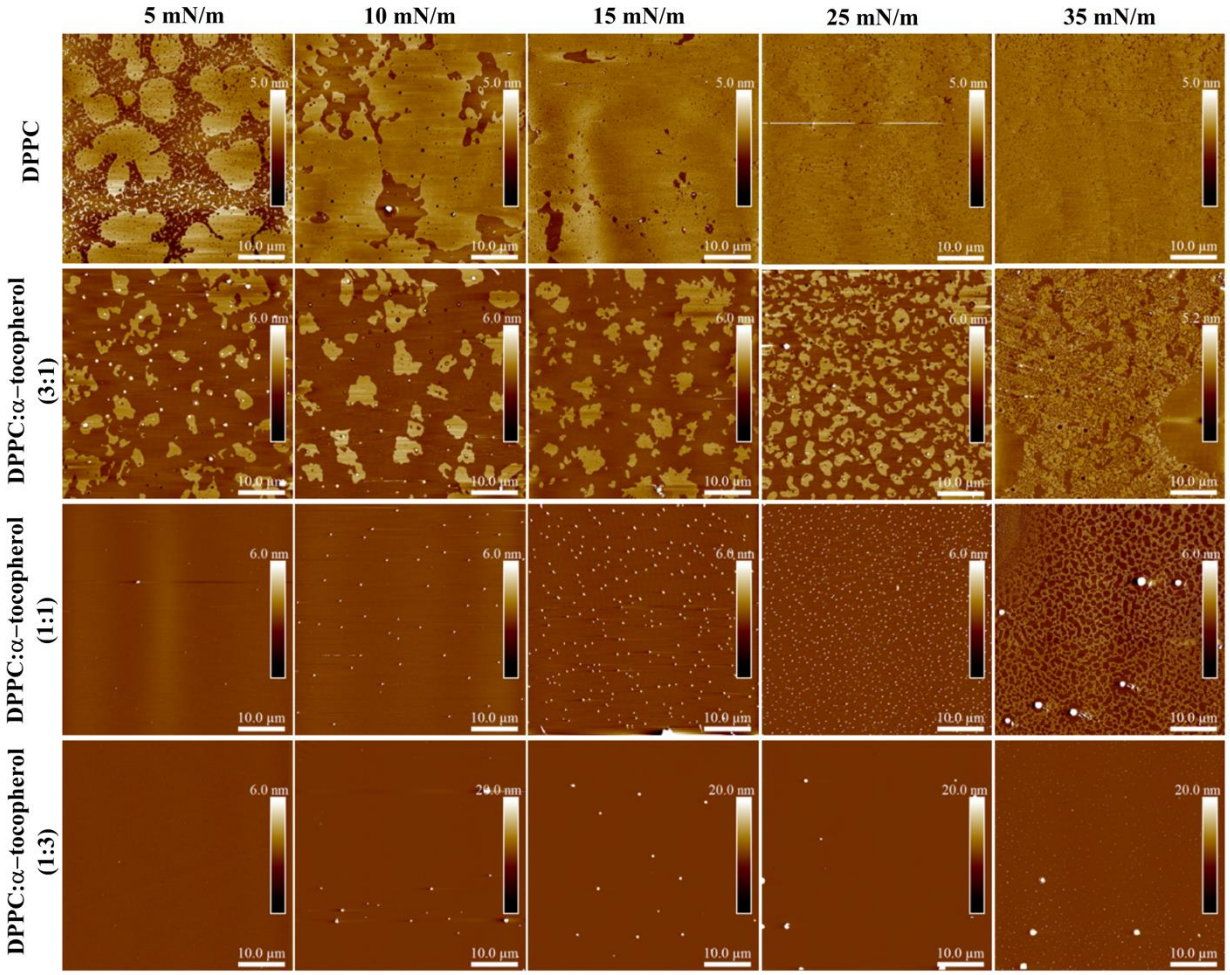

Figure 3.6. AFM images of monolayer films transferred onto mica at 5 mN/m, 10 mN/m, 15 mN/m, 25 mN/m, and 35 mN/m (LEFT to RIGHT) for DPPC, DPPC:α–tocopherol (3:1), DPPC:α–tocopherol (1:1), and DPPC:α–tocopherol (1:3) (TOP to BOTTOM). Note that all images are scanned at a size of 50 μm × 50 μm.

In agreement with BAM imaging, the DPPC shows an LE-LC phase co-existence from 5 mN/m that fully coalesces by 15 mN/m (Figure 3.6). Similarly, the clear reduction in the coverage by the LC phase at all pressures for 25 mol % α–tocopherol, and lack of domain coalescence is evident. The domains formed are also smaller and irregular shaped. At a molar ratio of 1:1 there is an even greater reduction in coverage by an LC phase for all surface pressures. Smaller scan size images were obtained and are shown in Figure B2. Below 15 mN/m, very small in diameter (approx. 0.4 μm) bright spots appear that are 73 ± 25 nm in height that are likely the nucleation sites for the

collapse of the α–tocopherol. These protrusions would be too small to be observed by BAM. By 15 mN/m, two populations are observed, namely domains corresponding to an LC phase (1.3 nm in height relative to the LE phase and with domain widths less than 1 μm) and the same higher protrusions. By 35 mN/m, the morphology is distinctly different and exhibits at least three different populations of domains. The LC phase domains form an interconnected network. A new population of nanodomains that are on average 3.5 nm above the LE phase and are primarily located at the perimeter of the condensed phase domains (Figure 3.7a). Finally, large-diameter, very tall protrusions that can be easily visualized by BAM begin to appear. Tocopherols are proposed to have linactant activity[103,158] and other strong linactants have shown to partition at the phase boundaries and to relax deformed domains back to a circular morphology[183], similar to the circular morphology observed here with increasing proportion of α–tocopherol (Figure 3.6 and Figure B2). The absence of a visible condensed phase in BAM measurements for DPPC:α–tocopherol (1:1) is due to the LC domains being below the lateral resolution of BAM, however AFM highlights that the DPPC condensed phase is not completely fluidized at the 1:1 DPPC:α–tocopherol ratio, as was previously reported (Figure 3.4, Figure 3.6, Figure B2).[84]

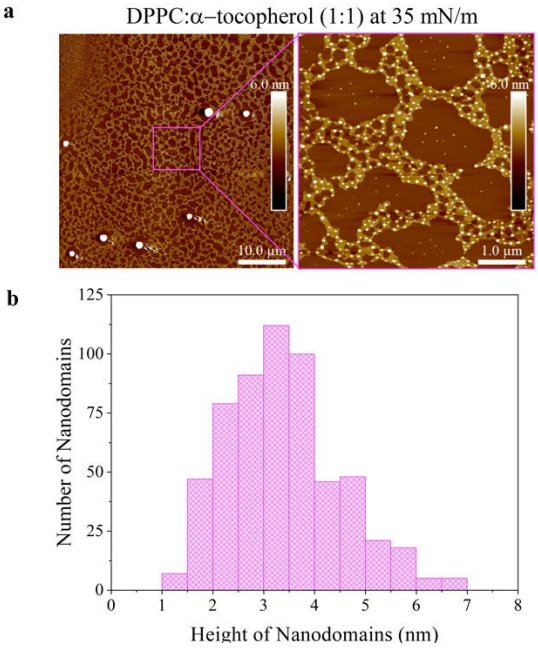

Figure 3.7. (a) AFM images of DPPC:α–tocopherol (1:1) at a surface pressure of 35 mN/m taken at a scan size of 50 μm × 50 μm (LEFT), and 5 μm × 5 μm (RIGHT). (b) Histogram for the height of the nanodomains (at the boundaries of condensed phase domains) observed in DPPC:α–tocopherol (1:1). The histogram presents the heights of nanodomains relative to the lower continuous phase (n>500) using pooled data from two independently prepared samples, minimum three areas imaged per sample.

The nanodomain heights relative to the lower phase are distributed from 1.0 nm to 7.0 nm, with the highest populated bins being 2.0 nm to 4.0 nm (Figure 3.7b). The height of the lowest phase (consisting of DPPC and α–tocopherol) is estimated at 1.8 nm to 2.0 nm. The height of an untilted α–tocopherol bilayer, calculated assuming full extension of the chain, is approximately 4.6 nm and a trilayer would be approximately 6.9 nm (note that these values represent maximal lengths as the α–tocopherol chain is unlikely to be fully extended). The nanodomain heights correlate well with α–tocopherol bilayers and multilayers, which could even be interdigitated. These observations suggest that α–tocopherol, due to its linactant properties, clusters at the phase boundary between the LE and condensed phase and can stack as bi- and/or trilayers that can grow laterally. Quinn *et al.* showed α–tocopherol to phase separate into enriched α–tocopherol domains in DPPC:α–tocopherol bilayers using low-angle X–ray diffraction.[184] The α–tocopherol-rich domains were not dependent on the phase state of the DPPC (gel or liquid crystalline) in the multilamellar dispersion. Additionally, they observed the positional correlation of the α–tocopherol enriched domains between bilayers which would agree with α–tocopherol multilayer formation in the mixed monolayers at 35 mN/m which is the surface pressure generally accepted to correlate to a bilayer. Each nanodomain may also represent the initial points of the α–tocopherol expulsion, i.e. the nucleation of the larger aggregates. These larger bright aggregates reach heights of 72 ± 30 nm, are observed by both BAM and AFM (Figure 3.4 and 3.6), but are only present after the α–tocopherol collapse. With the addition of 75 mol % α–tocopherol in DPPC, the monolayer only forms an LE phase at surface pressures < 35 mN/m and above these pressures condensed phase domains are observed but are too small laterally for their height to be accurately determined. In all mixtures, as the proportion of α–tocopherol increases, there is an increase in the proportion of LE phase at all surface pressures which correlates well to the decrease in compressibility moduli observed (Figure 3.6 and Figure 3.2c).

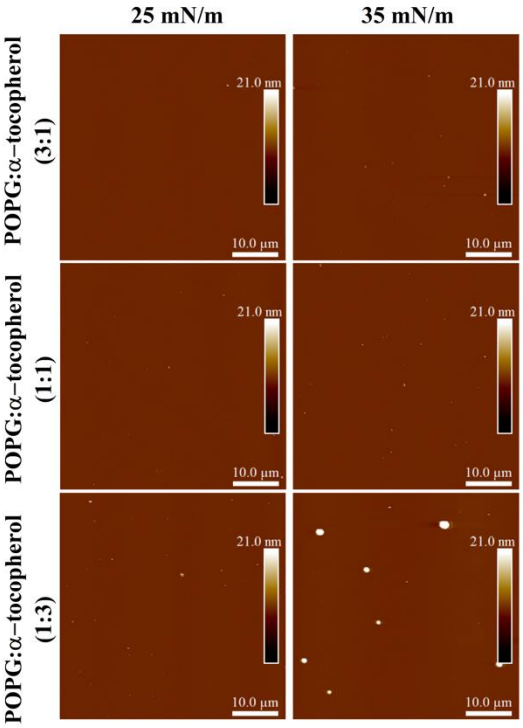

Figure 3.8. AFM images of monolayer films transferred onto mica at 25 mN/m, and 35 mN/m (LEFT to RIGHT) for POPG:α–tocopherol (3:1), POPG:α–tocopherol (1:1), and POPG:α–tocopherol (1:3) (TOP to BOTTOM). Note that all images are scanned at a size of 50 µm × 50 µm.

The α–tocopherol appears to mix fully with POPG at all mixing ratios, observed as a homogeneous monolayer, and the film remains in the LE phase at all surface pressures (Figure 3.8). The same bright aggregates appear after the independent collapse of α–tocopherol. As POPG is not a main component in mammalian membranes (aside from lung surfactant), its miscibility with α–tocopherol has been much less studied than the analogous phosphocholine POPC. Excess areas of POPC with α–tocopherol[84] and POPG with α–tocopherol up to 5 mN/m follow the same trends and both appear miscible. The miscibility is governed by the chain combination and not the headgroup chemical structure as previously seen where monounsaturated phosphocholines and phosphoglycerols behave similarly, evidenced by surface pressure-area isotherms and excess area calculations. The effects of α–tocopherol on the morphology and miscibility of POPG can be translated to its impact on POPC that is predominantly found in mammalian cell membranes.

3.4.5. Molecular Structure of Mixed Monolayers: GIXD & XR

For DPPC:α–tocopherol (1:1) *in situ* X–ray diffraction measurements were made at surface pressures 18 mN/m, 35 mN/m and 45 mN/m (Figure 3.9).

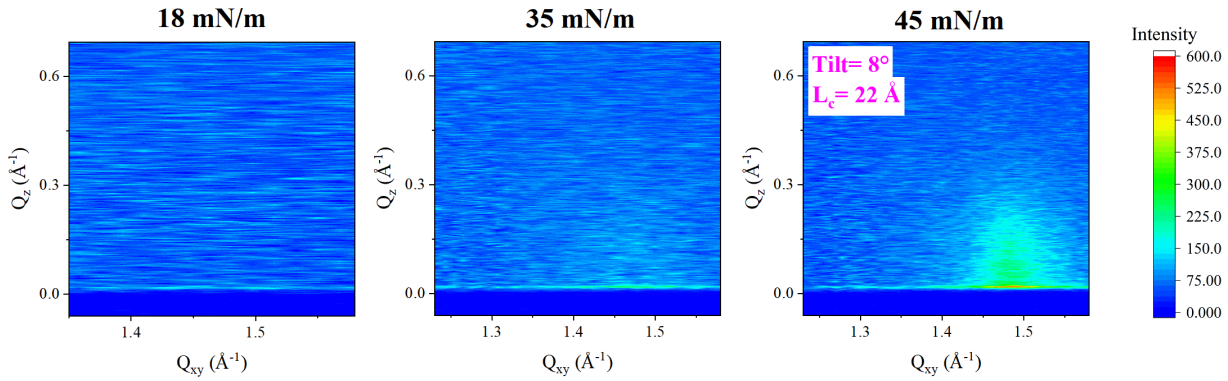

Figure 3.9. Contour plots of the X–ray intensities versus in-plane scattering vector components Q_{xy} and Q_z for DPPC:α–tocopherol (1:1) at surface pressures (left to right); 18 mN/m, 35 mN/m and 45 mN/m. Note fitted parameters produced a tilt angle of 8° and L_c in the Q_z direction of 22 Å.

At 18 mN/m the DPPC-rich phase domains do not generate enough surface coverage to produce a diffraction signal, since the monolayer is almost entirely occupied by a LE phase. At 35 mN/m, the DPPC:α–tocopherol (1:1) yields a very weak, diffuse signal again due to low coverage by condensed phase and/or a weakly correlated condensed phase. At 45 mN/m, the α–tocopherol has collapsed and been excluded from the monolayer, leaving the monolayer enriched in the DPPC-rich condensed phase which yields a stronger diffraction signal that corresponds to an alkyl chain tilt angle of 8° (Figure 3.9). A similar decrease in DPPC chain-tilt angle has also been observed for α–tocopherol added in DPPC:POPG model lung membranes at high compression states, owed to α–tocopherol intercalating between DPPC molecules in the DPPC-rich condensed phase.[158] Diffraction measurements were also obtained for POPG:α–tocopherol (1:1) shown in Figure B3 at a surface pressure 35 mN/m and shows no diffraction which correlate to a LE monolayer as also observed by BAM and AFM.

X–ray reflectivity numerical values for DPPC, POPG and DPPC or POPG:α–tocopherol (1:1) fitted parameters for the thickness and electron density found at the tail and headgroup region are shown in Table 3.1. The DPPC condensed phase has a 14.4 Å thick tail region that decreases to 11.1 Å with the addition of 50 mol % α–tocopherol since the film is dominated by a LE phase

which has a lower thickness. There is also an increase headgroup layer thickness from 7.1 Å (without α–tocopherol) to 8.7 Å (with 50 mol % α–tocopherol), attributed to the molecular placement of the chromanol ring at the air-water interphase.[121,158] The chromanol ring is not fully submerged into the subphase causing the increase in headgroup thickness. The electron density at the headgroup region decreases due to phosphocholine headgroups being further apart as the α–tocopherol inserts between DPPC molecules. As observed with the fluidization of DPPC, the POPG liquid expanded phase also has a thinner tail region of 10.1 Å the thickness of which is further reduced with the addition of α–tocopherol to 7.8 Å since α–tocopherol has a shorter hydrocarbon branched tail length than POPG. The decrease in headgroup thickness suggests that in POPG:α–tocopherol mixed monolayers, the chromanol moiety sits lower and induces a phosphoglycerol headgroup re-orientation. Similarly, in membranes with a phosphocholine headgroup, tocopherol's hydroxyl group submerges deeper with increase unsaturation of lipids, indicating a preference for positioning near oxidizable bonds.[86,89]

Table 3.1. Fitted parameters for XR data for DPPC and POPG with 50 mol % α–tocopherol at 22.0 ± 0.5 °C, and at 35 mN/m. *All data obtained with a TBS subphase except for POPG which is on an ultrapure water subphase.

	Tail		Headgroup	
System	Thickness (Å)	ρ ($e^{-}Å^{-3}$)	Thickness (Å)	ρ ($e^{-}Å^{-3}$)
DPPC	14.4	0.354	7.1	0.420
DPPC:α–tocopherol (1:1)	11.1	0.374	8.7	0.397
POPG*	10.1	0.371	11.9	0.398
POPG:α–tocopherol (1:1)	7.8	0.409	8.9	0.385

3.5. Conclusion

This study provides insights into the interactions between DPPC, POPG, and α–tocopherol, highlighting their miscibility and structural behaviors. POPG formed homogeneous monolayers with proportions of up to 75 mol % α–tocopherol. A near ideal mixture was achieved with 50 mol % α–tocopherol added to POPG which also stabilized the film to higher surface pressures, indicating a synergistic effect between the two and perhaps potential for designing lipid-antioxidant systems for therapies that optimize protective effects without disrupting lipid structures. To our knowledge, the miscibility of α–tocopherol with phosphoglycerols has not been studied. Herein we have shown that POPG shows similar mixing behaviour with α–tocopherol to POPC, underscoring the dependence of the mixing behaviour on alkyl chain combination rather than headgroup structure. Furthermore, a 1:1 ratio of α–tocopherol with either DPPC or POPG yields an almost ideal mixture, in agreement with other studies on unsaturated phosphocholines. The importance of this mixing ratio which is common across multiple chain and headgroup types, needs further investigation.

On the other hand, we find that DPPC and α–tocopherol exhibit partial miscibility, with α–tocopherol collapsing independently across all mixtures. The monolayer became more compressible and with little or no dependence on the α–tocopherol content. Notably, a condensed phase was still observed at 25 mol % and 50 mol % α–tocopherol, as revealed by AFM, in contrast to previous reports. The linactant capability of α–tocopherol was also observed through the formation of α–tocopherol nanodomains, primarily populating the interface between the condensed and LE phases with heights between 2 nm and 4 nm above the LE phase. The heights of nanodomains suggest the presence of α–tocopherol clusters characterized by bilayers and multilayers, which may also interdigitate. The formation of α–tocopherol nanodomains and their stability under compression within the lipid monolayer can be used in creating stable, organized nano-carriers for drug delivery. The approach envisions to develop therapies related to oxidative stress by specifically targeting unsaturated lipids. It also can involve engineering α–tocopherol-based nanodomains to encapsulate drugs, which will embed into membranes and enable targeted drug delivery into the cell.

Although early bilayer studies suggest that α–tocopherol would form clusters from either LE or condensed phase[184], we do not see that evidence especially with LE POPG, although phase

separation was evident with the DPPC condensed phase. This difference may be attributed to the differences in lipid composition used or the contrasting behaviours between bilayers and monolayers, revealing additional complexities not apparent in monolayer systems. Structural X–ray studies further demonstrated that α–tocopherol integrates into the DPPC condensed phase at concentrations as high as 50 mol % α–tocopherol, aligning with previous research that showed its incorporations at levels as low as 10 mol %.[158] Additionally, α–tocopherol was found position itself deeper within the monolayer of POPG compared to DPPC, highlighting how the degree of unsaturation influences antioxidant positioning in model membranes.

Chapter 4. Conclusions & Future Work

This research aimed to understand how vitamin E and vitamin E acetate, identified as illegal cutting agents in e-cigarettes, affected the lung surfactant. The urgency of this study is because of the many severe hospitalizations and deaths that occurred in 2019 due to EVALI, on top of the ongoing COVID-19 pandemic. Given the crucial role of the lungs as one of the first defense against airborne pathogens, addressing the severe lung injuries caused by vaping is important. These injuries to the lungs made it an important task to contribute to the little research that had been done on e-cigarette components and lung surfactant. The first part of this thesis shows the exposure of a lipid-based model lung surfactant membrane to α–tocopherol and α–tocopherol acetate at concentrations up to 20 mol % causes partitioning into both phases of the lung surfactant. This resulted in the fluidization of the membrane, potential alteration of lipid-reservoir formation, and retention of tocopherols within the membrane. This close association of tocopherols with the lipids, particularly their retention in the condensed phase at high surface pressures of 35 mN/m and 45 mN/m, where the surfactant begins to rearrange to lower surface tensions and prevent lung collapse, can disrupt lung function and can be a significant contributor to EVALI that is characteristic of shortness of breath or worse the collapse of the lungs.

Given α–tocopherol partitions to both the fluid and condensed phase of the lung surfactant, the next part of this thesis undertook a more in-depth study with its mixing behavior with the individual components, specifically DPPC and POPG. Both are common membrane lipids and thus the findings have broader implication for understanding vitamin E as a membrane soluble antioxidant. We found that α–tocopherol for all concentrations between 25 mol % and 75 mol % caused a significant impact on the saturated phosphocholine lipid monolayer. We observed that α–tocopherol significantly affected the saturated phosphatidylcholine lipid monolayer at concentrations ranging from 25 mol % to 75 mol %, while the monounsaturated phosphatidylglycerol lipid monolayer was minimally impacted and had a synergistic effect across all concentrations. The deterioration of cell membranes is very much associated to oxidative stress which damages unsaturated lipids, resulting in the increase of cell permeability, or worse cell death. The increase in permeability allows for other molecules, including free radicals, to leak into the cell, potentially harming proteins and other crucial molecules needed for proper cell functioning. The influx of free radicals in the cell further exacerbate oxidative stress by causing

DNA damage.[185] Given that vitamin E is one of the most powerful antioxidants, understanding how unsaturated lipids can withstand high levels of vitamin E (up to 75 mol %), offers valuable insights for improving treatment options for diseases related to oxidative stress.

In practice, e-cigarettes reach extremely high temperatures to generate an aerosol before its inhalation, and this elevated heat can induce chemical reactions leading to the introduction of new breakdown products from vaping liquids into your lungs. LeBouf *et al.* heated vitamin E oil (amongst other oils) at temperatures of up 250 ºC then analyzed the constituents by gas chromatography-mass spectrometry.[126] Heating vitamin E acetate produced hazardous substances such as acetic acid, acetone, and formic acid.[126] These chemicals could pose significant respiratory and systemic health risks on top of the parental vitamin E acetate molecule. The impact of these molecules on lung surfactant physicochemical properties is underexplored in the literature and could provide valuable insights into the mechanisms underlying EVALI damage.

Some of our preliminary experiments (not included in the manuscripts) using TGA-MS of vitamin E acetate showed that the most relevant compounds generated include trimethyldodecanol and trimethyldodecane, both of which are lipophilic and thus likely to be retained in the lung surfactant membrane like previously seen with vitamin E acetate. Neither breakdown product has yet to be highlighted in current literature and studied in the context of the lung surfactant. The other molecule of interest that we identified is duroquinone, highlighted in previous literature, which is a class of quinones that are known for their ability to undergo aggressive reversible redox reactions.[186] If in the presence of oxygen which is in the lungs there will likely be redox reactions that can generate harmful reactive oxygen species that have been linked to activating the inflammatory pathway.[186] This is concerning because in vaping long-term may lead prolonged inflammation in the lungs which can ultimately damage tissues and impair respiratory function.

Since vitamin E has been banned from vaping solutions, the number of hospitalizations due to EVALI have decreased. However, e-cigarettes are still very popular to this day especially those containing nicotine and flavouring molecules which are highly addictive and appealing to users especially young users since they come in a variety of flavours. The latest results from Health Canada's Canadian Student Tobacco Alcohol and Drugs Survey, which surveyed approximately 61,000 high school students aged 12 to 17 as of June 2022, showed that 30% of teenagers have tried e-cigarettes.[187] The survey also found that the daily use averages 1 in 10 teenagers across all age groups, placing Canada among the highest globally and mirroring previous statistics from

2018.[187] These consistently high rates of daily vaping from 2018 to 2022 suggest that vaping is no longer just a temporary or passing trend but may instead become a long-term, persistent behavior among youth. This is especially concerning because statistics have shown people as young as 12 begin using e-cigarettes when the lungs are not yet fully matured. In fact, the lungs mature between the ages of 20-25, and by 35 begin to decline gradually as you age.[188] It is especially important for the public to know the dangers of some of the ingredients that make e-cigarette liquids. The importance of also understanding the impact of flavouring molecules on lung health is highlighted by another vaping-related disease, bronchiolitis obliterans, commonly known as "popcorn lungs".[189] This condition was originally identified in popcorn and caramel factory workers who developed irreversible lung damage, and in some cases death, due to the exposure of diacetyl, a buttery-flavored chemical.[189] Diacetyl has since been found in many e-cigarettes, where it is added to enhance flavors like vanilla.[189] This has led to the direct inhalation of this harmful chemical by active e-cigarette users, linking it to popcorn lungs. Understanding the impact of flavoring molecules on lung surfactant has been studied recently, with findings showing that flavouring molecules like menthol and aldehyde cherry can impair the function of lung surfactant.[159,161,190]

Overall, the findings of this thesis highlight the need for further investigation into studying the inhaled components from vaping liquids, especially those released when heated, to provide a more accurate assessment of their effects on the lung surfactant. Understanding the detrimental impacts of these components is essential because the lungs are the centerpiece of the respiratory system. As vaping continues to be popular, particularly among younger populations, it is vital to fully grasp the impacts associated with these inhaled substances to inform regulatory policies, guide public health recommendations, and individuals who are e-cigarette users from potential harm. Although this thesis focuses on short-term effects, it also clues into the impact of accumulation of α–tocopherol acetate in the lungs, since we look at concentrations of up to 20 mol %. This is significant because the amounts studied are much higher than the physiological levels typically found in cells, potentially revealing some of the accumulative impacts on lung health. Future studies should explore the effects of α–tocopherol on lung surfactant *in vivo* and investigate the long-term exposure of itself and its breakdown products.

Exploring the interaction of α–tocopherol with different phospholipid headgroups and varying levels of unsaturation is another study worth exploring. Phospholipids, which are key components of lung surfactant, and many other cellular membranes, can vary in their physical and chemical

properties based on their headgroups and degree of unsaturation. Understanding how α–tocopherol interacts with these different lipid environments could shed light on how it affects membrane stability, fluidity, and function under conditions relevant to lung and cell physiology.

References

(1) Rosilio, V. How Can Artificial Lipid Models Mimic the Complexity of Molecule–Membrane Interactions?; 2018; pp 107–146. https://doi.org/10.1016/bs.abl.2017.12.004.

(2) Swenson, H.; Stadie, N. P. Langmuir's Theory of Adsorption: A Centennial Review. *Langmuir* **2019**, *35* (16), 5409–5426. https://doi.org/10.1021/acs.langmuir.9b00154.

(3) Rojewska, M.; Smułek, W.; Kaczorek, E.; Prochaska, K. Langmuir Monolayer Techniques for the Investigation of Model Bacterial Membranes and Antibiotic Biodegradation Mechanisms. *Membranes (Basel)* **2021**, *11* (9), 707. https://doi.org/10.3390/membranes11090707.

(4) Wnętrzak, A.; Łątka, K.; Dynarowicz-Łątka, P. Interactions of Alkylphosphocholines with Model Membranes—The Langmuir Monolayer Study. *J Membr Biol* **2013**, *246* (6), 453–466. https://doi.org/10.1007/s00232-013-9557-4.

(5) Wydro, P. The Influence of Cardiolipin on Phosphatidylglycerol/Phosphatidylethanolamine Monolayers—Studies on Ternary Films Imitating Bacterial Membranes. *Colloids Surf B Biointerfaces* **2013**, *106*, 217–223. https://doi.org/10.1016/j.colsurfb.2013.01.053.

(6) Krajewska, M.; Dopierała, K.; Prochaska, K. Lipid–Protein Interactions in Langmuir Monolayers under Dynamically Varied Conditions. *J Phys Chem B* **2020**, *124* (1), 302–311. https://doi.org/10.1021/acs.jpcb.9b10351.

(7) Elderdfi, M.; Sikorski, A. F. Langmuir-Monolayer Methodologies for Characterizing Protein-Lipid Interactions. *Chem Phys Lipids* **2018**, *212*, 61–72. https://doi.org/10.1016/j.chemphyslip.2018.01.008.

(8) Villanueva, M. E.; Salas, S. D.; Vico, R. V. Role of the Nanoparticle Core and Capping on the Interaction with Lipid Monolayers; 2023; pp 63–102. https://doi.org/10.1016/bs.abl.2023.10.001.

(9) Behyan, S.; Borozenko, O.; Khan, A.; Faral, M.; Badia, A.; DeWolf, C. Nanoparticle-Induced Structural Changes in Lung Surfactant Membranes: An X-Ray Scattering Study. *Environ Sci Nano* **2018**, *5* (5), 1218–1230. https://doi.org/10.1039/C8EN00189H.

(10) Gravel-Tatta, L.; DeWolf, C.; Badia, A. Are Plant-Based Carbohydrate Nanoparticles Safe for Inhalation? Investigating Their Interactions with the Pulmonary Surfactant Using Langmuir Monolayers. *Langmuir* **2021**, *37* (42), 12365–12376. https://doi.org/10.1021/acs.langmuir.1c01906.

(11) Kmetko, J.; Datta, A.; Evmenenko, G.; Dutta, P. The Effects of Divalent Ions on Langmuir Monolayer and Subphase Structure: A Grazing-Incidence Diffraction and Bragg Rod Study. *J Phys Chem B* **2001**, *105* (44), 10818–10825. https://doi.org/10.1021/jp0122169.

(12) Guzmán, E.; Santini, E.; Ferrari, M.; Liggieri, L.; Ravera, F. Evaluation of the Impact of Carbonaceous Particles in the Mechanical Performance of Lipid Langmuir Monolayers. *Colloids Surf A Physicochem Eng Asp* **2022**, *634*, 127974. https://doi.org/10.1016/j.colsurfa.2021.127974.

(13) Keramatnejad, M.; DeWolf, C. Impact of Pollutant Ozone on the Biophysical Properties of Tear Film Lipid Layer Model Membranes. *Membranes (Basel)* **2023**, *13* (2), 165. https://doi.org/10.3390/membranes13020165.

(14) Neergaard, K. Neue Auffassungen Über Einen Grundbegriff Der Atemmechanik. *Z Gesamte Exp Med* **1929**, *66* (1), 373–394. https://doi.org/10.1007/BF02621963.

(15) Bae, C.-W.; Kim, C. Y.; Chung, S.-H.; Choi, Y.-S. History of Pulmonary Surfactant Replacement Therapy for Neonatal Respiratory Distress Syndrome in Korea. *J Korean Med Sci* **2019**, *34* (25). https://doi.org/10.3346/jkms.2019.34.e175.

(16) Ji, J.; Sun, L.; Luo, Z.; Zhang, Y.; Xianzheng, W.; Liao, Y.; Tong, X.; Shan, J. Potential Therapeutic Applications of Pulmonary Surfactant Lipids in the Host Defence Against Respiratory Viral Infections. *Front Immunol* **2021**, *12*. https://doi.org/10.3389/fimmu.2021.730022.

(17) Han, S.; Mallampalli, R. K. The Role of Surfactant in Lung Disease and Host Defense against Pulmonary Infections. *Ann Am Thorac Soc* **2015**, *12* (5), 765–774. https://doi.org/10.1513/AnnalsATS.201411-507FR.

(18) Ochs, M.; Nyengaard, J. R.; Jung, A.; Knudsen, L.; Voigt, M.; Wahlers, T.; Richter, J.; Gundersen, H. J. G. The Number of Alveoli in the Human Lung. *Am J Respir Crit Care Med* **2004**, *169* (1), 120–124. https://doi.org/10.1164/rccm.200308-1107OC.

(19) Stachowicz-Kuśnierz, A.; Korchowiec, B.; Rogalska, E.; Korchowiec, J. The Lung Surfactant Activity Probed with Molecular Dynamics Simulations. *Adv Colloid Interface Sci* **2022**, *304*, 102659. https://doi.org/10.1016/j.cis.2022.102659.

(20) Bachofen, H.; Schürch, S. Alveolar Surface Forces and Lung Architecture. *Comp Biochem Physiol A Mol Integr Physiol* **2001**, *129* (1), 183–193. https://doi.org/10.1016/S1095-6433(01)00315-4.

(21) Bachofen, H.; Schurch, S.; Urbinelli, M.; Weibel, E. R. Relations among Alveolar Surface Tension, Surface Area, Volume, and Recoil Pressure. *J Appl Physiol* **1987**, *62* (5), 1878–1887. https://doi.org/10.1152/jappl.1987.62.5.1878.

(22) Da Silva, E.; Vogel, U.; Hougaard, K. S.; Pérez-Gil, J.; Zuo, Y. Y.; Sørli, J. B. An Adverse Outcome Pathway for Lung Surfactant Function Inhibition Leading to Decreased Lung Function. *Curr Res Toxicol* **2021**, *2*, 225–236. https://doi.org/10.1016/j.crtox.2021.05.005.

(23) Possmayer, F.; Keating, N.; Zuo, Y. Y.; Petersen, N. O.; Veldhuizen, R. A. Pulmonary Surfactant Reduces Surface Tension to Low Values near Zero through a Modified Squeeze-Out Mechanism. *Biophys J* **2012**, *102* (3), 414a. https://doi.org/10.1016/j.bpj.2011.11.2263.

(24) Bangham, A. D.; Morley, C. J.; Phillips, M. C. The Physical Properties of an Effective Lung Surfactant. *Biochimica et Biophysica Acta (BBA) - Lipids and Lipid Metabolism* **1979**, *573* (3), 552–556. https://doi.org/10.1016/0005-2760(79)90229-7.

(25) Goerke, J.; Clements, J. A. Alveolar Surface Tension and Lung Surfactant. In *Comprehensive Physiology*; Wiley, 1986; pp 247–261. https://doi.org/10.1002/cphy.cp030316.

(26) Goerke, J. Pulmonary Surfactant: Functions and Molecular Composition. *Biochimica et Biophysica Acta (BBA) - Molecular Basis of Disease* **1998**, *1408* (2–3), 79–89. https://doi.org/10.1016/S0925-4439(98)00060-X.

(27) Wang, Z.; Gurel, O.; Baatz, J. E.; Notter, R. H. Differential Activity and Lack of Synergy of Lung Surfactant Proteins SP-B and SP-C in Interactions with Phospholipids. *J Lipid Res* **1996**, *37* (8), 1749–1760. https://doi.org/10.1016/S0022-2275(20)39118-5.

(28) Liekkinen, J.; Olżyńska, A.; Cwiklik, L.; Bernardino de la Serna, J.; Vattulainen, I.; Javanainen, M. Surfactant Proteins SP-B and SP-C in Pulmonary Surfactant Monolayers: Physical Properties Controlled by Specific Protein–Lipid Interactions. *Langmuir* **2023**, *39* (12), 4338–4350. https://doi.org/10.1021/acs.langmuir.2c03349.

(29) Krol, S.; Janshoff, A.; Ross, M.; Galla, H.-J. Structure and Function of Surfactant Protein B and C in Lipid Monolayers: A Scanning Force Microscopy Study. *Physical Chemistry Chemical Physics* **2000**, *2* (20), 4586–4593. https://doi.org/10.1039/b004145i.

(30) Takamoto, D. Y.; Lipp, M. M.; von Nahmen, A.; Lee, K. Y. C.; Waring, A. J.; Zasadzinski, J. A. Interaction of Lung Surfactant Proteins with Anionic Phospholipids. *Biophys J* **2001**, *81* (1), 153–169. https://doi.org/10.1016/S0006-3495(01)75688-3.

(31) Dhar, P.; Eck, E.; Israelachvili, J. N.; Lee, D. W.; Min, Y.; Ramachandran, A.; Waring, A. J.; Zasadzinski, J. A. Lipid-Protein Interactions Alter Line Tensions and Domain Size Distributions in Lung Surfactant Monolayers. *Biophys J* **2012**, *102* (1), 56–65. https://doi.org/10.1016/j.bpj.2011.11.4007.

(32) Krause, M. F.; Schulte-Mönting, J.; Hoehn, T. Rate of Surfactant Administration Influences Lung Function and Gas Exchange in a Surfactant-Deficient Rabbit Model. *Pediatr Pulmonol* **1998**, *25* (3), 196–204. https://doi.org/10.1002/(SICI)1099-0496(199803)25:3<196::AID-PPUL10>3.0.CO;2-1.

(33) Walther, F. J.; Hernández-Juviel, J.; Bruni, R.; Waring, A. J. Protein Composition of Synthetic Surfactant Affects Gas Exchange in Surfactant-Deficient Rats. *Pediatr Res* **1998**, *43* (5), 666–673. https://doi.org/10.1203/00006450-199805000-00016.

(34) Olmeda, B.; Villén, L.; Cruz, A.; Orellana, G.; Perez-Gil, J. Pulmonary Surfactant Layers Accelerate O2 Diffusion through the Air-Water Interface. *Biochimica et Biophysica Acta (BBA) - Biomembranes* **2010**, *1798* (6), 1281–1284. https://doi.org/10.1016/j.bbamem.2010.03.008.

(35) Jeon, G. W. Surfactant Preparations for Preterm Infants with Respiratory Distress Syndrome: Past, Present, and Future. *Korean J Pediatr* **2019**, *62* (5), 155–161. https://doi.org/10.3345/kjp.2018.07185.

(36) Soll, R. Synthetic Surfactant for Respiratory Distress Syndrome in Preterm Infants. *Cochrane Database of Systematic Reviews* **1998**, *2010* (1). https://doi.org/10.1002/14651858.CD001149.

(37) Fujiwara, T.; Chida, S.; Watabe, Y.; Maeta, H.; Morita, T.; Abe, T. ARTIFICIAL SURFACTANT THERAPY IN HYALINE-MEMBRANE DISEASE. *The Lancet* **1980**, *315* (8159), 55–59. https://doi.org/10.1016/S0140-6736(80)90489-4.

(38) Soll, R.; Blanco, F. Natural Surfactant Extract versus Synthetic Surfactant for Neonatal Respiratory Distress Syndrome. In *Cochrane Database of Systematic Reviews*; Soll, R., Ed.; John Wiley & Sons, Ltd: Chichester, UK, 2001. https://doi.org/10.1002/14651858.CD000144.

(39) Werner, A. K.; Koumans, E. H.; Chatham-Stephens, K.; Salvatore, P. P.; Armatas, C.; Byers, P.; Clark, C. R.; Ghinai, I.; Holzbauer, S. M.; Navarette, K. A.; Danielson, M. L.; Ellington, S.; Moritz, E. D.; Petersen, E. E.; Kiernan, E. A.; Baldwin, G. T.; Briss, P.; Jones, C. M.; King, B. A.; Krishnasamy, V.; Rose, D. A.; Reagan-Steiner, S. Hospitalizations and Deaths Associated with EVALI. *New England Journal of Medicine* **2020**, *382* (17), 1589–1598. https://doi.org/10.1056/NEJMoa1915314.

(40) Armatas, C.; Heinzerling, A.; Wilken, J. A. E-Cigarette, or Vaping, Product Use–Associated Lung Injury Cases During the COVID-19 Response — California, 2020. *MMWR Morb Mortal Wkly Rep* **2020**, *69* (25), 801–802. https://doi.org/10.15585/mmwr.mm6925a5.

(41) Blount, B. C.; Karwowski, M. P.; Shields, P. G.; Morel-Espinosa, M.; Valentin-Blasini, L.; Gardner, M.; Braselton, M.; Brosius, C. R.; Caron, K. T.; Chambers, D.; Corstvet, J.;

Cowan, E.; De Jesús, V. R.; Espinosa, P.; Fernandez, C.; Holder, C.; Kuklenyik, Z.; Kusovschi, J. D.; Newman, C.; Reis, G. B.; Rees, J.; Reese, C.; Silva, L.; Seyler, T.; Song, M.-A.; Sosnoff, C.; Spitzer, C. R.; Tevis, D.; Wang, L.; Watson, C.; Wewers, M. D.; Xia, B.; Heitkemper, D. T.; Ghinai, I.; Layden, J.; Briss, P.; King, B. A.; Delaney, L. J.; Jones, C. M.; Baldwin, G. T.; Patel, A.; Meaney-Delman, D.; Rose, D.; Krishnasamy, V.; Barr, J. R.; Thomas, J.; Pirkle, J. L. Vitamin E Acetate in Bronchoalveolar-Lavage Fluid Associated with EVALI. *New England Journal of Medicine* **2020**, *382* (8), 697–705. https://doi.org/10.1056/NEJMoa1916433.

(42) Morbidity and Mortality Weekly Report (MMWR). *Update: Characteristics of a Nationwide Outbreak of E-Cigarette, or Vaping, Product Use–Associated Lung Injury*; 2019.

(43) Duffy, B.; Li, L.; Lu, S.; Durocher, L.; Dittmar, M.; Delaney-Baldwin, E.; Panawennage, D.; LeMaster, D.; Navarette, K.; Spink, D. Analysis of Cannabinoid-Containing Fluids in Illicit Vaping Cartridges Recovered from Pulmonary Injury Patients: Identification of Vitamin E Acetate as a Major Diluent. *Toxics* **2020**, *8* (1), 8. https://doi.org/10.3390/toxics8010008.

(44) Jiang, H.; Ahmed, C. M. S.; Martin, T. J.; Canchola, A.; Oswald, I. W. H.; Garcia, J. A.; Chen, J. Y.; Koby, K. A.; Buchanan, A. J.; Zhao, Z.; Zhang, H.; Chen, K.; Lin, Y.-H. Chemical and Toxicological Characterization of Vaping Emission Products from Commonly Used Vape Juice Diluents. *Chem Res Toxicol* **2020**, *33* (8), 2157–2163. https://doi.org/10.1021/acs.chemrestox.0c00174.

(45) Blount, B. C.; Karwowski, M. P.; Morel-Espinosa, M.; Rees, J.; Sosnoff, C.; Cowan, E.; Gardner, M.; Wang, L.; Valentin-Blasini, L.; Silva, L.; De Jesús, V. R.; Kuklenyik, Z.; Watson, C.; Seyler, T.; Xia, B.; Chambers, D.; Briss, P.; King, B. A.; Delaney, L.; Jones, C. M.; Baldwin, G. T.; Barr, J. R.; Thomas, J.; Pirkle, J. L. Evaluation of Bronchoalveolar Lavage Fluid from Patients in an Outbreak of E-Cigarette, or Vaping, Product Use–Associated Lung Injury — 10 States, August–October 2019. *MMWR Morb Mortal Wkly Rep* **2019**, *68* (45), 1040–1041. https://doi.org/10.15585/mmwr.mm6845e2.

(46) Butt, Y. M.; Smith, M. L.; Tazelaar, H. D.; Vaszar, L. T.; Swanson, K. L.; Cecchini, M. J.; Boland, J. M.; Bois, M. C.; Boyum, J. H.; Froemming, A. T.; Khoor, A.; Mira-Avendano, I.; Patel, A.; Larsen, B. T. Pathology of Vaping-Associated Lung Injury. *New England Journal of Medicine* **2019**, *381* (18), 1780–1781. https://doi.org/10.1056/NEJMc1913069.

(47) Bhat, T. A.; Kalathil, S. G.; Bogner, P. N.; Blount, B. C.; Goniewicz, M. L.; Thanavala, Y. M. An Animal Model of Inhaled Vitamin E Acetate and EVALI-like Lung Injury. *New England Journal of Medicine* **2020**, *382* (12), 1175–1177. https://doi.org/10.1056/NEJMc2000231.

(48) Rose, J. J.; Krishnan-Sarin, S.; Exil, V. J.; Hamburg, N. M.; Fetterman, J. L.; Ichinose, F.; Perez-Pinzon, M. A.; Rezk-Hanna, M.; Williamson, E. Cardiopulmonary Impact of Electronic Cigarettes and Vaping Products: A Scientific Statement From the American Heart Association. *Circulation* **2023**, *148* (8), 703–728. https://doi.org/10.1161/CIR.0000000000001160.

(49) Cañadas, O.; Olmeda, B.; Alonso, A.; Pérez-Gil, J. Lipid–Protein and Protein–Protein Interactions in the Pulmonary Surfactant System and Their Role in Lung Homeostasis. *Int J Mol Sci* **2020**, *21* (10), 3708. https://doi.org/10.3390/ijms21103708.

(50) DiPasquale, M.; Gbadamosi, O.; Nguyen, M. H. L.; Castillo, S. R.; Rickeard, B. W.; Kelley, E. G.; Nagao, M.; Marquardt, D. A Mechanical Mechanism for Vitamin E Acetate in E-Cigarette/Vaping-Associated Lung Injury. *Chem Res Toxicol* **2020**, *33* (9), 2432–2440. https://doi.org/10.1021/acs.chemrestox.0c00212.

(51) van Bavel, N.; Lai, P.; Amrein, M.; Prenner, E. J. Biophysical Investigation of Vape Additives with Complex Lung Surfactant Model Systems and Physiological Surfactant Extracts. *JCIS Open* **2023**, *10*, 100085. https://doi.org/10.1016/j.jciso.2023.100085.

(52) van Bavel, N.; Lai, P.; Loebenberg, R.; Prenner, E. J. Vaping Additives Negatively Impact the Stability and Lateral Film Organization of Lung Surfactant Model Systems. *Nanomedicine* **2022**, *17* (12), 827–843. https://doi.org/10.2217/nnm-2021-0398.

(53) Ranard, K. M.; Erdman, J. W. Effects of Dietary RRR α-Tocopherol vs All-Racemic α-Tocopherol on Health Outcomes. *Nutr Rev* **2018**, *76* (3), 141–153. https://doi.org/10.1093/nutrit/nux067.

(54) EL-BELTAGI, H. S.; MOHAMED, H. I. Reactive Oxygen Species, Lipid Peroxidation and Antioxidative Defense Mechanism. *Not Bot Horti Agrobot Cluj Napoca* **2013**, *41* (1), 44. https://doi.org/10.15835/nbha4118929.

(55) Fritsche, S.; Wang, X.; Jung, C. Recent Advances in Our Understanding of Tocopherol Biosynthesis in Plants: An Overview of Key Genes, Functions, and Breeding of Vitamin E Improved Crops. *Antioxidants* **2017**, *6* (4), 99. https://doi.org/10.3390/antiox6040099.

(56) McLaughlin, P. J.; Weihrauch, J. L. Vitamin E Content of Foods. *J Am Diet Assoc* **1979**, *75* (6), 647–665.

(57) Rimbach, G.; Moehring, J.; Huebbe, P.; Lodge, J. K. Gene-Regulatory Activity of α-Tocopherol. *Molecules* **2010**, *15* (3), 1746–1761. https://doi.org/10.3390/molecules15031746.

(58) Acuff, R.; Thedford, S.; Hidiroglou, N.; Papas, A.; Odom, T. Relative Bioavailability of RRR- and All-Rac-α-Tocopheryl Acetate in Humans: Studies Using Deuterated Compounds. *Am J Clin Nutr* **1994**, *60* (3), 397–402. https://doi.org/10.1093/ajcn/60.3.397.

(59) Burton, G.; Traber, M.; Acuff, R.; Walters, D.; Kayden, H.; Hughes, L.; Ingold, K. Human Plasma and Tissue Alpha-Tocopherol Concentrations in Response to Supplementation with Deuterated Natural and Synthetic Vitamin E. *Am J Clin Nutr* **1998**, *67* (4), 669–684. https://doi.org/10.1093/ajcn/67.4.669.

(60) Leonard, S. W.; Terasawa, Y.; Farese Jr, R. V; Traber, M. G. Incorporation of Deuterated RRR- or All-Rac-α-Tocopherol in Plasma and Tissues of α-Tocopherol Transfer Protein–Null Mice. *Am J Clin Nutr* **2002**, *75* (3), 555–560. https://doi.org/10.1093/ajcn/75.3.555.

(61) Morton, L. W.; Caccetta, R. A.; Puddey, I. B.; Croft, K. D. Chemistry And Biological Effects Of Dietary Phenolic Compounds: Relevance To Cardiovascular Disease. *Clin Exp Pharmacol Physiol* **2000**, *27* (3), 152–159. https://doi.org/10.1046/j.1440-1681.2000.03214.x.

(62) Jeffrey, G. P.; Muller, D. P. R.; Burroughs, A. K.; Matthews, S.; Kemp, C.; Epstein, O.; Metcalfe, T. A.; Southam, E.; Tazir-Melboucy, M.; Thomas, P. K.; McIntyre, N. Vitamin E Deficiency and Its Clinical Significance in Adults with Primary Biliary Cirrhosis and Other Forms of Chronic Liver Disease. *J Hepatol* **1987**, *4* (3), 307–317. https://doi.org/10.1016/S0168-8278(87)80539-1.

(63) Kono, N.; Arai, H. Intracellular Transport of Fat-Soluble Vitamins A and E. *Traffic* **2015**, *16* (1), 19–34. https://doi.org/10.1111/tra.12231.

(64) Lobo, V.; Patil, A.; Phatak, A.; Chandra, N. Free Radicals, Antioxidants and Functional Foods: Impact on Human Health. *Pharmacogn Rev* **2010**, *4* (8), 118. https://doi.org/10.4103/0973-7847.70902.
(65) Cummings, M. J.; Mattill, H. A. The Auto-Oxidation of Fats with Reference to Their Destructive Effect on Vitamin E. *J Nutr* **1931**, *3* (4), 421–432. https://doi.org/10.1093/jn/3.4.421.
(66) Traber, M. G. Vitamin E Inadequacy in Humans: Causes and Consequences. *Advances in Nutrition* **2014**, *5* (5), 503–514. https://doi.org/10.3945/an.114.006254.
(67) Tappel, A. L.; Brown, W. D.; Zalkin, H.; Maier, V. P. Unsaturated Lipid Peroxidation Catalyzed by Hematin Compounds and Its Inhibition by Vitamin E [1]. *J Am Oil Chem Soc* **1961**, *38* (1), 5–9. https://doi.org/10.1007/BF02633109.
(68) Niki, E. Lipid Oxidation That Is, and Is Not, Inhibited by Vitamin E: Consideration about Physiological Functions of Vitamin E. *Free Radic Biol Med* **2021**, *176*, 1–15. https://doi.org/10.1016/j.freeradbiomed.2021.09.001.
(69) Ramana, K. V.; Srivastava, S.; Singhal, S. S. Lipid Peroxidation Products in Human Health and Disease 2019. *Oxid Med Cell Longev* **2019**, *2019*, 1–2. https://doi.org/10.1155/2019/7147235.
(70) Zingg, J.-M. Vitamin E: A Role in Signal Transduction. *Annu Rev Nutr* **2015**, *35* (1), 135–173. https://doi.org/10.1146/annurev-nutr-071714-034347.
(71) Food and Drug Administration. *Food Labeling: Revision of the Nutrition and Supplement Facts Labels*.
(72) U.S. Department of Agriculture. FoodData Central. *Agricultural Research Service* **2019**.
(73) M. Jasim, A.; J. Jawad, M. Pharmaceutical Applications of Vitamin E TPGS; 2021. https://doi.org/10.5772/intechopen.97474.
(74) Leme Goto, P.; Cinato, M.; Merachli, F.; Vons, B.; Jimenez, T.; Marsal, D.; Todua, N.; Loi, H.; Santin, Y.; Cassel, S.; Blanzat, M.; Tronchere, H.; Dejugnat, C.; Kunduzova, O.; Boal, F. In Vitro and in Vivo Cardioprotective and Metabolic Efficacy of Vitamin E TPGS/Apelin. *J Mol Cell Cardiol* **2020**, *138*, 165–174. https://doi.org/10.1016/j.yjmcc.2019.12.001.
(75) Abraham, A.; Kattoor, A. J.; Saldeen, T.; Mehta, J. L. Vitamin E and Its Anticancer Effects. *Crit Rev Food Sci Nutr* **2019**, *59* (17), 2831–2838. https://doi.org/10.1080/10408398.2018.1474169.
(76) Keen, M.; Hassan, I. Vitamin E in Dermatology. *Indian Dermatol Online J* **2016**, *7* (4), 311. https://doi.org/10.4103/2229-5178.185494.
(77) Burke, K. E.; Clive, J.; Combs, G. F.; Commisso, J.; Keen, C. L.; Nakamura, R. M. Effects of Topical and Oral Vitamin E on Pigmentation and Skin Cancer Induced by Ultraviolet Irradiation in Skh:2 Hairless Mice. *Nutr Cancer* **2000**, *38* (1), 87–97. https://doi.org/10.1207/S15327914NC381_13.
(78) Ricciarelli, R.; Maroni, P.; Özer, N.; Zingg, J.-M.; Azzi, A. Age-Dependent Increase of Collagenase Expression Can Be Reduced by α-Tocopherol via Protein Kinase C Inhibition. *Free Radic Biol Med* **1999**, *27* (7–8), 729–737. https://doi.org/10.1016/S0891-5849(99)00007-6.
(79) Makpol, S.; Jam, F. A.; Khor, S. C.; Ismail, Z.; Mohd Yusof, Y. A.; Wan Ngah, W. Z. Comparative Effects of Biodynes, Tocotrienol-Rich Fraction, and Tocopherol in Enhancing Collagen Synthesis and Inhibiting Collagen Degradation in Stress-Induced Premature

Senescence Model of Human Diploid Fibroblasts. *Oxid Med Cell Longev* **2013**, *2013*, 1–8. https://doi.org/10.1155/2013/298574.

(80) Delgado, A.; Al-Hamimi, S.; Ramadan, M. F.; Wit, M. De; Durazzo, A.; Nyam, K. L.; Issaoui, M. Contribution of Tocols to Food Sensorial Properties, Stability, and Overall Quality. *J Food Qual* **2020**, *2020*, 1–8. https://doi.org/10.1155/2020/8885865.

(81) Wessling, C.; Nielsen, T.; Leufv&#65533;n, A. The Influence of ?-Tocopherol Concentration on the Stability of Linoleic Acid and the Properties of Low-Density Polyethylene. *Packaging Technology and Science* **2000**, *13* (1), 19–28. https://doi.org/10.1002/(SICI)1099-1522(200001/02)13:1<19::AID-PTS492>3.0.CO;2-B.

(82) Gerassimidou, S.; Geueke, B.; Groh, K. J.; Muncke, J.; Hahladakis, J. N.; Martin, O. V.; Iacovidou, E. Unpacking the Complexity of the Polyethylene Food Contact Articles Value Chain: A Chemicals Perspective. *J Hazard Mater* **2023**, *454*, 131422. https://doi.org/10.1016/j.jhazmat.2023.131422.

(83) *Food and Packaging Interactions*; Hotchkiss, J. H., Ed.; American Chemical Society: Washington, DC, 1988; Vol. 365. https://doi.org/10.1021/bk-1988-0365.

(84) Jurak, M.; Miñones Conde, J. Characterization of the Binary Mixed Monolayers of α-Tocopherol with Phospholipids at the Air-Water Interface. *Biochimica et Biophysica Acta (BBA) - Biomembranes* **2013**, *1828* (11), 2410–2418. https://doi.org/10.1016/j.bbamem.2013.07.005.

(85) DiPasquale, M.; Nguyen, M. H. L.; Pabst, G.; Marquardt, D. Partial Volumes of Phosphatidylcholines and Vitamin E: α-Tocopherol Prefers Disordered Membranes. *J Phys Chem B* **2022**, *126* (35), 6691–6699. https://doi.org/10.1021/acs.jpcb.2c04209.

(86) Harroun, , T A; Marquardt, , D; Katsaras, J.; Atkinson, J. Neutron Diffraction and Vitamin E. *J Phys Conf Ser* **2010**, *251*, 012039. https://doi.org/10.1088/1742-6596/251/1/012039.

(87) Marquardt, D.; Williams, J. A.; Kučerka, N.; Atkinson, J.; Wassall, S. R.; Katsaras, J.; Harroun, T. A. Tocopherol Activity Correlates with Its Location in a Membrane: A New Perspective on the Antioxidant Vitamin E. *J Am Chem Soc* **2013**, *135* (20), 7523–7533. https://doi.org/10.1021/ja312665r.

(88) Atkinson, J.; Epand, R. F.; Epand, R. M. Tocopherols and Tocotrienols in Membranes: A Critical Review. *Free Radic Biol Med* **2008**, *44* (5), 739–764. https://doi.org/10.1016/j.freeradbiomed.2007.11.010.

(89) Maggio, B.; Diplock, A. T.; Lucy, J. A. Interactions of Tocopherols and Ubiquinones with Monolayers of Phospholipids. *Biochemical Journal* **1977**, *161* (1), 111–121. https://doi.org/10.1042/bj1610111.

(90) Hincha, D. K. Effects of A-tocopherol (Vitamin E) on the Stability and Lipid Dynamics of Model Membranes Mimicking the Lipid Composition of Plant Chloroplast Membranes. *FEBS Lett* **2008**, *582* (25–26), 3687–3692. https://doi.org/10.1016/j.febslet.2008.10.002.

(91) Bradford, A.; Atkinson, J.; Fuller, N.; Rand, R. P. The Effect of Vitamin E on the Structure of Membrane Lipid Assemblies. *J Lipid Res* **2003**, *44* (10), 1940–1945. https://doi.org/10.1194/jlr.M300146-JLR200.

(92) Hénon, S.; Meunier, J. Microscope at the Brewster Angle: Direct Observation of First-Order Phase Transitions in Monolayers. *Review of Scientific Instruments* **1991**, *62* (4), 936–939. https://doi.org/10.1063/1.1142032.

(93) Hoenig, D.; Moebius, D. Direct Visualization of Monolayers at the Air-Water Interface by Brewster Angle Microscopy. *J Phys Chem* **1991**, *95* (12), 4590–4592. https://doi.org/10.1021/j100165a003.
(94) Daear, W.; Mahadeo, M.; Prenner, E. J. Applications of Brewster Angle Microscopy from Biological Materials to Biological Systems. *Biochimica et Biophysica Acta (BBA) - Biomembranes* **2017**, *1859* (10), 1749–1766. https://doi.org/10.1016/j.bbamem.2017.06.016.
(95) Peachey, N. M.; Eckhardt, C. J. Structural Studies of Ordered Monolayers Using Atomic Force Microscopy. *Micron* **1994**, *25* (3), 271–292. https://doi.org/10.1016/0968-4328(94)90033-7.
(96) Stefaniu, C.; Brezesinski, G. X-Ray Investigation of Monolayers Formed at the Soft Air/Water Interface. *Curr Opin Colloid Interface Sci* **2014**, *19* (3), 216–227. https://doi.org/10.1016/j.cocis.2014.01.004.
(97) Stefaniu, C.; Brezesinski, G. X-Ray Investigation of Monolayers Formed at the Soft Air/Water Interface. *Curr Opin Colloid Interface Sci* **2014**, *19* (3), 216–227. https://doi.org/10.1016/j.cocis.2014.01.004.
(98) Als-Nielsen, J.; Jacquemain, D.; Kjaer, K.; Leveiller, F.; Lahav, M.; Leiserowitz, L. Principles and Applications of Grazing Incidence X-Ray and Neutron Scattering from Ordered Molecular Monolayers at the Air-Water Interface. *Phys Rep* **1994**, *246* (5), 251–313. https://doi.org/10.1016/0370-1573(94)90046-9.
(99) Stefaniu, C.; Brezesinski, G. Grazing Incidence X-Ray Diffraction Studies of Condensed Double-Chain Phospholipid Monolayers Formed at the Soft Air/Water Interface. *Adv Colloid Interface Sci* **2014**, *207*, 265–279. https://doi.org/10.1016/j.cis.2014.01.005.
(100) Tikhonov, A. M.; Asadchikov, V. E.; Volkov, Y. O.; Roshchin, B. S.; Nuzhdin, A. D.; Makrinsky, K. I.; Ermakov, Y. A. X-Ray Reflectivity Study of Polylysine Adsorption on the Surface of DMPS Monolayers. *Membranes (Basel)* **2022**, *12* (12), 1223. https://doi.org/10.3390/membranes12121223.
(101) DiPasquale, M.; Nguyen, M. H. L.; Castillo, S. R.; Dib, I. J.; Kelley, E. G.; Marquardt, D. Vitamin E Does Not Disturb Polyunsaturated Fatty Acid Lipid Domains. *Biochemistry* **2022**, *61* (21), 2366–2376. https://doi.org/10.1021/acs.biochem.2c00405.
(102) Leng, X.; Zhu, F.; Wassall, S. R. Vitamin E Has Reduced Affinity for a Polyunsaturated Phospholipid: An Umbrella Sampling Molecular Dynamics Simulations Study. *J Phys Chem B* **2018**, *122* (35), 8351–8358. https://doi.org/10.1021/acs.jpcb.8b05016.
(103) Muddana, H. S.; Chiang, H. H.; Butler, P. J. Tuning Membrane Phase Separation Using Nonlipid Amphiphiles. *Biophys J* **2012**, *102* (3), 489–497. https://doi.org/10.1016/j.bpj.2011.12.033.
(104) Keating, E.; Rahman, L.; Francis, J.; Petersen, A.; Possmayer, F.; Veldhuizen, R.; Petersen, N. O. Effect of Cholesterol on the Biophysical and Physiological Properties of a Clinical Pulmonary Surfactant. *Biophys J* **2007**, *93* (4), 1391–1401. https://doi.org/10.1529/biophysj.106.099762.
(105) Olżyńska, A.; Zubek, M.; Roeselova, M.; Korchowiec, J.; Cwiklik, L. Mixed DPPC/POPC Monolayers: All-Atom Molecular Dynamics Simulations and Langmuir Monolayer Experiments. *Biochimica et Biophysica Acta (BBA) - Biomembranes* **2016**, *1858* (12), 3120–3130. https://doi.org/10.1016/j.bbamem.2016.09.015.

(106) Wüstneck, R.; Perez-Gil, J.; Wüstneck, N.; Cruz, A.; Fainerman, V. B.; Pison, U. Interfacial Properties of Pulmonary Surfactant Layers. *Adv Colloid Interface Sci* **2005**, *117* (1–3), 33–58. https://doi.org/10.1016/j.cis.2005.05.001.
(107) Parra, E.; Pérez-Gil, J. Composition, Structure and Mechanical Properties Define Performance of Pulmonary Surfactant Membranes and Films. *Chem Phys Lipids* **2015**, *185*, 153–175. https://doi.org/10.1016/j.chemphyslip.2014.09.002.
(108) Casals, C.; Cañadas, O. Role of Lipid Ordered/Disordered Phase Coexistence in Pulmonary Surfactant Function. *Biochimica et Biophysica Acta (BBA) - Biomembranes* **2012**, *1818* (11), 2550–2562. https://doi.org/10.1016/j.bbamem.2012.05.024.
(109) Lee, K. Y. C.; Majewski, J.; Kuhl, T. L.; Howes, P. B.; Kjaer, K.; Lipp, M. M.; Waring, A. J.; Zasadzinski, J. A.; Smith, G. S. Synchrotron X-Ray Study of Lung Surfactant-Specific Protein SP-B in Lipid Monolayers. *Biophys J* **2001**, *81* (1), 572–585. https://doi.org/10.1016/S0006-3495(01)75724-4.
(110) Yasmann, A.; Sukharev, S. Properties of Diphytanoyl Phospholipids at the Air–Water Interface. *Langmuir* **2015**, *31* (1), 350–357. https://doi.org/10.1021/la503800g.
(111) Ładniak, A.; Jurak, M.; Wiącek, A. E. Langmuir Monolayer Study of Phospholipid DPPC on the Titanium Dioxide–Chitosan–Hyaluronic Acid Subphases. *Adsorption* **2019**, *25* (3), 469–476. https://doi.org/10.1007/s10450-019-00037-1.
(112) Cutro, A. C.; Disalvo, E. A.; Frías, M. A. Effects of Phenylalanine on the Liquid-Expanded and Liquid-Condensed States of Phosphatidylcholine Monolayers. *Lipid Insights* **2019**, *12*, 117863531882092. https://doi.org/10.1177/1178635318820923.
(113) Cheng, S.; Li, S.; Tsona, N. T.; George, C.; Du, L. Insights into the Headgroup and Chain Length Dependence of Surface Characteristics of Organic-Coated Sea Spray Aerosols. *ACS Earth Space Chem* **2019**, *3* (4), 571–580. https://doi.org/10.1021/acsearthspacechem.8b00212.
(114) Neunert, G.; Hertmanowski, R.; Witkowski, S.; Polewski, K. Effect of Ester Moiety on Structural Properties of Binary Mixed Monolayers of Alpha-Tocopherol Derivatives with DPPC. *Molecules* **2022**, *27* (15), 4670. https://doi.org/10.3390/molecules27154670.
(115) Hasegawa, T.; Takeda, S.; Kawaguchi, A.; Umemura, J. Quantitative Analysis of Uniaxial Molecular Orientation in Langmuir-Blodgett Films by Infrared Reflection Spectroscopy. *Langmuir* **1995**, *11* (4), 1236–1243. https://doi.org/10.1021/la00004a032.
(116) Borozenko, O.; Faral, M.; Behyan, S.; Khan, A.; Coulombe, J.; DeWolf, C.; Badia, A. Silica Nanoparticle-Induced Structural Reorganizations in Pulmonary Surfactant Films: What Monolayer Compression Isotherms Do Not Say. *ACS Appl Nano Mater* **2018**, *1* (9), 5268–5278. https://doi.org/10.1021/acsanm.8b01259.
(117) Malcharek, S.; Hinz, A.; Hilterhaus, L.; Galla, H.-J. Multilayer Structures in Lipid Monolayer Films Containing Surfactant Protein C: Effects of Cholesterol and POPE. *Biophys J* **2005**, *88* (4), 2638–2649. https://doi.org/10.1529/biophysj.104.050823.
(118) Brezesinski, G.; Dietrich, A.; Struth, B.; Böhm, C.; Bouwman, W. G.; Kjaer, K.; Möhwald, H. Influence of Ether Linkages on the Structure of Double-Chain Phospholipid Monolayers. *Chem Phys Lipids* **1995**, *76* (2), 145–157. https://doi.org/10.1016/0009-3084(95)02439-P.
(119) Bringezu, F.; Ding, J.; Brezesinski, G.; Zasadzinski, J. A. Changes in Model Lung Surfactant Monolayers Induced by Palmitic Acid. *Langmuir* **2001**, *17* (15), 4641–4648. https://doi.org/10.1021/la0103158.

(120) Choi, S. Q.; Kim, K.; Fellows, C. M.; Cao, K. D.; Lin, B.; Lee, K. Y. C.; Squires, T. M.; Zasadzinski, J. A. Influence of Molecular Coherence on Surface Viscosity. *Langmuir* **2014**, *30* (29), 8829–8838. https://doi.org/10.1021/la501615g.
(121) GOMEZ-FERNANDEZ, J. C.; VILLALAIN, J.; ARANDA, F. J.; ORTIZ, A.; MICOL, V.; COUTINHO, A.; BERBERAN-SANTOS, M. N.; PRIETO, M. J. E. Localization of A-Tocopherol in Membranes. *Ann N Y Acad Sci* **1989**, *570* (1), 109–120. https://doi.org/10.1111/j.1749-6632.1989.tb14912.x.
(122) Layden, J. E.; Ghinai, I.; Pray, I.; Kimball, A.; Layer, M.; Tenforde, M. W.; Navon, L.; Hoots, B.; Salvatore, P. P.; Elderbrook, M.; Haupt, T.; Kanne, J.; Patel, M. T.; Saathoff-Huber, L.; King, B. A.; Schier, J. G.; Mikosz, C. A.; Meiman, J. Pulmonary Illness Related to E-Cigarette Use in Illinois and Wisconsin — Final Report. *New England Journal of Medicine* **2020**, *382* (10), 903–916. https://doi.org/10.1056/NEJMoa1911614.
(123) Baker, M. M.; Procter, T. D.; Belzak, L.; Ogunnaike-Cooke, S. Vaping-Associated Lung Illness (VALI) in Canada: A Descriptive Analysis of VALI Cases Reported from September 2019 to December 2020. *Health Promotion and Chronic Disease Prevention in Canada* **2022**, *42* (1), 37–44. https://doi.org/10.24095/hpcdp.42.1.06.
(124) Ghosh, A.; Ahmad, S.; Coakley, R. D.; Sassano, M. F.; Alexis, N. E.; Tarran, R. Lipid-Laden Macrophages Are Not Unique to Patients with E-Cigarette or Vaping Product Use–Associated Lung Injury. *Am J Respir Crit Care Med* **2021**, *203* (8), 1030–1033. https://doi.org/10.1164/rccm.202009-3507LE.
(125) Milad, N.; Morissette, M. C. Revisiting the Role of Pulmonary Surfactant in Chronic Inflammatory Lung Diseases and Environmental Exposure. *European Respiratory Review* **2021**, *30* (162), 210077. https://doi.org/10.1183/16000617.0077-2021.
(126) LeBouf, R. F.; Ranpara, A.; Ham, J.; Aldridge, M.; Fernandez, E.; Williams, K.; Burns, D. A.; Stefaniak, A. B. Chemical Emissions From Heated Vitamin E Acetate—Insights to Respiratory Risks From Electronic Cigarette Liquid Oil Diluents Used in the Aerosolization of Δ9-THC-Containing Products. *Front Public Health* **2022**, *9*. https://doi.org/10.3389/fpubh.2021.765168.
(127) Jiang, Q. Metabolism of Natural Forms of Vitamin E and Biological Actions of Vitamin E Metabolites. *Free Radic Biol Med* **2022**, *179*, 375–387. https://doi.org/10.1016/j.freeradbiomed.2021.11.012.
(128) Jiang, Q. Natural Forms of Vitamin E: Metabolism, Antioxidant, and Anti-Inflammatory Activities and Their Role in Disease Prevention and Therapy. *Free Radic Biol Med* **2014**, *72*, 76–90. https://doi.org/10.1016/j.freeradbiomed.2014.03.035.
(129) Xiaoyuan Wang, P. J. Q. The Location and Function of Vitamin E in Membranes (Review). *Mol Membr Biol* **2000**, *17* (3), 143–156. https://doi.org/10.1080/09687680010000311.
(130) Howard, A. C.; McNeil, A. K.; McNeil, P. L. Promotion of Plasma Membrane Repair by Vitamin E. *Nat Commun* **2011**, *2* (1), 597. https://doi.org/10.1038/ncomms1594.
(131) Napolitano, G.; Fasciolo, G.; Di Meo, S.; Venditti, P. Vitamin E Supplementation and Mitochondria in Experimental and Functional Hyperthyroidism: A Mini-Review. *Nutrients* **2019**, *11* (12), 2900. https://doi.org/10.3390/nu11122900.
(132) Lauridsen, C.; Jensen, S. K. α-Tocopherol Incorporation in Mitochondria and Microsomes upon Supranutritional Vitamin E Supplementation. *Genes Nutr* **2012**, *7* (4), 475–482. https://doi.org/10.1007/s12263-012-0286-6.

(133) Thomas, S. M.; Gebicki, J. M.; Dean, R. T. Radical Initiated α-Tocopherol Depletion and Lipid Peroxidation in Mitochondrial Membranes. *Biochimica et Biophysica Acta (BBA) - Lipids and Lipid Metabolism* **1989**, *1002* (2), 189–197. https://doi.org/10.1016/0005-2760(89)90286-5.
(134) Mustacich, D. J.; Leonard, S. W.; Patel, N. K.; Traber, M. G. α-Tocopherol β-Oxidation Localized to Rat Liver Mitochondria. *Free Radic Biol Med* **2010**, *48* (1), 73–81. https://doi.org/10.1016/j.freeradbiomed.2009.10.024.
(135) Irías-Mata, A.; Sus, N.; Flory, S.; Stock, D.; Woerner, D.; Podszun, M.; Frank, J. α-Tocopherol Transfer Protein Does Not Regulate the Cellular Uptake and Intracellular Distribution of α- and γ-Tocopherols and -Tocotrienols in Cultured Liver Cells. *Redox Biol* **2018**, *19*, 28–36. https://doi.org/10.1016/j.redox.2018.07.027.
(136) Yévenes, L. F.; Klein, A.; Castro, J. F.; Marín, T.; Leal, N.; Leighton, F.; Alvarez, A. R.; Zanlungo, S. Lysosomal Vitamin E Accumulation in Niemann–Pick Type C Disease. *Biochimica et Biophysica Acta (BBA) - Molecular Basis of Disease* **2012**, *1822* (2), 150–160. https://doi.org/10.1016/j.bbadis.2011.11.009.
(137) Buttriss, J. L.; Diplock, A. T. The Relationship between α-Tocopherol and Phospholipid Fatty Acids in Rat Liver Subcellular Membrane Fractions. *Biochimica et Biophysica Acta (BBA) - Lipids and Lipid Metabolism* **1988**, *962* (1), 81–90. https://doi.org/10.1016/0005-2760(88)90098-7.
(138) König, J.; Besoke, F.; Stuetz, W.; Malarski, A.; Jahreis, G.; Grune, T.; Höhn, A. Quantification of Age-related Changes of A-tocopherol in Lysosomal Membranes in Murine Tissues and Human Fibroblasts. *BioFactors* **2016**, *42* (3), 307–315. https://doi.org/10.1002/biof.1274.
(139) Stocker, A.; Azzi, A. Tocopherol-Binding Proteins: Their Function and Physiological Significance. *Antioxid Redox Signal* **2000**, *2* (3), 397–404. https://doi.org/10.1089/15230860050192170.
(140) Zingg, J. Vitamin E: Regulatory Role on Signal Transduction. *IUBMB Life* **2019**, *71* (4), 456–478. https://doi.org/10.1002/iub.1986.
(141) AZZI, A.; GYSIN, R.; KEMPNÁ, P.; MUNTEANU, A.; NEGIS, Y.; VILLACORTA, L.; VISARIUS, T.; ZINGG, J. Vitamin E Mediates Cell Signaling and Regulation of Gene Expression. *Ann N Y Acad Sci* **2004**, *1031* (1), 86–95. https://doi.org/10.1196/annals.1331.009.
(142) Md Amin, N. A.; Sheikh Abdul Kadir, S. H.; Arshad, A. H.; Abdul Aziz, N.; Abdul Nasir, N. A.; Ab Latip, N. Are Vitamin E Supplementation Beneficial for Female Gynaecology Health and Diseases? *Molecules* **2022**, *27* (6), 1896. https://doi.org/10.3390/molecules27061896.
(143) Cicek, N.; Eryilmaz, O. G.; Sarikaya, E.; Gulerman, C.; Genc, Y. Vitamin E Effect on Controlled Ovarian Stimulation of Unexplained Infertile Women. *J Assist Reprod Genet* **2012**, *29* (4), 325–328. https://doi.org/10.1007/s10815-012-9714-1.
(144) Kowdley, K. V.; Mason, J. B.; Meydani, S. N.; Cornwall, S.; Grand, R. J. Vitamin E Deficiency and Impaired Cellular Immunity Related to Intestinal Fat Malabsorption. *Gastroenterology* **1992**, *102* (6), 2139–2142. https://doi.org/10.1016/0016-5085(92)90344-X.

(145) Pae, M.; Wu, D. Nutritional Modulation of Age-Related Changes in the Immune System and Risk of Infection. *Nutrition Research* **2017**, *41*, 14–35. https://doi.org/10.1016/j.nutres.2017.02.001.
(146) Hatam, L. J.; Kayden, H. J. A High-Performance Liquid Chromatographic Method for the Determination of Tocopherol in Plasma and Cellular Elements of the Blood. *J Lipid Res* **1979**, *20* (5), 639–645.
(147) Coquette, A.; Vray, B.; Vanderpas, J. Role of Vitamin E in the Protection of the Resident Macrophage Membrane against Oxidative Damage. *Arch Int Physiol Biochim* **1986**, *94* (5), S29-34.
(148) Lewis, E. D.; Meydani, S. N.; Wu, D. Regulatory Role of Vitamin E in the Immune System and Inflammation. *IUBMB Life* **2019**, *71* (4), 487–494. https://doi.org/10.1002/iub.1976.
(149) Tengerdy, R. P.; Heinzerling, R. H.; Brown, G. L.; Mathias, M. M. Enhancement of the Humoral Immune Response by Vitamin E. *Int Arch Allergy Immunol* **1973**, *44* (2), 221–232. https://doi.org/10.1159/000230931.
(150) Wallert, M.; Schmölz, L.; Galli, F.; Birringer, M.; Lorkowski, S. Regulatory Metabolites of Vitamin E and Their Putative Relevance for Atherogenesis. *Redox Biol* **2014**, *2*, 495–503. https://doi.org/10.1016/j.redox.2014.02.002.
(151) Kopańska, M.; Batoryna, M.; Banaś-Ząbczyk, A.; Błajda, J.; Lis, M. W. The Effect of α-Tocopherol on the Reduction of Inflammatory Processes and the Negative Effect of Acrylamide. *Molecules* **2022**, *27* (3), 965. https://doi.org/10.3390/molecules27030965.
(152) Reiter, E.; Jiang, Q.; Christen, S. Anti-Inflammatory Properties of α- and γ-Tocopherol. *Mol Aspects Med* **2007**, *28* (5–6), 668–691. https://doi.org/10.1016/j.mam.2007.01.003.
(153) Burton, G. W. Vitamin E: Molecular and Biological Function. *Proceedings of the Nutrition Society* **1994**, *53* (2), 251–262. https://doi.org/10.1079/PNS19940030.
(154) Buettner, G. R. The Pecking Order of Free Radicals and Antioxidants: Lipid Peroxidation, α-Tocopherol, and Ascorbate. *Arch Biochem Biophys* **1993**, *300* (2), 535–543. https://doi.org/10.1006/abbi.1993.1074.
(155) Niki, E. Evidence for Beneficial Effects of Vitamin E. *Korean J Intern Med* **2015**, *30* (5), 571–579. https://doi.org/10.3904/kjim.2015.30.5.571.
(156) YAMAUCHI, R. Vitamin E: Mechanism of Its Antioxidant Activity. *Food Science and Technology International, Tokyo* **1997**, *3* (4), 301–309. https://doi.org/10.3136/fsti9596t9798.3.301.
(157) Van Bavel, N.; Lai, P.; Amrein, M.; Prenner, E. J. Pulmonary Surfactant Function and Molecular Architecture Is Disrupted in the Presence of Vaping Additives. *Colloids Surf B Biointerfaces* **2023**, *222*, 113132. https://doi.org/10.1016/j.colsurfb.2023.113132.
(158) Taktikakis, P.; Côté, M.; Subramaniam, N.; Kroeger, K.; Youssef, H.; Badia, A.; DeWolf, C. Understanding the Retention of Vaping Additives in the Lungs: Model Lung Surfactant Membrane Perturbation by Vitamin E and Vitamin E Acetate. *Langmuir* **2024**, *40* (11), 5651–5662. https://doi.org/10.1021/acs.langmuir.3c02952.
(159) Martin, A.; Tempra, C.; Yu, Y.; Liekkinen, J.; Thakker, R.; Lee, H.; de Santos Moreno, B.; Vattulainen, I.; Rossios, C.; Javanainen, M.; Bernardino de la Serna, J. Exposure to Aldehyde Cherry E-Liquid Flavoring and Its Vaping Byproduct Disrupt Pulmonary Surfactant Biophysical Function. *Environ Sci Technol* **2024**, *58* (3), 1495–1508. https://doi.org/10.1021/acs.est.3c07874.

(160) Graham, E.; McCaig, L.; Shui-Kei Lau, G.; Tejura, A.; Cao, A.; Zuo, Y. Y.; Veldhuizen, R. E-Cigarette Aerosol Exposure of Pulmonary Surfactant Impairs Its Surface Tension Reducing Function. *PLoS One* **2022**, *17* (11), e0272475. https://doi.org/10.1371/journal.pone.0272475.
(161) Xu, L.; Yang, Y.; Simien, J. M.; Kang, C.; Li, G.; Xu, X.; Haglund, E.; Sun, R.; Zuo, Y. Y. Menthol in Electronic Cigarettes Causes Biophysical Inhibition of Pulmonary Surfactant. *American Journal of Physiology-Lung Cellular and Molecular Physiology* **2022**, *323* (2), L165–L177. https://doi.org/10.1152/ajplung.00015.2022.
(162) Yammine, A.; Nury, T.; Vejux, A.; Latruffe, N.; Vervandier-Fasseur, D.; Samadi, M.; Greige-Gerges, H.; Auezova, L.; Lizard, G. Prevention of 7-Ketocholesterol-Induced Overproduction of Reactive Oxygen Species, Mitochondrial Dysfunction and Cell Death with Major Nutrients (Polyphenols, Ω3 and Ω9 Unsaturated Fatty Acids) of the Mediterranean Diet on N2a Neuronal Cells. *Molecules* **2020**, *25* (10), 2296. https://doi.org/10.3390/molecules25102296.
(163) Debbabi, M.; Nury, T.; Zarrouk, A.; Mekahli, N.; Bezine, M.; Sghaier, R.; Grégoire, S.; Martine, L.; Durand, P.; Camus, E.; Vejux, A.; Jabrane, A.; Bretillon, L.; Prost, M.; Moreau, T.; Ammou, S.; Hammami, M.; Lizard, G. Protective Effects of α-Tocopherol, γ-Tocopherol and Oleic Acid, Three Compounds of Olive Oils, and No Effect of Trolox, on 7-Ketocholesterol-Induced Mitochondrial and Peroxisomal Dysfunction in Microglial BV-2 Cells. *Int J Mol Sci* **2016**, *17* (12), 1973. https://doi.org/10.3390/ijms17121973.
(164) Grau, A.; Ortiz, A. Dissimilar Protection of Tocopherol Isomers against Membrane Hydrolysis by Phospholipase A2. *Chem Phys Lipids* **1998**, *91* (2), 109–118. https://doi.org/10.1016/S0009-3084(97)00101-1.
(165) Atkinson, J.; Marquardt, D.; Harroun, T. CHAPTER 3. The Behaviour of Vitamin E in Membranes; 2019; pp 32–50. https://doi.org/10.1039/9781788016216-00032.
(166) Soblosky, L.; Ramamoorthy, A.; Chen, Z. Membrane Interaction of Antimicrobial Peptides Using E. Coli Lipid Extract as Model Bacterial Cell Membranes and SFG Spectroscopy. *Chem Phys Lipids* **2015**, *187*, 20–33. https://doi.org/10.1016/j.chemphyslip.2015.02.003.
(167) Zhang, L. Disulfide Bonds Affect the Binding Sites of Human β Defensin Type 3 on Negatively Charged Lipid Membranes. *J Phys Chem B* **2020**, *124* (11), 2088–2100. https://doi.org/10.1021/acs.jpcb.9b10529.
(168) Elías-Wolff, F.; Lindén, M.; Lyubartsev, A. P.; Brandt, E. G. Curvature Sensing by Cardiolipin in Simulated Buckled Membranes. *Soft Matter* **2019**, *15* (4), 792–802. https://doi.org/10.1039/C8SM02133C.
(169) Chowdhury, U. D.; Paul, A.; Bhargava, B. L. The Effect of Lipid Composition on the Dynamics of Tau Fibrils. *Proteins: Structure, Function, and Bioinformatics* **2022**, *90* (12), 2103–2115. https://doi.org/10.1002/prot.26401.
(170) Yakoubi, S.; Kobayashi, I.; Uemura, K.; Saidani-Tounsi, M.; Nakajima, M.; Isoda, H.; A. Neves, M. Nanoscale Delivery System for Improving Bacillus Subtilis Probiotic Viability: A Promising Safety-Enhanced Nanoemulsion. *Food Biosci* **2023**, *56*, 103184. https://doi.org/10.1016/j.fbio.2023.103184.
(171) Gothandapani, D.; Makpol, S. Effects of Vitamin E on the Gut Microbiome in Ageing and Its Relationship with Age-Related Diseases: A Review of the Current Literature. *Int J Mol Sci* **2023**, *24* (19), 14667. https://doi.org/10.3390/ijms241914667.

(172) Duncan, S. L.; Larson, R. G. Comparing Experimental and Simulated Pressure-Area Isotherms for DPPC. *Biophys J* **2008**, *94* (8), 2965–2986. https://doi.org/10.1529/biophysj.107.114215.
(173) Massey, J. B.; She, H. S.; Pownall, H. J. Interaction of Vitamin E with Saturated Phospholipid Bilayers. *Biochem Biophys Res Commun* **1982**, *106* (3), 842–847. https://doi.org/10.1016/0006-291X(82)91787-9.
(174) Selladurai, S. L.; Miclette Lamarche, R.; Schmidt, R.; DeWolf, C. E. Model Lung Surfactant Films: Why Composition Matters. *Langmuir* **2016**, *32* (41), 10767–10775. https://doi.org/10.1021/acs.langmuir.6b02945.
(175) Lipp, M. M.; Lee, K. Y. C.; Zasadzinski, J. A.; Waring, A. J. Design and Performance of an Integrated Fluorescence, Polarized Fluorescence, and Brewster Angle Microscope/Langmuir Trough Assembly for the Study of Lung Surfactant Monolayers. *Review of Scientific Instruments* **1997**, *68* (6), 2574–2582. https://doi.org/10.1063/1.1148163.
(176) Adeyeye, E.; Oyarekua, M. Lipid Profile of the Skin and Muscle of Freshwater Sardine (<I>Pellenula Afzeliusi</I>): Nutritional /Dietary Implications. *Bangladesh Journal of Scientific and Industrial Research* **1970**, *46* (4), 523–532. https://doi.org/10.3329/bjsir.v46i4.9602.
(177) Vicetti, R.; Ishitani, T.; Salas, A.; Ayala, M. Use of Alpha-Tocopherol Combined with Synergists and Compared to Other Antioxidants on the Oxidative Stability of Sardine Skin Lipids. *Journal of Food Composition and Analysis* **2005**, *18* (2–3), 131–137. https://doi.org/10.1016/j.jfca.2003.12.010.
(178) Suárez-Jiménez, G.; López-Saiz, C.; Ramírez-Guerra, H.; Ezquerra-Brauer, J.; Ruiz-Cruz, S.; Torres-Arreola, W. Role of Endogenous and Exogenous Tocopherols in the Lipid Stability of Marine Oil Systems: A Review. *Int J Mol Sci* **2016**, *17* (12), 1968. https://doi.org/10.3390/ijms17121968.
(179) Oliva-Teles, A. Nutrition and Health of Aquaculture Fish. *J Fish Dis* **2012**, *35* (2), 83–108. https://doi.org/10.1111/j.1365-2761.2011.01333.x.
(180) US Food and Drug Administration. Lung Illnesses Associated with Use of Vaping Products. **2020**.
(181) Weis, R. M.; McConnell, H. M. Two-Dimensional Chiral Crystals of Phospholipid. *Nature* **1984**, *310* (5972), 47–49. https://doi.org/10.1038/310047a0.
(182) Alvares, D. S.; Fanani, M. L.; Ruggiero Neto, J.; Wilke, N. The Interfacial Properties of the Peptide Polybia-MP1 and Its Interaction with DPPC Are Modulated by Lateral Electrostatic Attractions. *Biochimica et Biophysica Acta (BBA) - Biomembranes* **2016**, *1858* (2), 393–402. https://doi.org/10.1016/j.bbamem.2015.12.010.
(183) Trabelsi, S.; Zhang, S.; Lee, T. R.; Schwartz, D. K. Linactants: Surfactant Analogues in Two Dimensions. *Phys Rev Lett* **2008**, *100* (3), 037802. https://doi.org/10.1103/PhysRevLett.100.037802.
(184) Quinn, P. J. Characterisation of Clusters of A-Tocopherol in Gel and Fluid Phases of Dipalmitoylglycerophosphocholine. *Eur J Biochem* **1995**, *233* (3), 916–925. https://doi.org/10.1111/j.1432-1033.1995.916_3.x.
(185) Salmon, T. B. Biological Consequences of Oxidative Stress-Induced DNA Damage in Saccharomyces Cerevisiae. *Nucleic Acids Res* **2004**, *32* (12), 3712–3723. https://doi.org/10.1093/nar/gkh696.

(186) Canchola, A.; Ahmed, C. M. S.; Chen, K.; Chen, J. Y.; Lin, Y.-H. Formation of Redox-Active Duroquinone from Vaping of Vitamin E Acetate Contributes to Oxidative Lung Injury. *Chem Res Toxicol* **2022**, *35* (2), 254–264. https://doi.org/10.1021/acs.chemrestox.1c00309.
(187) CCI Research Inc. *Summary of Results for the Canadian Student Tobacco, Alcohol and Drugs Survey 2021-22*; 2022.
(188) Sharma, G.; Goodwin, J. Effect of Aging on Respiratory System Physiology and Immunology. *Clin Interv Aging* **2006**, *1* (3), 253–260. https://doi.org/10.2147/ciia.2006.1.3.253.
(189) American Lung Association. Popcorn Lung: A Dangerous Risk of Flavored E-Cigarettes. 2016.
(190) Louisa Dalton, special to C. Vape Flavor Gums up Lung Coating in Lab Model. *C&EN Global Enterprise* **2024**, *102* (4), 6–6. https://doi.org/10.1021/cen-10204-scicon4.

Appendices

Appendix A

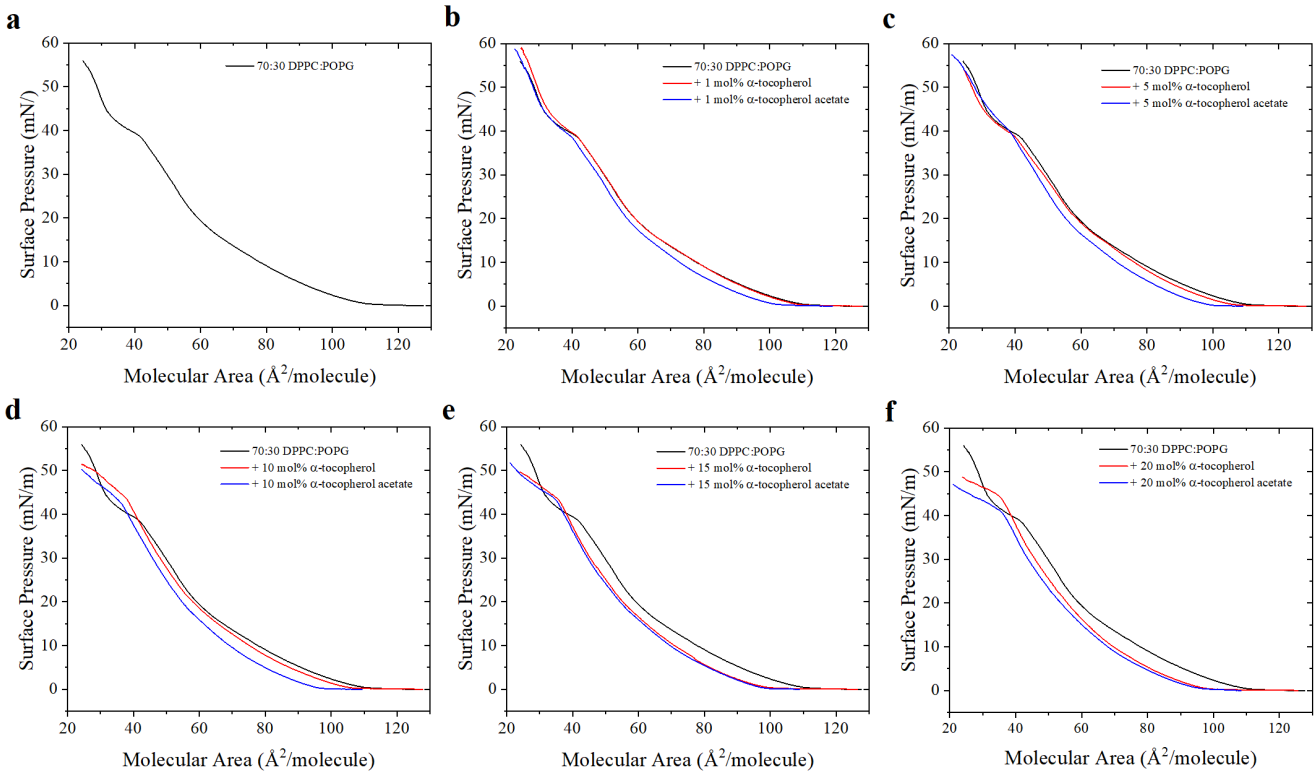

Figure A1. Surface pressure-area isotherms of (a) DPPC:POPG (7:3) in the (a) absence of additive and in the presence of (b) 1 mol %, (c) 5 mol %, (d) 10 mol %, (e) 15 mol % and (f) 20 mol % of α−tocopherol and α−tocopherol acetate.

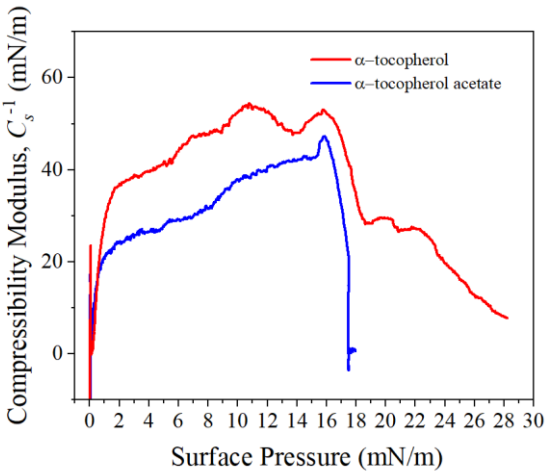

Figure A2. Compressibility moduli of α–tocopherol (red) and α–tocopherol acetate (blue) films as a function of surface pressure.

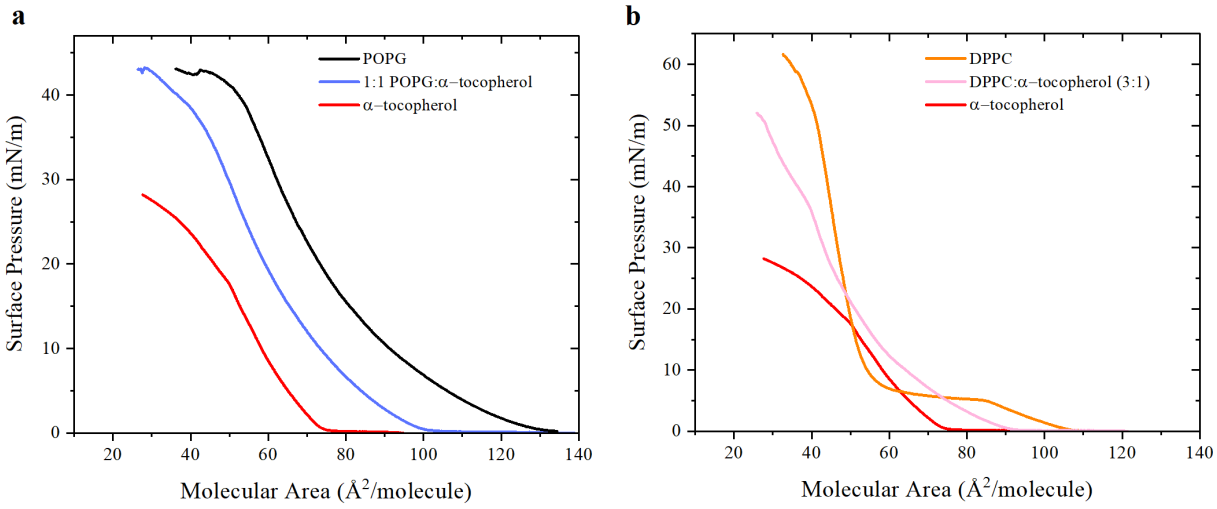

Figure A3. Surface pressure-area isotherms for (a) POPG:α–tocopherol (1:1), and (b) DPPC:α–tocopherol (3:1).

Table A1. Excess areas for POPG:α–tocopherol (1:1) and DPPC:α–tocopherol (3:1) at 1 mN/m, 5 mN/m, 10 mN/m and 15 mN/m.

System	Pressure (mN/m)	Excess Area (Å^2/molecule)
POPG:α–tocopherol (1:1)	1	-1
	5	-2
	10	-2
	15	-2
DPPC:α–tocopherol (3:1)	1	-7
	5	-4
	10	+8
	15	+4

Table A2. GIXD fitted peak positions and FWHM for Bragg peaks and Bragg rods for DPPC:POPG (7:3) with and without added α–tocopherol and α–tocopherol acetate on TBS subphase at 22.0 ± 0.5 °C. For 15 mol % and 20 mol % α–tocopherol at 45 mN/m, and 20 mol % α-tocopherol acetate at 35 mN/m and 45 mN/m, the weak peaks positioned near the horizon make fitting difficult; tentative peak positions for 35 mN/m are given.

		d (10) [Å]				d (01) [Å]				d ($1\bar{1}$) [Å]			
System	Pressure [mN/m]	Q_{xy}	fwhm [Å^{-1}]	Q_z	fwhm [Å^{-1}]	Q_{xy}	fwhm [Å^{-1}]	Q_z	fwhm [Å^{-1}]	Q_{xy}	fwhm [Å^{-1}]	Q_z	fwhm [Å^{-1}]
DPPC:POPG (7:3)	18	1.33	0.067	0.72	0.29	1.39	0.071	0.64	0.29	1.47	0.017	0.07	0.29
	35	1.35	0.036	0.66	0.28	1.37	0.085	0.52	0.28	1.47	0.018	0.13	0.28
	45	1.44	0.046	0.50	0.30	1.46	0.027	0.39	0.30	1.48	0.025	0.09	0.36
DPPC:POPG (7:3) + 10 mol % α–tocopherol	35	1.38	0.036	0.54	0.28	1.42	0.080	0.42	0.28	1.48	0.017	0.09	0.28
	45	1.44	0.051	0.27	0.30	1.47	0.10	0.20	0.30	1.48	0.024	0.06	0.30
DPPC:POPG (7:3) + 15 mol % α–tocopherol	35	1.38	0.071	0.47	0.27	1.45	0.057	0.40	0.27	1.48	0.023	0.06	0.27
	45	1.44	0.019	0.24	0.28	1.46	0.015	0.18	0.28	1.48	0.077	0.11	0.28
DPPC:POPG (7:3) + 20 mol % α–tocopherol	35	1.44	0.095	0.45	0.27	1.45	0.024	0.34	0.27	1.48	0.014	0.11	0.27
	45	1.46	0.005	0.17	0.28	1.47	0.055	0.12	0.28	1.48	0.14	0.05	0.28
DPPC:POPG (7:3) + 20 mol % α–tocopherol acetate	20	1.39	0.007	0.56	0.30	1.42	0.087	0.52	0.30	1.48	0.019	0.04	0.30
	35	1.45	0.11	0.29	0.27	1.46	0.023	0.22	0.27	1.49	0.042	0.06	0.27

Table A3. Unit cell parameters derived from the fits of the GIXD data for DPPC:POPG (7:3) with and without added α–tocopherol and α–tocopherol acetate on TBS subphase, at 22.0 ± 0.5 °C. For 15 mol % and 20 mol % α–tocopherol at 45 mN/m, and 20 mol % α-tocopherol acetate at 35 mN/m and 45 mN/m, the weak peaks positioned near the horizon make fitting difficult; a tentative unit cell for 35 mN/m is given. d represents the d-spacing in a given lattice direction, the chain tilt is given relative to the normal to the plane of the monolayer, A_{xy} is the chain cross-sectional area in the plane of the monolayer and L_c is the vertical correlation length.

System	Surface Pressure [mN/m]	d (10) [Å]	d (01) [Å]	d ($1\bar{1}$) [Å]	Chain tilt [°]	A_{xy} [Å^2]	L_c in the Q_z direction [Å^2]
DPPC:POPG (7:3)	18	4.94	5.17	5.46	31	23.2	19.4
	35	5.02	5.12	5.46	28	23.3	20.1
	45	4.88	4.96	5.03	20	21.3	18.9
DPPC:POPG (7:3) + 10 mol % α–tocopherol	35	4.92	5.07	5.28	23	22.4	20.1
	45	4.85	4.96	5.00	11	21.1	18.8
DPPC:POPG (7:3) + 15 mol % α–tocopherol	35	4.89	5.07	5.22	20	22.1	20.5
	45	4.89	4.97	5.03	10	21.3	20.1
DPPC:POPG (7:3) + 20 mol % α–tocopherol	35	4.91	4.96	5.03	19	21.3	20.9
	45	4.87	4.92	4.95	7	20.9	20.1
DPPC:POPG (7:3) + 20 mol % α–tocopherol acetate	20	4.93	5.03	5.24	25	22.2	18.9
	35	4.87	4.90	5.03	12	21.1	20.9

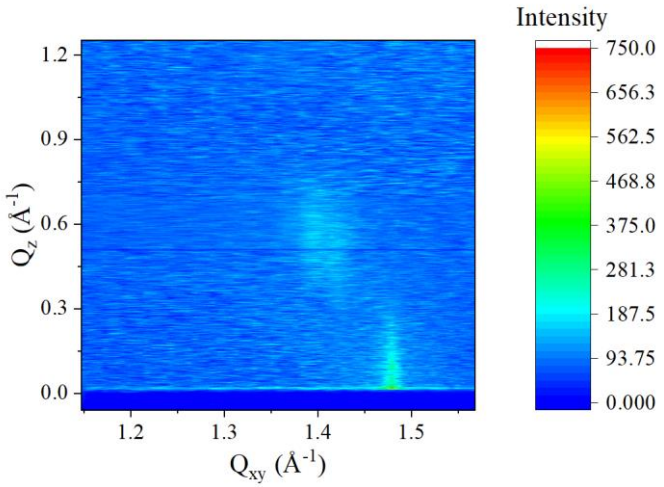

Figure A4. Contour plots of the X–ray intensity as a function of the in-plane (Q_{xy}) and out-of-plane (Q_z) scattering vector components for DPPC:POPG (7:3) of 20 mol % α–tocopherol with no additional peaks at higher Q_{xy} at a surface pressure of 35 mN/m.

Table A4. Fitted parameters for XR data for DPPC:POPG (7:3) with varying molar proportions of α–tocopherol added (15 mol % and 20 mol %) on TBS subphase, at 22.0 ± 0.5 °C, and at 35 mN/m.

	Tail		Headgroup	
System	Thickness (Å)	ρ (e^-Å^{-3})	Thickness (Å)	ρ (e^-Å^{-3})
DPPC:POPG (7:3)	17.6	0.336	6.89	0.251
DPPC:POPG (7:3) + 15 mol % α–tocopherol	15.2	0.397	7.80	0.219
DPPC:POPG (7:3) + 20 mol % α–tocopherol	15.1	0.398	7.81	0.218

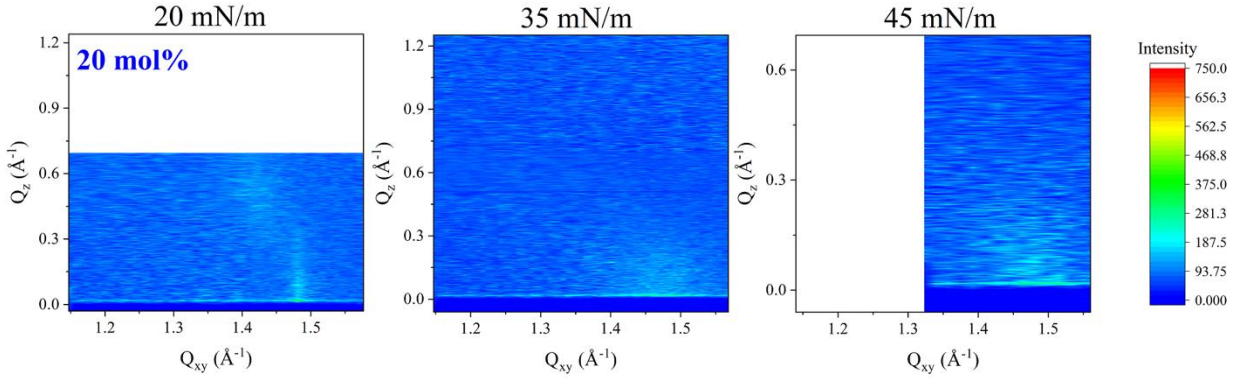

Figure A5. Contour plots of the X–ray intensity as a function of the in-plane (Q_{xy}) and out-of-plane (Q_z) scattering vector components for DPPC:POPG (7:3) with 20 mol % α–tocopherol acetate at surface pressures (left to right); 20 mN/m, 35 mN/m and 45 mN/m.

Appendix B

Table B1. Numerical values for key transitions in surface pressure-area isotherms for DPPC, POPG, DPPC:α–tocopherol (3:1, 1:1, 1:3) and POPG:α–tocopherol (3:1, 1:1, 1:3).

System	Onset Area (Å^2/molecule)	Collapse Area$_1$ (Å^2/molecule)	Collapse π_1 (mN/m)	Collapse Area$_2$ (Å^2/molecule)	Collapse π_2 (mN/m)
DPPC	106	40	55	-	-
A–tocopherol	75	50	17	-	-
DPPC:α–tocopherol (3:1)	90	42	38	30	51
DPPC:α–tocopherol (1:1)	83	45	32	-	-
DPPC:α–tocopherol (1:3)	81	53	23	-	-
POPG	130	51	42	-	-
POPG:α–tocopherol (3:1)	122	48	42	-	-
POPG:α–tocopherol (1:1)	105	41	38	-	-
POPG:α–tocopherol (1:3)	80	41	28	-	-

Table B2. Excess areas with corresponding error for binary mixtures of DPPC with α–tocopherol and POPG with α–tocopherol for molar ratios of DPPC or POPG:α–tocopherol (3:1, 1:1, 1:3). Note all excess areas are within error of ± 1 Å^2/molecule.

System	Surface Pressure (mN/m)	Excess Area (Å^2/molecule)
DPPC:α–tocopherol (3:1)	1	-7
	5	-3
	10	8
	15	4
DPPC:α–tocopherol (1:1)	1	-7
	5	-5
	10	3
	15	1
DPPC:α–tocopherol (1:3)	1	-2
	5	0
	10	5
	15	4
POPG:α–tocopherol (3:1)	1	7
	5	5
	10	5
	15	5
POPG:α–tocopherol (1:1)	1	-1
	5	-2
	10	-2
	15	-2
POPG:α–tocopherol (1:3)	1	-6
	5	-5
	10	-4
	15	-4

Table B3. Estimated excess areas using isotherms from Jurak *et al.* for binary mixtures of POPC with α–tocopherol and DOPC with α–tocopherol for molar ratios of POPC or DOPC:α–tocopherol (3:1, 1:1, 1:3) at 5 mN/m.

System	Excess Area (Å^2/molecule)
POPC:α–tocopherol (3:1)	4.3
POPC:α–tocopherol (1:1)	-0.5
POPC:α–tocopherol (1:3)	-2.3
DOPC:α–tocopherol (3:1)	-2.5
DOPC:α–tocopherol (1:1)	-1.0
DOPC:α–tocopherol (1:3)	-2.5

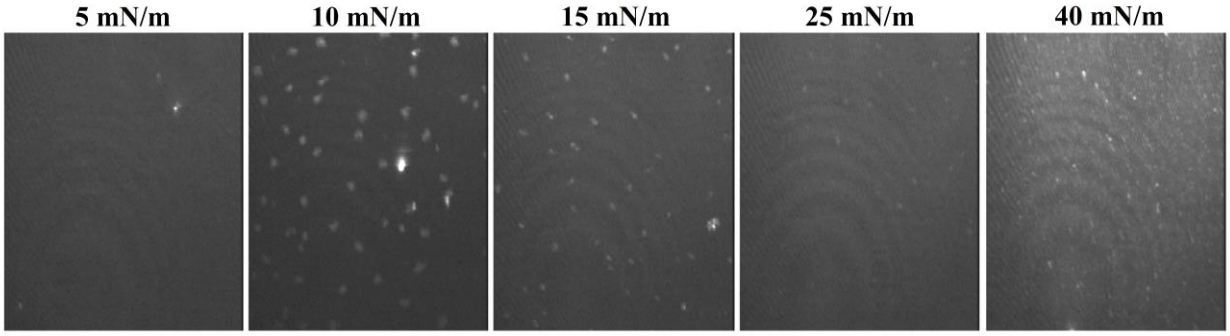

Figure B1. BAM images (220 μm × 275 μm) of DPPC:α–tocopherol (3:1) that have been adjusted in brightness in contrast.

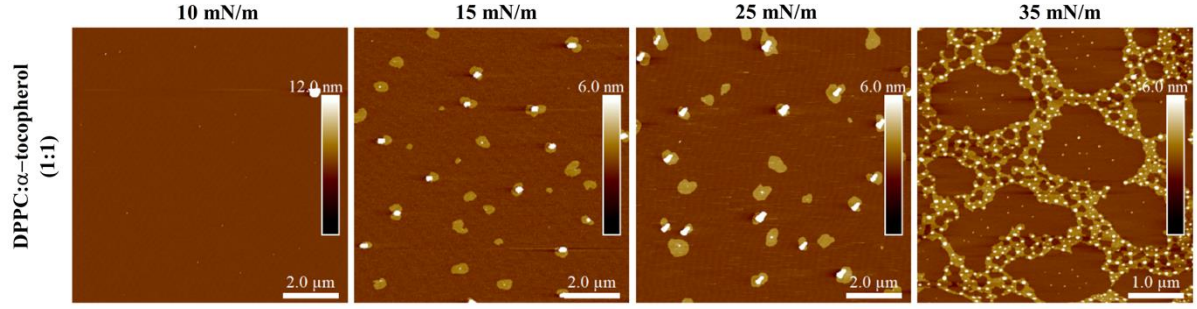

Figure B2. AFM images of monolayer films transferred onto mica with visible condensed phase domains and nanodomains at 10 mN/m (10 μm × 10 μm), 15 mN/m (10 μm × 10 μm), 25 mN/m (10 μm × 10 μm), and 35 mN/m (5 μm × 5 μm) for DPPC:α–tocopherol (1:1).

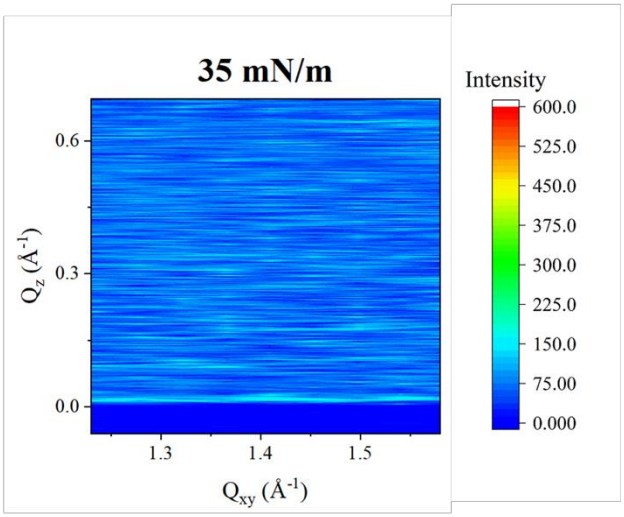

Figure B3. Contour plots of the X–ray intensities versus in-plane scattering vector components Q_{xy} and Q_z for POPG:α–tocopherol (1:1) at 35 mN/m.